Half-Heusler Alloys as Promising Thermoelectric Materials

by

Alexander A. Page

A dissertation submitted in partial fulfillment
of the requirements for the degree of
Doctor of Philosophy
(Physics)
in the University of Michigan
2017

Doctoral Committee:

Professor Ctirad Uher, Chair
Assistant Professor Emmanouil Kioupakis
Associate Professor Lu Li
Associate Professor Pierre Ferdinand P. Poudeu
Professor Anton Van der Ven, University of California Santa Barbara

Alexander A. Page

aapage@umich.edu

ORCID iD: 0000-0002-8783-3659

Dedication

To my mother, father, and brother.

Table of Contents

List of Figures

List of Tables

Abstract

This thesis describes Ph.D. research on the half-Heusler class of thermoelectric materials. Half-Heusler alloys are a versatile class of materials that have been studied for use in photovoltaics, phase change memory, and thermoelectric power generation. With respect to thermoelectric power generation, new approaches were recently developed in order to improve the thermoelectric figure of merit, *ZT*, of half-Heusler alloys. Two of the strategies discussed in this work are adding excess Ni within *M*NiSn (*M* = Ti, Zr, or Hf) compounds to form full-Heusler nanostructures and using isoelectronic substitution of Ti, Zr, and Hf in *M*NiSn compounds to create microscale grain boundaries. This work uses computational simulations based on density functional theory, combined with the cluster expansion method, to predict the stable phases of pseudo-binary and pseudo-ternary composition systems. Statistical mechanics methods were used to calculate temperature-composition phase diagrams that relate the equilibrium phases. It is shown that full-Heusler nanostructures are predicted to remain stable even at high temperatures, and the microscale grain boundaries observed in (Ti,Zr,Hf)NiSn materials are found to be thermodynamically unstable at equilibrium. A new strategy of combining *M*NiSn materials with ZrNiPb has also recently emerged, and theoretical and experimental work show that a solid solution of the two materials is stable.

Chapter 1 Introduction to Thermoelectrics

1.1 Waste heat

Over the past fifty years, there has been a global push for renewable energy due to environmental concerns. However, despite recent advances in technology, renewable energy is still only a small fraction of the total energy market. According to a study by Lawrence Livermore National Laboratory, in the year 2016 sustainable renewables only made up about 5.4 % of the total energy production in the United States, as shown in Figure 1. It may be many years until renewable energy is in a position to fully replace fossil fuels, therefore intermediate technologies are necessary to reduce carbon output and increase the efficiency of the existing fossil fuel

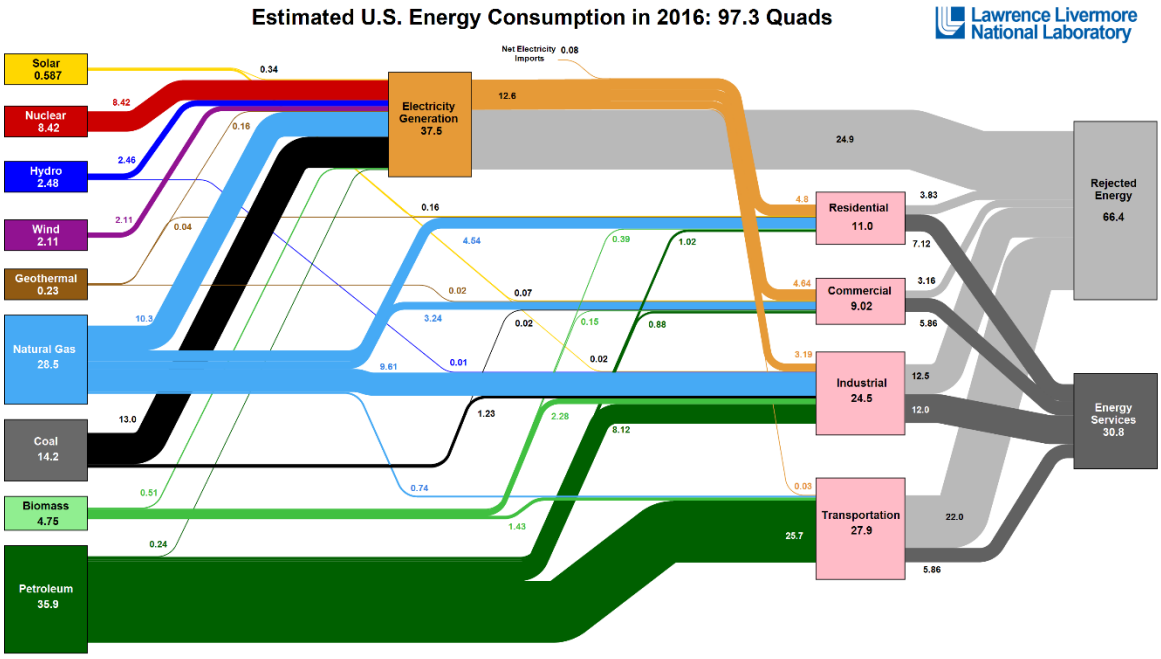

Figure 1. Energy flow diagram of US energy production and consumption. Source: Lawrence Livermore National Laboratory, March 2017. Data is based on DOE/EIA MER (2016)

technology during this transition period. Thermoelectric power generation is an appealing technology to help increase overall efficiency during and after the transition to renewable energy. Thermoelectric power generation is a solid state conversion of heat energy directly into electricity. Thermoelectric devices are capable of converting waste heat into usable electricity with no moving parts, and are extremely compact and reliable in operation. Using waste heat as a power source has considerable promise as 66% of all generated energy is lost as waste heat, shown in light grey in Figure 1. Even capturing and converting a small fraction of the waste heat would have a tremendous impact on the environment.

1.2 The thermoelectric effects

The principle of thermoelectricity is to use the charge carriers within a solid material as the working medium for a power generator, or in the reverse process as a cooler. The thermoelectric effect was discovered in 1821 by the German physicist Thomas Johann Seebeck. Seebeck discovered that if two wires of different metals were joined together to make a loop, and the wires were heated at their junction, a voltage would develop between the two open ends. Likewise, if the two ends were connected, a current would flow around the loop. The voltage produced, ΔV, was found to be linearly related to the difference in temperature of both sides, ΔT. The constant of proportionality is now called the Seebeck coefficient, S, given as

$$\Delta V = S\Delta T \tag{1}$$

Later, in 1834, a French watchmaker and physicist, Jean Peltier, discovered that when current was passed through the junction between two different metals, heat was absorbed at one of the junctions and heat was liberated at the other. The amount of heat released or absorbed was

found to be linearly related to the current passed through, and the coefficient of proportionality is now called the Peltier coefficient, π, defined as

$$\mathrm{Q} = \pi I \tag{2}$$

where Q is the heat absorbed or released at the interface and I is the current.

The Seebeck effect relates an applied temperature difference to a generated voltage difference, and the Peltier effect relates an applied current to the heat absorbed or released. In 1851, William Thomson (who later became Lord Kelvin) showed that the two effects are related, and introduced a third effect known as the Thomson effect, which relates the heat production rate of a material to the current passed through it and the temperature gradient. The performance of thermoelectric materials was first characterized by Edmund Altenkirch in 1909, and later modernized and formalized by Abram Ioffe. Ioffe expressed the maximum efficiency of a thermoelectric power generator as a product of the Carnot efficiency and a term that depends on the thermoelectric figure of merit, ZT,

$$\eta_{max} = \frac{T_H - T_C}{T_H}\left(\frac{\sqrt{1+ZT}-1}{\sqrt{1+ZT}+\frac{T_C}{T_H}}\right) \tag{3}$$

where T_H is the temperature of the hot junction, T_C is the temperature of the cold junction. The first term, $\frac{T_H - T_C}{T_H}$, is the Carnot efficiency. As ZT goes to infinity, the efficiency of the device approaches the Carnot limit, as shown in Figure 2.

The thermoelectric figure of merit, ZT, is a material dependent parameter given by

$$ZT = \frac{S^2 \sigma T}{K} \tag{4}$$

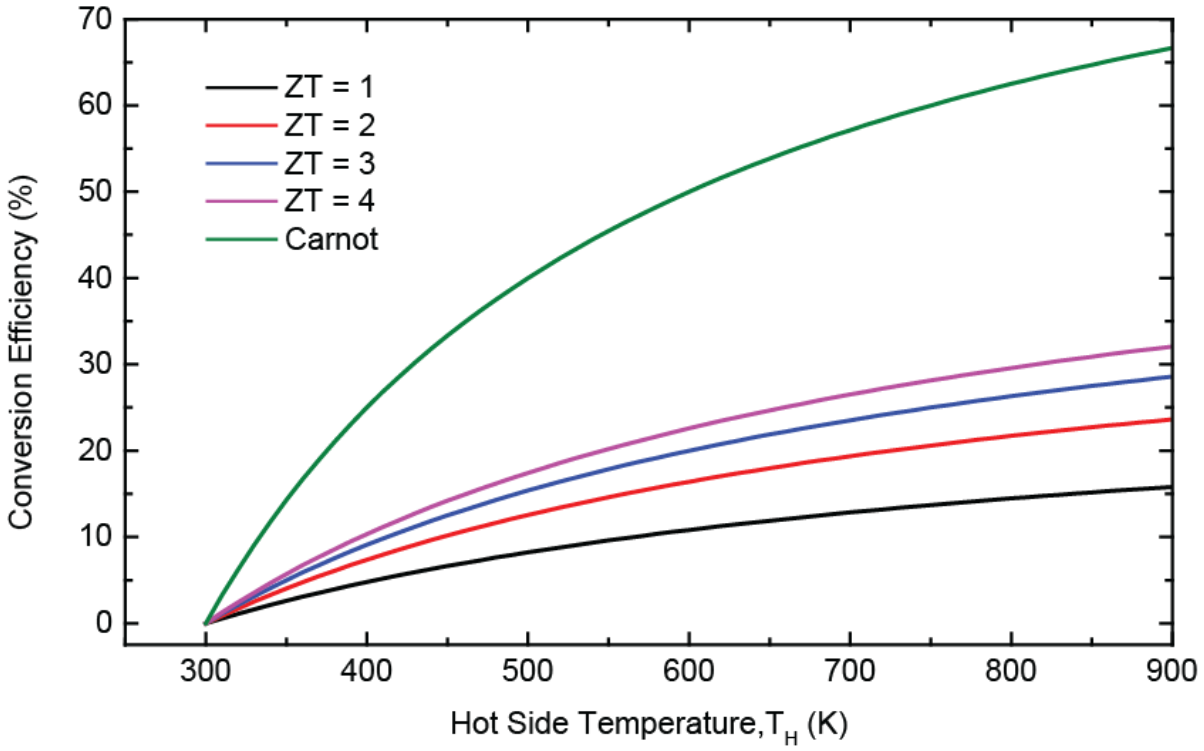

Figure 2. Plot of conversion efficiency vs. hot side temperature. The cold side temperature is taken to be 300 K and efficiencies for ZT = 1, 2, 3, and 4 are shown compared to the Carnot limit.

where S is the Seebeck coefficient, σ is the electrical conductivity, T is the absolute temperature, and K is the thermal conductivity. In order to maximize the ZT of a material, one would need to maximize the numerator, known as the power factor, where $PF = S^2\sigma$, while simultaneously minimizing the thermal conductivity. In practice this is a very difficult task, as the materials properties are not independent of each other. The Seebeck coefficient decreases with increasing carrier density, whereas the electrical conductivity increases with increasing carrier density. Also the electrical contribution to the thermal conductivity increases with carrier density. In this respect, strategies must be developed that bypass these standard semiconductor relations.

Modern strategies to improve thermoelectrics are largely influenced by two theoretical papers published in 1993 by Hicks and Dresselhaus [*1*, *2*]. Before these works, known

thermoelectric materials, such as Bi_2Te_3, had a maximum *ZT* of about 1. The Hicks and Dresselhaus papers suggested that large improvements could be achieved by utilizing the quantum nature of lower dimensional structures, which can advantageously alter the density of states in ways that enable simultaneous increases of the Seebeck coefficient and the electrical conductivity. In addition to enhancing the electrical properties, strategies emerged to use nanoscale grain boundaries to enhance phonon scattering while keeping the electrical properties unharmed. This concept is stated best as the 'phonon glass/electron crystal' concept, proposed by Slack [*3*]. These new strategies breathed life back into the field of thermoelectrics, which was considered stagnant for many years. Since 1993, dozens of new potential thermoelectric materials have been discovered and *ZT* values have improved from 1 to *ZT* as high as 2.6, specifically in single crystal SnSe [*4*]. Of the new materials focused on in the last 20 years, half-Heusler alloys have gathered considerable attention as potential low cost high durability thermoelectric materials. The remainder of this work is focused on the class of half-Heusler alloys and their thermoelectric properties.

Chapter 2 Half Heusler Alloys as Thermoelectric Materials

2.1 The half-Heusler and full-Heusler crystal structure

Half-Heusler (HH) alloys have recently shown great promise as thermoelectric materials. HH alloys are made of inexpensive, light weight, and environmentally friendly elements. They are stable at high temperatures and have intrinsically high power factors, PF, where $\mathrm{PF} = \alpha^2\sigma$. However, the *ZT* of HH alloys is limited by their large thermal conductivity [*5-8*], which is around 10 W/m-K at room temperature. Many of the recent research efforts on HH alloys have indeed focused on developing techniques to lower the thermal conductivity while preserving the outstanding electronic properties.

Half-Heusler alloys are named after Friedrich Heusler, a German mining engineer and chemist who studied $MnCu_2Sn$ in 1903. Materials with $MnCu_2Sn$ type structures are now named Heusler alloys, which are also referred to as full-Heusler (FH) alloys in order to emphasize the distinction between them and half-Heusler alloys. FH alloys are generally ferromagnetic metals, and have recently become of interest as half-metallic materials, with applications for spin injection in spintronic devices [*9*]. Half-Heusler alloys, on the other hand, are usually non-magnetic and can be semiconductors depending on the valence count of the elements chosen [*10*]. The half-Heusler crystal structure is closely related to the FH structure, except it has a 1:1:1 ratio of elements rather than 1:2:1. HH alloys have a general composition of *XYZ*, where *X* and *Y* are transition

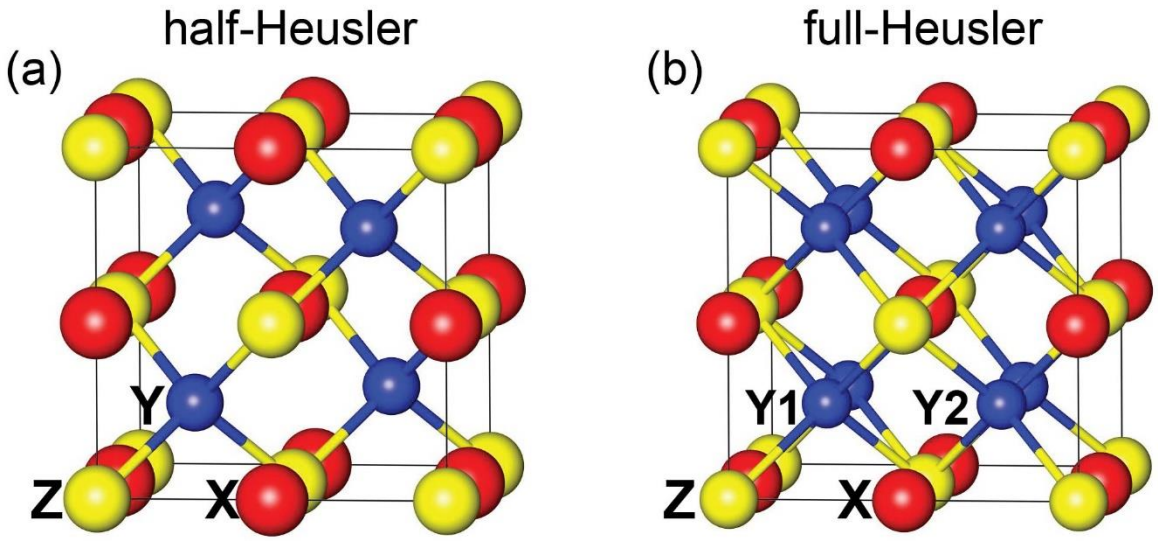

Figure 3. (a) The crystal structure of half-Heusler and (b) full-Heusler alloys. Half-Heusler alloys have composition XYZ, whereas in the full-Heusler structure, the vacancies are filled in with a second atom (Y2-site), making the composition XY_2Z.

metals, and *Z* is a main group element. HH alloys take the form of the MgAgAs structure type, space group F-43*m* (SG #216), and the structure is made up of 4 distinct face-centered cubic (fcc) sublattices [*11*], as shown in Figure 3(a). The *Z* atom is located at (0,0,0), the *Y* atom at (¼, ¼, ¼), and the *X* atom at (½, ½, ½). The fourth fcc sublattice located at (¾, ¾, ¾) remains vacant. The FH structure can be made by simply filling the vacant sublattice with *Y* atoms, making a composition of XY_2Z, as shown in Figure 3(b), where the two sublattices, Y1 and Y2, are symmetrically equivalent.

A large amount of thermoelectrics research has focused on half-Heusler alloys with a composition of *M*NiSn which is usually n-type and *M*CoSb which is usually p-type, where *M* = (Ti, Zr, Hf). Early works showed that *M*NiSn compounds form in the HH structure [*11*], and that they are indeed small gap semiconductors [*7*]. The thermoelectric properties of the materials can be greatly enhanced by use of dopants such as Sb for *M*NiSn [*5*] and Sn for *M*CoSb [*12*].

Furthermore, the high thermal conductivity can be greatly reduced by using isoelectronic substitution on the M-site with Ti, Zr, and Hf. Mass-defect scattering effectively reduces thermal conductivity (~ 4-5 $Wm^{-1}K^{-1}$ at room temperature), while still preserving good electronic properties [*5*, *13*].

2.2 First principles studies of half-Heusler alloys

First principles calculations have served an integral role in understanding the basic physical properties of thermoelectric half-Heusler alloys from an early stage. In 1994, Öğüt and Rabe [*14*] explored the stability of *M*NiSn (M = Ti, Zr, Hf) alloys by *ab initio* calculations. DFT methods were used to calculate the band structures. *M*NiSn compounds were shown to be semiconductors, in agreement with experimental work [*7*]. The theoretical bandgap of about 0.5 eV was found to be indirect between the *Γ*- and *X*-points in the fcc Brillouin zone. Figure 4 shows the band structures of ZrNiSn and $ZrNi_2Sn$, where ZrNiSn has a band gap of 0.48 eV and the full-Heusler $ZrNi_2Sn$ is metallic without a bandgap.

Later, it was demonstrated that the electronic structure of HH alloys depends heavily on the valence electron count [*15*-*17*]. Kandpal *et al.* [*10*] explored this concept in terms of bonding. Using linear muffin tin orbitals (LMTO) in band structure calculations, they visualized the charge density of a unit cell in order to understand the degree of bonding between atoms. The calculations showed that in almost all 8- and 18-valence HH alloys, the structure can be thought of as a covalently bonded Zinc-blend structure between the Y and Z atoms. The X^{n+} ion then fills the $(YZ)^{n-}$ Zinc-blend sublattice, see Figure 3(a), where covalent bonds are indicated between the Y and Z atoms. In addition, calculations were performed on the *p*-type TiCoSb compound, and the charge density shows evidence of covalent bonding in the form of charge density surfaces located

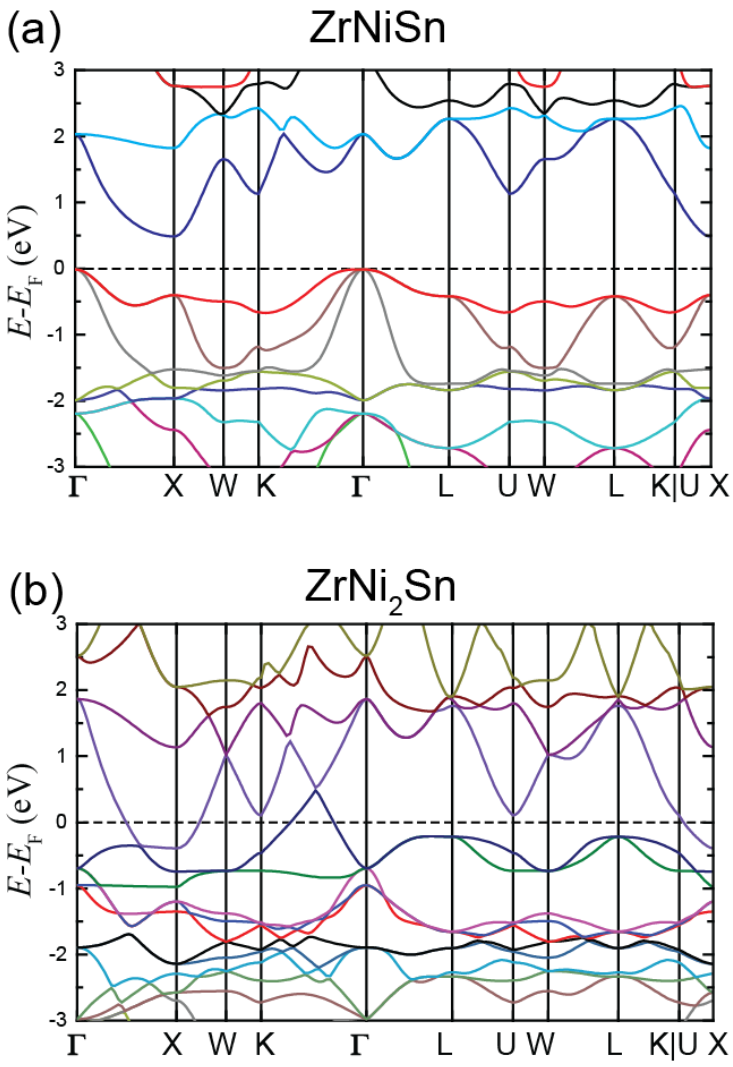

Figure 4. Calculated band structure of ZrNiSn (a) and $ZrNi_2Sn$. Band energy is relative to the valence band maximum (b). Unpublished, Page *et al.*

at the midpoint of the Co-Sb tetrahedral bonds. By simply studying the band structure, and subsequently the localized charge density, Kandpal *et al.* developed a rule that HH alloys with total valence electron counts of 8 and 18 form semiconductors, whereas compounds with valence counts other than 8 or 18 result in half-metallic ferromagnets [*10*].

Recently, in addition to *M*NiSn and *M*CoSb compunds, other HH alloys, such as (V,Nb)FeSb, and even a full-Heusler alloy, VFe_2Al, have come into view as potential candidates

for thermoelectric devices [*18-26*]. Studies of the band structure of *M*FeSb, where *M* = (V,Nb), have led to insights into how to improve their thermoelectric efficiency. *M*FeSb compounds are HH alloys with 18 valence electrons. It was shown that while these materials have high power factors, they also have a high thermal conductivity, on the order of ~10 $Wm^{-1}K^{-1}$ at room temperature. The resultant maximum *ZT* of less than 0.3 does not make *M*FeSb as attractive as other n-type HH alloys for high-temperature power generation[*18-20*]. However, calculated band structures revealed that the *M*FeSb compounds could be more effective as p-type materials because the valence band maxima are located at the L-point, rather than at the Γ-point [*19-21*]. The L-point of the fcc Brillouin zone is 4-fold degenerate. A high valence band degeneracy, $N_v = 4$, is beneficial for thermoelectric performance as the density of states effective mass, m^*, depends on the band effective mass, m_b^* , following $m^* = N_v^{2/3} m_b^*$. A large m^* is desired for good thermoelectric materials; however, having a large m_b^* can decrease the mobility of the charge carriers, hurting the electrical conductivity. Increasing N_v is thus an effective way to improve a material's TE properties without detrimental side effects [*22*]. In accordance with this concept, compounds of $(V_{1-x}Nb_x)_{1-y}Ti_yFeSb$, were synthesized, where Ti acts as a *p*-type dopant. The isoelectronic substitution of Nb for V was done in an effort to reduce the thermal conductivity. This resulted in *p*-type materials with vastly improved *ZT* of 0.8 at 900 K [*23*].

Following this, Fu *et al.* [*21*] further improved the thermoelectric performance by noticing subtle differences in the calculated band structures of VFeSb and NbFeSb. The key differences between the two compounds are the size of the bandgap, i.e., 0.54 eV for NbFeSb and 0.34 eV for VFeSb, and the band effective mass, i.e., $0.16m_e$ for NbFeSb and $0.25m_e$ for VFeSb. Based on these facts, Fu *et al.* predicted that $Nb_{1-x}Ti_xFeSb$ would actually perform better than $(V_{1-x}Nb_x)_{1-y}Ti_yFeSb$. The improvement in *ZT* came primarily from three sources. First, the band effective

mass is reduced in the NbFeSb system, compared to that of VFeSb, leading to large improvements in the carrier mobility. Second, the decrease in band effective mass decreased the carrier concentration at which the PF is maximized. The carrier concentration achievable is limited by the solubility limit of Ti in *M*FeSb, which is about 20%. Therefore, the PF could be maximized within the solubility limit of Ti by decreasing the optimal carrier concentration. Third, the NbFeSb system has a larger bandgap, which increases the temperature at which bipolar contributions begin to diminish thermoelectric performance. All three effects combined led to a large enhancement in performance, with *ZT* of 1.1 at 1100 K. Soon after, it was discovered that Hf was also an effective dopant and has the added benefit of reducing the lattice thermal conductivity *via* increased point defect scattering, compared to that of Ti. The compound $Nb_{0.88}Hf_{0.12}FeSn$ was found to have a record high *ZT* of 1.5 at 1200K [*27*] for p-type half-Heusler alloys. These works on *M*FeSb are a good example of how band structure predictions quickly reveal important insights, which are key in developing new strategies for improving the TE performance of HH alloys.

2.3 Synthesis of half-Heusler alloys

Half-Heusler alloys are remarkably stable and strong materials, however the synthesis process required to obtain homogenous single phase half-Heusler alloys is difficult and still a very active area of research. The synthesis of half-Heusler alloys is challenging because of the very different melting points of the constituent elements involved and the high propensity for defects in the crystal structure. The melting point of Sn is 232 ˚C, whereas the melting point of Zr is 1,855 ˚C, and the melting point of the half-Heusler ZrNiSn is 1,435 ˚C [*28*]. This creates the need for high temperature techniques such as arc melting [*29*], melt spinning [*30*], induction melting [*31*], optical floating zone solidification [*32*]. In all techniques where the ingot is cooled from a melt,

additional processing steps are necessary before a high quality TE material can be achieved. In most cases annealing followed by high temperature densification is required. Densification is usually done *via* Spark Plasma Sintering (SPS) or Hot Pressing (HP). Spark plasma sintering has the advantage that it is able to rapidly heat the materials from within, by passing electrical current directly through the samples. Typically, SPS can take as little as 15-30 minutes to achieve close to theoretical density. HP, on the other hand, can take many hours, sometimes as long as 6 hours to fully densify a sample. Additionally, rather than melting the components and solidifying, the half-Heusler phase can be obtained directly from solid state reaction [*33, 34*]. Ball milling can also be used to reduce the grain size and effectively reduce the thermal conductivity of HH alloys [*35*].

In most of these techniques, one to two weeks of annealing above 800 ˚C is necessary to remove high defect densities and produce a homogenous single phase. It was shown early on that the electrical properties of *M*NiSn compounds are highly dependent on annealing time [*5*]. Recently, new methods of synthesis have emerged, such as combustion synthesis. By using a controlled combustion wave, called Self-propagating High-temperature Synthesis (SHS), single phase HH alloys can be made within minutes [*36*]. SHS involves rapidly heating a well-mixed cold pressed cylinder of raw elements. The heating should be localized in one location, and fast enough to start chemical combustion of the elements. The process usually begins once the lowest melting point material (Sn in the case of *M*NiSn) melts. The other elements then dissolve into the melt and react. If the reaction is exothermic, and the heat released in the reaction is sufficient to melt the surrounding material, the reaction will then propagate along the length of the sample. The reaction is quick and easy to start, and can be carried out in air at ambient temperatures. This new technique holds great promise for making HH alloys cheaper and more suitable for industrial

commercialization. All of the techniques mentioned above have been used to produce high quality TE materials and no one technique has come to dominate the field.

The work contained in the following chapters will remain focused on *M*NiSn compounds. For more in-depth reviews, see the corresponding references [*37-40*].

Chapter 3 Density Functional Theory Calculations

3.1 Density functional theory

The search for new thermoelectric materials with higher efficiency, cheaper components, and better mechanical properties has necessitated the exploration of more complex materials combining three or more elements. The number of possible combinations of ternary compounds, if one only considers a 1:1:1 ratio of elements available in the periodic table, is 1,601,496 unique compounds. Therefore, it is highly desirable to be able to examine many different types of compounds quickly. Some experimental high-throughput techniques have been developed for this cause, however they are still expensive and limited in what types of compounds can be tested. A much more promising route is to screen many different compounds for their TE properties via computational simulations.

One computational method that has gained tremendous momentum over the past 30 years is Density Functional Theory (DFT) [*41-44*]. DFT is a powerful technique that allows for the accurate prediction of physical properties in a variety of materials and molecules. Here we describe the basic theory of DFT and then in section 3.2, the details of calculations used in predicting properties of half-Heusler alloys are described.

3.1.1 Schrödinger's Equation

The usual method for predicting observables in a quantum system requires solving Schrödinger's equation to find the wave function of the system, Ψ, and then calculating expectation values of observables, $A = \langle\Psi|\hat{A}|\Psi\rangle$. This method gives exact answer for any system, however, in practice it cannot be used in condensed matter systems due to how the complexity scales with the number of electrons in the system. To see this, take the non-relativistic single particle Schrödinger's eq.

$$\left[\frac{-\hbar\nabla^2}{2m} + v(\boldsymbol{r})\right]\Psi(\boldsymbol{r}) = E\Psi(\boldsymbol{r}) \tag{5}$$

with a particle of mass m in a spatially dependent potential, $v(\boldsymbol{r})$. This equations enables us to solve for the wave function as a function of position, $\boldsymbol{r}$. For many particles, this expression becomes,

$$\left[\sum_i^N \left(\frac{-\hbar\nabla_i^2}{2m} + v(\boldsymbol{r}_i)\right) + \sum_{i<j} U(\boldsymbol{r}_i, \boldsymbol{r}_j)\right]\Psi(\boldsymbol{r}_1, \boldsymbol{r}_2, \cdots, \boldsymbol{r}_N) = E\Psi(\boldsymbol{r}_1, \boldsymbol{r}_2, \cdots, \boldsymbol{r}_N) \tag{6}$$

where N is the number of electrons in the system and $U(\boldsymbol{r}_i, \boldsymbol{r}_j)$ is the potential arising from Coulombic electron-electron interactions. This equation has $3N$ variables, and in solids N is typically of the order of 10^{23} atoms. The goal of density functional theory is to form these equations in a more solvable manner by expressing the system as a functional of the charge density, $n(\boldsymbol{r})$.

3.1.2 The Hohenberg-Kohn theorem

The basic tenets of DFT were set by Hohenberg and Kohn in 1965 with the Hohenberg-Kohn theorem [*45*, *46*]. The theorem states that the ground state of a system is uniquely defined

by the ground state density, $n_0(\boldsymbol{r})$. This implies that the ground state wave function, $\Psi_0(\boldsymbol{r}_1, \boldsymbol{r}_2, \cdots, \boldsymbol{r}_N)$ can be expressed as a functional of $n_0(\boldsymbol{r})$. The theorem can be proved by the variational principle. The energy of a system is minimized only in the unique ground state Ψ_0, and this wave function can be used to calculate the observable $n_0(\boldsymbol{r})$. If we consider the energy E as a functional of the charge density, $E(n)$, the energy will then be minimized by the ground state density n_0. Any state with $n \neq n_0$ must also have $\Psi \neq \Psi_0$, and therefore have energy $E > E_0$. The energy of the system can be expressed as

$$E(n) = T(n) + U(n) + V_{ex}(n) \tag{7}$$

where $T(n)$ is the kinetic energy, $U(n)$ is the electron-electron interaction potential, and $V_{ex}(n)$ is determined by the lattice geometry, which is known for a given system. We now need to use approximations to determine $T(n)$ and $U(n)$. Note that the functional $E(n(\boldsymbol{r}))$ only depends on the form of $n(\boldsymbol{r})$ and the three spatial coordinates.

3.1.3 The Kohn-Sham equations

The Kohn-Sham equations are what enable practical use of DFT for computation. Essentially they allow us to transform an interacting manybody system into a non-interacting system with an effective potential [*46*].

First we define a new fictitious system of N non-interacting electrons. This system is described by an anti-symmetric wave function made up of single electron orbitals, φ_i, which are chosen so that they correctly reproduce the ground state density:

$$n(\boldsymbol{r}) = \sum_{i}^{N} |\varphi_i(\boldsymbol{r})|^2 \tag{8}$$

With these new orbitals, we can solve for the non-interacting kinetic energy, T_s, and the classical Coulomb electron-electron term, U_h, as follows

$$T_s(n) = -\frac{\hbar^2}{2m}\sum_i^N \langle \varphi_i(\boldsymbol{r})|\nabla^2|\varphi_i(\boldsymbol{r})\rangle \ , \ U_h(n) = \frac{1}{2}\iint \frac{n(\boldsymbol{r}_1)n(\boldsymbol{r}_2)}{|\boldsymbol{r}_1 - \boldsymbol{r}_2|} d\boldsymbol{r}_1 d\boldsymbol{r}_2 \tag{9}$$

Substituting these equations into (7), we can rewrite the energy in terms of the single electron orbital kinetic and potential energies

$$E(n) = T_s(n) + U_h(n) + V_{ex}(n) + E_{xc} \tag{10}$$

where we define the Exchange-Correlation energy as

$$E_{xc} = [T(n) - T_s(n)] + [U(n) - U_h(n)] \tag{11}$$

The exchange-correlation energy is a grouping of the errors resulting from using the non-interacting T_s and U_h. These errors arise from two major contributions: the exchange and correlation errors. The exchange error can be thought of as the error introduced by ignoring the Pauli exclusion principle in the kinetic energy term [*42*]. The correlation error is caused by the use of independent orbitals, φ_i, since in the real system electron orbitals are statistically correlated, and electron wave functions tend to repel each other to avoid interaction. The E_{xc} contains all of the manybody information of the system that was left out of T_s and U_h.

Given the energy in (10), it is possible to write down a non-interacting Schrödinger's Equation to solve for the φ_i by grouping potential energy terms into an effective potential

$$v_s = v_{ex}(\boldsymbol{r}) + v_h(\boldsymbol{r}) + v_{xc}(\boldsymbol{r}) \tag{12}$$

where

$$v_{xc}(\boldsymbol{r}) = \frac{\delta E_{xc}(n(\boldsymbol{r}))}{\delta n(\boldsymbol{r})} \tag{13}$$

and φ_i can be solved for in the standard way

$$\left[\frac{-\hbar\nabla^2}{2m} + v_s(\boldsymbol{r})\right]\varphi_i = \epsilon_i\varphi_i \tag{14}$$

This expression is exact as long as the exact local potential $v_s(\boldsymbol{r})$ is used. However, the form of E_{xc} remains unknown, thus the effective potential $v_s(\boldsymbol{r})$ must be approximated. The problem has been reduced to solving the non-interacting Schrödinger's equation. The combination of (12) and (14) are known as the Kohn-Sham equations [*46*]. All that remains for practical use of DFT is an accurate approximation of E_{xc}.

3.1.4 Exchange-Correlation approximations

Several different approximations have emerged over the years that are computationally viable. The approximations we will briefly discuss are the Local Density Approximation (LDA) and the Generalized Gradient Approximation (GGA).

The local density approximation assumes that the exchange-correlation energy can be written as a functional of the electron density, $E_{xc} \rightarrow E_{xc}(n)$ [*46*]. This approximation is made so that the results calculated from a homogeneous electron gas can be used. The homogeneous electron gas was studied by Thomas and Fermi in the early 1920's, and the results can be applied to inhomogeneous systems in some respects. The exchange energy can be calculated explicitly assuming that small regions essentially have a homogeneous density, and then summing over all such small regions to calculate the total exchange energy. The correlation energy is still difficult to solve for using this approximation, and results are generally parameterizations of quantum Monte Carlo simulations of a homogeneous electron gas. LDA can be used to reliably calculate

vibrational frequencies, elastic moduli, and phase stability of solids. However, LDA's performance drops when dealing with electronic band gaps, binding energies, diffusion energies, and chemical reactions. LDA results also tend to slightly underestimate the lattice parameter of solids [*47*].

The generalized gradient approximation improves upon LDA by expressing the exchange-correlation energy as a functional of the local electron density and its gradient, $E_{xc} \rightarrow E_{xc}(n, \nabla n)$. This functional improves the accuracy of the approximation but also adds computational complexity. In order to make the approximation more flexible and accurate, the energy is written as a functional of some generalized function, *f*, which depends on the electron density and its gradient:

$$E_{xc}^{GGA} = \int n(\boldsymbol{r}) f(n(\boldsymbol{r}), \nabla n(\boldsymbol{r}))\, d\boldsymbol{r} \tag{15}$$

where $f(n(\boldsymbol{r}), \nabla n(\boldsymbol{r}))$ is a function that is determined by calculating fitting parameters to certain test systems and constraints. A popular form of f was developed by Perdew, Burke, and Ernzerhof (PBE) in 1996 [*48*]. The improvements gained by using GGA over LDA allows for accurate calculations of chemical bonding and diffusion energies, however, predictions of intermolecular bonds such as Van der Waals forces are still unreliable [*42*].

Other more complicated exchange-correlation approximations have since been developed. The class of hybrid-functionals incorporate portions of exact exchange energies from Hartree-Fock theory that tend to be far better predictors of electronic density of states and band structure in semiconductors. In the following chapters, the work is done exclusively within GGA using the PBE parameterization.

3.2 Ab Initio simulation methods

3.2.1 General Methods

All calculations done in the following research used density functional theory as implemented in the Vienna *Ab Initio* Simulation Package (VASP) [*49*]. Calculations used GGA pseudo potentials as parameterized by Perdew, Burke, and Ernzerhof (PBE) [*48*]. The projector augmented wave method [*50*] was used and the energy cutoff for plane waves included in the basis set was taken to be 1.5 times larger than the largest `ENMAX` of the GGA-PBE pseudo potentials used in the simulation.

For each material of interest for DFT calculations, the material's sensitivity to several VASP input parameters was tested before more complicated calculations were attempted. The process begins by entering the material's crystal structure and atomic basis into a file named `POSCAR`. An example `POSCAR` file for the ZrNiSn compound with a half-Heusler crystal structure is given below.

```
ZrNiSn
   1.00000000000000
     0.0000000000000000   3.0766718734936536   3.0766718734936536
     3.0766718734936536   0.0000000000000000   3.0766718734936536
     3.0766718734936536   3.0766718734936536   0.0000000000000000
   Zr   Ni   Sn
     1     1     1
Direct
  0.0000000000000000  0.0000000000000000  0.0000000000000000
  0.2500000000000000  0.2500000000000000  0.2500000000000000
  0.5000000000000000  0.5000000000000000  0.5000000000000000
```

Detailed descriptions of the formatting conventions for each line can be found in the VASP manual. The `POSCAR` file can either be constructed using an existing CIF file from an online data

base, such as MaterialsProject.org or from scratch by using crystal structure information and experimental (or best guess) lattice parameters.

The material now needs to be tested for k-point energy convergence. This is done simply by creating multiple VASP runs, each with a different density of k-points in the first Brillouin Zone (BZ). For initial k-point convergence and subsequent relaxation steps, we use a Monkhorst-Pack mesh of k-points to sample the BZ [*51*]. Below is an example of a `KPOINTS` file with a $15 \times 15 \times 15$ Γ-point centered mesh.

```
ZrNiSn Kpoints
0
Gamma
15 15 15
0 0 0
```

For the example of ZrNiSn, k-point meshes of dimensions $3 \times 3 \times 3$ to $15 \times 15 \times 15$ were tested, and it was found that the formation energy converged to within 1 meV for meshes of size $7 \times 7 \times 7$ or greater, as shown in Figure 5. The formation energies are calculated by allowing for full relaxation of atomic position, cell shape and cell volume (`ISIF = 3`). For metals, it is common to use the first order Methfessel-Paxton method (`ISMEAR = 1`) to approximate the partial occupancy of energy states near the Fermi level. In this case, the artificial temperature parameter, `SIGMA`, must be tested for convergence such that the free energy, F, and the energy, E_0, are converged ($F - E_0 \leq 1$ meV). A common value used is `SIGMA = 0.2`, where the units of SIGMA are in eV. For semiconductors, it is recommended to use the tetrahedron method with Blöchl corrections (`ISMEAR = -5`) [*52*].

After the converged k-point mesh and smearing values have been found, further relaxation of the structure is required to accurately predict the equilibrium lattice parameter and atomic

positions. The crystal geometry should be allowed to fully relax (`ISIF = 3`) and the electronic steps should be converged to $\Delta F \leq 10^{-7}$ eV. This can be set through the `EDIFF` parameter in the `INCAR` file. An example `INCAR` file is given below.

```
PREC = Accurate # precision
ENCUT = 550     # global energy cutoff
LREAL = .FALSE. # real space projection yes/no
ISMEAR = -5   # method to determine partial occupancies (relaxation)
SIGMA = 0.2     # smearing width (eV), only used with ISMEAR = 1
NSW = 61        # number of ion relaxation steps
IBRION = 2      # conjugate gradient relaxation (2)
ISIF = 3        # set degrees of freedom for cell relaxation
LWAVE = .FALSE. # do not write out WAVECAR file
NPAR = 2        # parallelization
EDIFF = 1.0e-7  # energy convergence cutoff, default 1.0e-4
```

The calculation is then rerun multiple times, typically 2 or 3 times, increasing the `EDIFF` value from the default `1.0e-4` to `1.0e-7`. After the completion of a run, the output structure file, `CONTCAR`, is copied to the input structure file, `POSCAR`. This process is repeated until the VASP run converges after a maximum of 3 ionic relaxation steps. We consider the final OUTCAR file as the "fully relaxed" unit cell and can extract the DFT predicted lattice parameter from the file.

New materials should be checked to see if magnetic effects are prevalent. This can be done by allowing the electrons to obtain a spin polarization by setting the `INCAR` parameter `ISPIN = 2`. The initial magnetic moment of each atom in the basis needs to be set via the MAGMOM parameter. In the case of the half-Heusler and full-Heusler alloys studied, none were found to have appreciable magnetism, and calculations were carried out without considering the spin polarization of electrons.

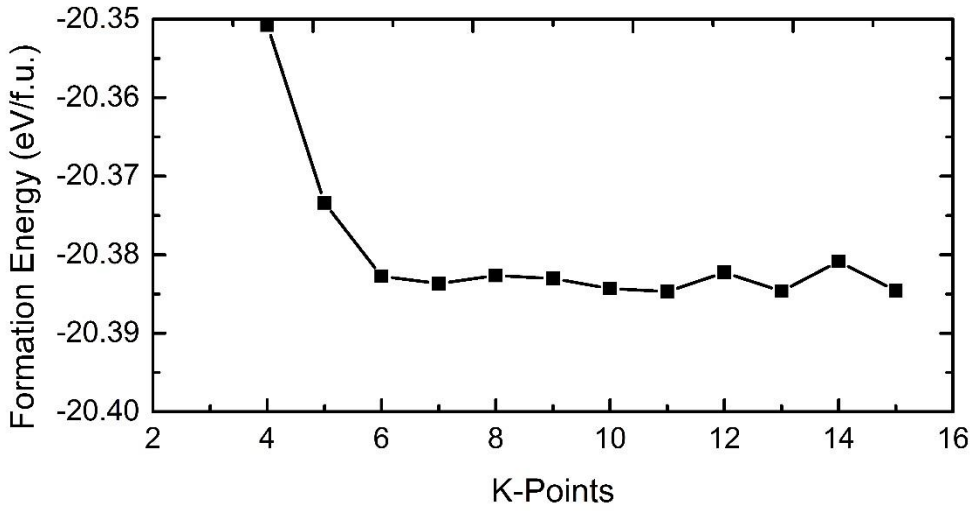

Figure 5. Plot of ZrNiSn formation energy as a function of k-point grid dimension.

3.2.2 Density of states and band structure calculations

In order to calculate the Density of State (DOS) it is important to do a single self-consistent (`ICHARG = 2`) static run (NSW = 0) with a high k-point density, such as $25 \times 25 \times 25$ for ZrNiSn, to produce a CHGCAR file. After the self-consistent run is complete, the run should be repeated as a non-selfconsistent calculation (`ICHARG = 11`) and the resulting `DOSCAR` file will hold the proper DOS information. An example INCAR file of the non-selfconsistent run to calculate the DOS is given below.

```
PREC = High     # precision
ENCUT = 550     # global energy cutoff
LREAL = .FALSE. # real space projection yes/no
ISMEAR = -5       #=1 for normal relaxation, =-5 for tetrahedral
method
NSW = 0         # number of ion relaxation steps
IBRION = -1    #conjugate gradient (=2 normal, =-1 for static run)
ISIF = 3        # set degrees of freedom for cell relaxation
LWAVE = .FALSE. # do not write out WAVECAR file
NPAR = 2        # parallelization

ICHARG=11       # =2 selfconsistent run, =11 non-selfconsistent
```

```
EMIN=-10        #Set starting energy for DOS
EMAX=15         #Set max energy for DOS
NEDOS=1000      #Number of data points
```

Band structure calculations can be based off of the same self-consistent run used in calculating the DOS. The band structure calculation should use a non-selfconsistent run and the k-point mesh should be replaced with a k-point path that covers the relevant symmetry lines through the BZ, following the standards set by Setyawan and Curtarolo [*53*].

3.2.3 Phonon dispersion calculations

Phonon dispersion curves and other vibrational properties were calculated by fitting force constants to Hellman-Feynman forces calculated in VASP on supercells with displaced atoms. We used the open source PHONOPY code [*54*] to generate displaced supercells and fit the force-displacement data to compute the dynamical matrix. In all calculations we used a displacement distance of 0.03 Å and supercells of dimension $2 \times 2 \times 2$ and $3 \times 3 \times 3$ primitive cells. Before creating the displaced supercells, the primitive cells were relaxed such that all forces were less than 1×10^{-5} eV/ Å, using the `EDIFFG` tag in the `INCAR` file. Born Effective Charge corrections were calculated using density functional perturbation theory (DFPT) [*55, 56*] in VASP. Resultant phonon density of states are calculated using a dense k-point mesh $(31 \times 31 \times 31)$, and dispersions curves are calculated along the high symmetry lines of the first BZ, similar to the electronic band structure calculations. Any 'soft modes' which are indications of structural instability, will be displayed as having negative frequency for ease of viewing. In this situation, the negative frequencies actually represent complex frequencies, which show that the structure is in an unstable maximum of energy rather than a minimum that would provide the usual restoring force.

3.2.4 Migration barriers and activation energy calculations:

We calculated the migration barriers associated with the self-diffusion of various atoms within the HH matrix. To do this we assumed the diffusion happened *via* a vacancy mechanism, where a vacancy located on the corresponding site, Va, swaps with a neighboring atom. This mechanism can be thought of as two separate processes: first a vacancy must form in the matrix, and then a vacancy-atom exchange must occur. The diffusion coefficient in solids, can be expressed as [*57*],

$$D = D_0 \exp\left[\frac{-E_a}{k_B T}\right] \tag{16}$$

where E_a is an activation energy, k_B is the Boltzmann constant, T is the absolute temperature, and D_0 is the diffusion prefactor, which depends on the jump distance, effective jump frequency, and the vibrational entropy of vacancy formation [*58*]. The prefactor D_0, in this form, has a weak temperature dependence arising from anharmonic vibrational excitations. The prefactor is commonly calculated from first principles within the harmonic approximation [*59, 60*]. The activation energy of vacancy-mediated diffusion is made up of two contributions, $E_a = \Delta E_V + \Delta E_m$, where ΔE_V is the formation energy of a single vacancy in the matrix, and ΔE_m is the migration energy. In many cases, it is sufficient to calculate only the activation energy and assume a constant value for the prefactor, D_0.

The migration energy was calculated using the DFT calculations along the diffusion pathway. The energy of migration, ΔE_m, is defined as the difference in energy between the initial state and the transition state. The transition state is the "saddle point" between the initial state and the final state defined as the highest energy point of the lowest energy migration path from the initial to the final state. The migration barrier energy of the HH compounds was found by first

fully relaxing $3 \times 3 \times 3$ supercells of the initial and final states. Then, Nudged Elastic Band (NEB) calculations were performed in VASP to find the location and energy of the saddle point.

Nudged Elastic Band calculations are used to create and calculate the energy of intermediate structures along the migration path from the initial to final state. This is done by adding artificial "spring like" forces that keep the atoms at their desired location in the migration path, while at the same time allowing them to relax in directions perpendicular to the path. NEB calculations were performed using the built in NEB functionality in VASP. It is often better to start with a small number of images (1 to 3) for the initial NEB run. An example INCAR file is given below.

```
PREC = Medium    # precision medium
ENCUT = 550      # global energy cutoff
LREAL = .FALSE.  # real space projection yes/no
ISMEAR = 1       # method to determine partial occupancies
SIGMA = 0.2      # smearing width (eV) - keep T*S < 1 meV/atom
NSW = 10         # number of ion relaxation steps
LWAVE = .FALSE.  # do not write out WAVECAR file
ELMIN = 5        # Min number of steps
LCHARG = .FALSE. #determines if the charge densities are written.

#Nudged Elastic Band Tags#
EDIFF = 1e-6     # electronic convergence, default is 1e-4
EDIFFG = -0.01   # max force 0.01 eV/A
IMAGES = 1     # num of steps between initial & final configurations
SPRING = -5      # spring constant
IBRION = 1       # RMM-DIIS method
ISIF = 2         # atomic positions relax, no volume or shape
```

After the location of the saddle point along the reaction path is found, the saddle point structure can be further relaxed to find the lowest possible bound on the migration energy. To do this, place the migrating atom in the saddle point location, while leaving the rest of the cell unchanged from its initial configuration. This cell can then be fully relaxed and, in theory, the

migrating atom should stay at its local maxima, while the other atoms relax, further lowering the energy. This method sometimes provides an even lower bound on the migration energy, although one has to double check to make sure the migrating atom has stayed in position, and that the structure has not drastically changed. The calculation of equilibrium vacancy concentrations in compounds and alloys [*61-67*], especially those that are semiconductors [*65*] is difficult as the vacancy formation energy can depend on the charge state of the crystal. In this work, vacancy formation energies from other more thorough studies were used rather than attempting to calculate them from scratch.

Chapter 4 *Ab-initio* Phase Diagrams

The thermoelectric efficiency of half-Heusler alloys can be dramatically raised by doping in order to optimize the carrier concentration and by isoelectronic substitution, which can lower the lattice thermal conductivity *via* mass fluctuations. In both methods, it is important to know what the solubility limits of defects are inside the HH matrix. Consequently, phase diagrams are an extremely valuable tool in understanding and controlling how dopants are incorporated in the HH materials. The phase diagram is a compact way of representing which phases are thermodynamically stable under equilibrium conditions for a given temperature and composition. Such information can be found by extensive experimental work, where compounds of different composition are synthesized and annealed at varying temperatures, however, this type of investigation is extremely time consuming and expensive. Furthermore, the synthesized material depends on the kinetic processes of synthesis, which can obscure the fundamental thermodynamic processes we aim to understand. Therefore, it is highly desirable to have an accurate theoretical method for determining the phase diagram of a particular composition space. Theoretical methods that employ DFT as the backbone for calculations have been developed to create full thermodynamic phase diagrams as functions of temperature and composition in a timely and cost effective manner.

The phase diagram of a system can be constructed by finding the free energy of various competing phases as a function of composition and temperature. Systems with substitutional

degrees of freedom, such as an alloy of two materials, require both accurate formation energy calculations and statistical mechanics techniques, which can account for configurational entropy, in order to calculate finite-temperature thermodynamic properties. The cluster expansion method [*68*] bridges the gap between the accurate but costly DFT formation energy calculations, and the macroscopic statistical mechanics tools, such as Monte Carlo simulations or mean field approximations.

The free energy of a solid, *F*, is given by

$$F = -k_B T \ln(Z), \qquad Z = \sum_s \exp\left(\frac{-E_s}{k_B T}\right) \tag{17}$$

where *Z*, the partition function is determined by a sum over all possible configurational, electronic, and vibrational states of the solid. Here, E_s is the energy of state s, k_B is the Boltzmann constant, and T is the absolute temperature. Often, in investigations of phase diagrams, the effects of vibrational and electronic degrees of freedom are considered small and can be neglected [*69*]. In this case, the sum in (17) is only over the configurational degrees of freedom.

Consider a specific sublattice in a crystal that can be occupied by either atom *A* or atom *B*. The number of possible configurations that *A* and *B* atoms can be arranged on the lattice sites increases with the size of the lattice. Usually we are interested in the arrangement of atoms in the $A_{1-x}B_x$ alloy for a given composition, *x*. One possible configuration is shown in Figure 6(a), where only two FCC conventional cells are shown. The formation energy of all possible configurations of *A* and *B* atoms over an arbitrarily large number of sites is required to solve for the free energy using (17). This is not possible to compute using DFT, as the vast number of possible configurations is far too costly computationally. Luckily, there are several approximations we can use that make it possible to accurately predict the formation energy for any given configuration.

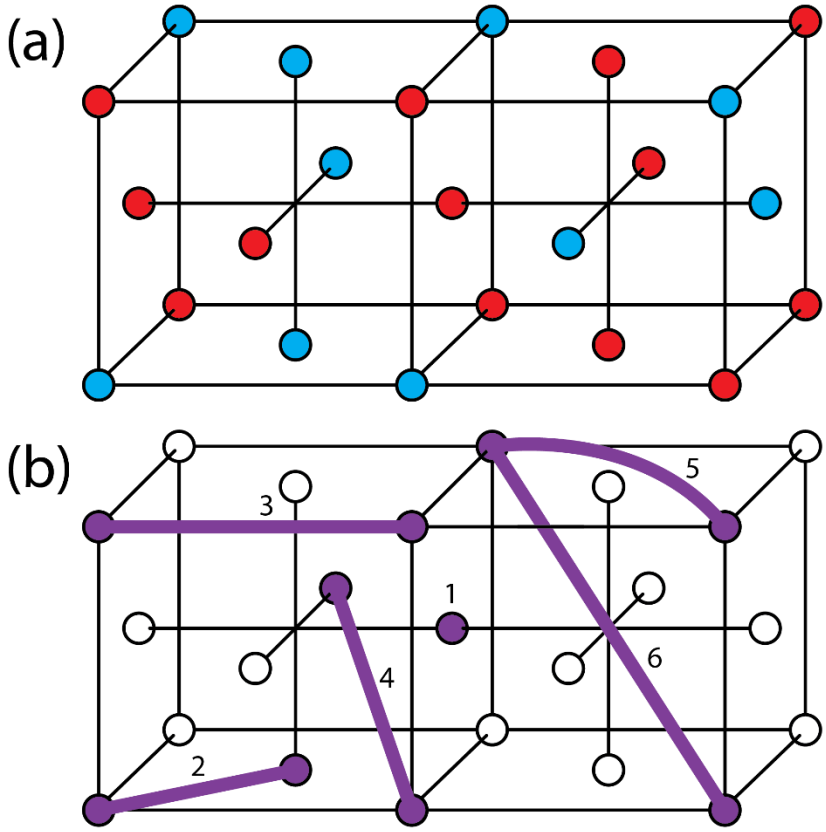

Figure 6. (a) Example configuration of twenty three atoms A and B (red and blue respectively) in an FCC lattice configuration. (b) Examples of possible singlet and pair clusters on an FCC lattice.

The cluster expansion requires relatively little DFT calculations. In constructing a cluster expansion, each site is assigned an occupation variable, σ_i, which takes a value of 1 or -1 if site i is occupied by atom *A* or *B*, respectively [*70*]. We then create groups of occupation variables, called a cluster and denoted as β. Clusters can range from just one site to groups including multiple sites. For example, a cluster that includes two sites $\beta = (\sigma_i, \sigma_j)$ is called a pair, and a cluster that includes three sites $\beta = (\sigma_i, \sigma_j, \sigma_k)$ is called a triplet, and so on. Some example possible pair clusters on an FCC lattice are shown in Figure 6(b). The formation energy can then be expressed

as an expansion in terms of cluster basis functions, $\Gamma_\beta(\vec{\sigma})$, which are polynomials of the discrete occupation variables, σ_i [*68, 71*]. The configurational energy then takes the form

$$E(\vec{\sigma}) = V_0 + \sum_i V_i\sigma_i + \sum_{i,j} V_{i,j}\sigma_i\sigma_j + \sum_{i,j,k} V_{i,j,k}\sigma_i\sigma_j\sigma_k + \cdots = V_0 + \sum_\beta V_\beta\Gamma_\beta \tag{18}$$

where V_0 and V_β are coefficients called effective cluster interactions (ECI) and have a constant value. Here, the sum in Eq. (18) is over all possible clusters, β. However, this infinite sum can be drastically truncated by eliminating terms that have very small contributions to the formation energy. For example, the ECI tend to converge to zero for clusters that involve lattice sites far away from each other, such as more than three times the lattice parameter of a material. Also, clusters that involve a large numbers of sites, such as greater than five sites, tend to have very small ECI. Therefore, this sum can be truncated to a relatively small number of clusters, and generally only clusters that contain close range pairs or triplets are included.

The ECI can then be solved for by fitting Eq. (18) to the calculated DFT formation energies of various configurations. To attain an accurate fitting of the ECI, only fifty to eighty separate DFT configurational energies are required for a binary system, and around 300 configurations are required for a ternary system. This is easily done with modern computing power, and in practice using 12 or 24 processors in a computing clusters required around one month to complete the calculations for half-Heusler alloy systems. The ECI are fit by using a genetic algorithm. The genetic algorithm is required to optimally determine which clusters are most important and should be included in the expansion. To do this, sets of clusters are randomly generated and evaluated by using a cross validation, CV, score. A set of clusters, called a genome, is usually represented in

binary, with a 1 representing that a cluster is included and a 0 representing that a cluster is not included. Top scoring genomes of an individual set are then mated together to produce 'offspring' by swapping a certain fraction of their genes or randomly mutating (i.e. flipping a bit from 0 to 1). This new generation is again tested and ranked based on CV score. The process repeats until population members achieve CV scores within a specified tolerance, or until the maximum number of allowed generations has passed.

The CV score is found using the 'leave one out' method, described as follows. The ECI included in a genome are trained on all but one of the configurations used in the DFT calculation. The ECI resulting from the training are then used to predict the energy of the configuration which was left out of the original training set. The CV score is then found by repeating this process for the same genome using different training sets, until all DFT calculated configurations have been 'left out' once. The average error between the ECI predicted formation energy and the DFT calculated energy is defined as the CV score. Typically, the CV score should be less than 10 meV and in the case of this work was never larger than 6 meV.

Once the optimal fit is obtained, the energy of any configuration, no matter its size or arrangement, can be calculated to a high accuracy using the truncated version of Eq. (18), which now is a sum only over the clusters used in the optimal fit. See Ref. [*72*] for a more detailed description of cluster expansions methods.

A complete description of the formation energy of different configurations along a composition space $A_{1-x}B_x$, allows us to determine the ground state structure. The ground state of a material is determined by the lowest energy structures on the "hull", which is defined by the common tangent of the formation energies. From this, we can determine at 0 Kelvin, what the equilibrium microstructure of the material is. However, in order to predict the equilibrium phases

of a system at non-zero temperatures, it is necessary to consider more than just the formation energy of a given configuration.

In experimental conditions, we must consider that atomic diffusion is possible within the system. From thermodynamics, we know that for a system in thermal and diffusive contact with a reservoir at a temperature, *T*, and chemical potential μ, the probability of states occurring is governed by the Gibbs factor. Thus, the ratio of the probability of being in a particular state, *1*, with N_1 particles and energy E_1, over another, *2*, is given by

$$\frac{P(N_1, E_1)}{P(N_2, E_2)} = \frac{\exp\left(\frac{\mu N_1 - E_1}{k_B T}\right)}{\exp\left(\frac{\mu N_2 - E_2}{k_B T}\right)} = \exp\left(\frac{-\Delta H}{k_B T}\right) \tag{19}$$

which is just the ratio of Gibbs factors [*73*]. We define the enthalpy $H_i = E_i - \mu N_i$, and $\Delta H = H_1 - H_2$ as the difference in enthalpy between states *1* and *2*. In Monte Carlo (MC) simulations, we implement this fundamental thermodynamic law via the Metropolis algorithm [*74*]. This algorithm is as follows: 1) randomly generate a new state of the system; 2) calculate the energy of this new state using the ECI to evaluate the local environment of the site; 3) if the new state has lower enthalpy that the current state, the change is immediately accepted, but if the new state has higher enthalpy than the current state (i.e. ΔH is positive), then the new state will be accepted with the probability $P = \exp\left(\frac{-\Delta H}{k_B T}\right)$. If each lattice site in the MC simulation is visited a sufficient number of times, the Metropolis algorithm guarantees that the system will tend to thermodynamic equilibrium. Thus, the MC method simulates the randomness of systems at finite temperature and acts as an artificial entropy. In practice, when running the simulation, each site is visited around 3000-5000 times, and the simulation takes place on over 3000 lattice sites. In order to find the actual phase boundaries with respect to temperature and composition, multiple MC runs must be

made at varying temperature and chemical potentials. From the MC results, thermodynamic averages provide the grand canonical energy, concentration *x*, and structure of crystal. Through an integration, the Gibbs free energy can be obtained and thus the equilibrium concentrations are found. By plotting the equilibrium concentrations for multiple temperatures, a phase diagram is constructed, as shown in Figure 7.

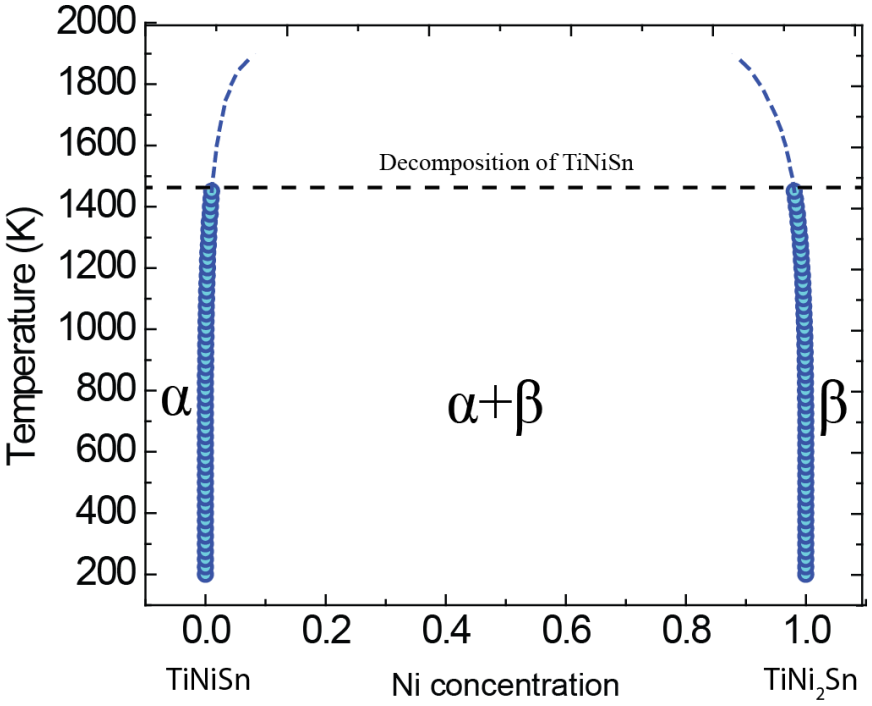

Figure 7. Calculated pseudo-binary phase diagram of $TiNi_{1+x}Sn$ from x = 0 to 1. Circles show calculated phase transition points, between which, a two phase coexistence is stable. The MC method is limited to temperatures below the decomposition point of TiNiSn, above which the phase diagram can no longer be considered pseudo-binary.

Chapter 5 Phase Separation of Full-Heusler Nanostructures in Half-Heusler Thermoelectrics and Vibrational Properties from First-principles Calculations

5.1 Introduction

A *ZT* value greater than 2 has still not been achieved in the half-Heusler class of materials. Recently, a new strategy has emerged that takes advantage of the structural similarities of the HH and FH structures as well as their differing electronic properties. It was shown that by using an overstoichiometric amount of Ni in bulk HH, the excess Ni creates FH nano-structures that make coherent or semi-coherent boundaries with the HH matrix [*33, 34, 75-79*]. Coherent nanostructures are thought to be less detrimental to the electronic transport and thus are beneficial for TE materials [*80*].

Makongo and coworkers [*34*] found that adding 2% to 3% excess Ni created semi-coherent FH nano-structures (see Figure 8), which simultaneously increased the Seebeck coefficient and the electrical conductivity while slightly decreasing the lattice thermal conductivity. This resulted in an overall 250% increase of *ZT* compared to the HH bulk at a temperature of 775K. The authors attributed this enhancement to an energy filtering effect that occurs at the interfaces of the metallic nanoparticles and the bulk semiconducting matrix.

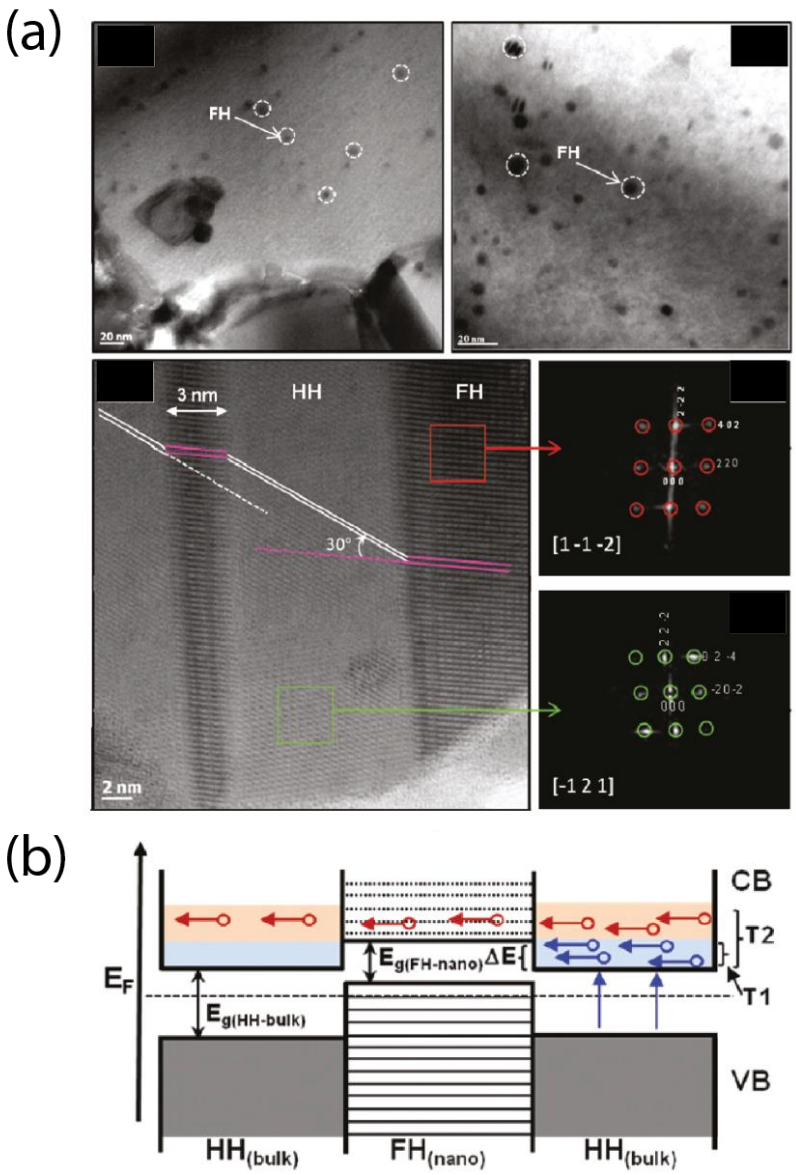

Figure 8. (a) TEM images of HH with excess Ni forming semi-coherent interfaces with the bulk HH matrix. (b) Schematic of the electronic bands across the nanostructure-bulk interface. The potential barrier created at the interface could enable an energy filtering process. (a) and (b) shown with permission from Makongo *et al*., JACS 133, 18843 (2011).

Much is still unknown about the processes that govern the formation of the nanoparticles and the properties at their interfaces that contribute to the enhanced power factor. Furthermore, to be useful in waste heat recovery applications, small fractions of FH metallic nanoparticles must be

thermodynamically stable at high temperature within the HH matrix to prevent performance degradation during operation and thermal cycling.

Many theoretical studies using DFT were done regarding aspects of the HH-FH system. The formation enthalpy of defects was examined for the *M*NiSn (*M* = Ti, Zr, or Hf) structures. Studies found that, of the many different defects that can occur in a HH structure, excess Ni filling a vacant site results in the lowest change in formation enthalpy [*81-84*]. While the low formation enthalpy of excess Ni indicates that such a defect is likely to form, it remained unclear what the resulting microstructure would be. The work of Do *et al.* [*83*] showed that the formation energy of a supercell with two excess Ni atoms was minimized if the Ni atoms occupied adjacent vacancy sites as opposed to sites far away from each other. This was promising qualitative evidence that excess Ni atoms would preferentially form a secondary full-Heusler phase as opposed to a solid solution. However, it was still unknown what the behavior of Ni defects at non-zero temperatures is. Furthermore, predictions of the maximum solubility limits of Ni in $M\mathrm{Ni}_{1+x}\mathrm{Sn}$ as a function of temperature would reveal if the experimentally observed nanostructures would remain stable during prolonged use at high operating temperatures.

This chapter presents the results of a study of the equilibrium phase diagram along the pseudo-binary composition axis between *M*NiSn and $M\mathrm{Ni}_2\mathrm{Sn}$ [*85*]. First-principles electronic structure calculations are combined with a Cluster Expansion (CE) method and statistical mechanics simulations to predict phase stability at finite temperature as a function of concentration x in $M\mathrm{Ni}_{(1+x)}\mathrm{Sn}$. Vibrational properties of HH and FH structures are also investigated from first principles. It is found that cubic $\mathrm{TiNi}_2\mathrm{Sn}$ is dynamically unstable while the cubic forms of $\mathrm{ZrNi}_2\mathrm{Sn}$ and $\mathrm{HfNi}_2\mathrm{Sn}$ are predicted to be dynamically stable. Structural instabilities have been observed in FH compounds, such as $\mathrm{MnNi}_2\mathrm{Ga}$ before and were explored for their usefulness as potential

magnetic shape memory devices [*86-88*]. The unstable phonon modes predicted in cubic $TiNi_2Sn$ differ qualitatively from those of $MnNi_2Ga$.

5.2 Configurational formation energies

The clusters approach to statistical mechanics (CASM) software package [*90, 91*] was used to enumerate symmetrically distinct Ni-vacancy configurations over the vacancy sublattice of HH *M*NiSn, to fit the cluster expansion coefficients to fully relaxed DFT energies, and to perform the Monte Carlo simulations. In this work, cluster expansions are parameterized for each $MNi_{1+x}Sn$ system. Each expansion was fit to over 40 DFT calculated structures with supercell volumes up to 5 times the primitive cell. The optimized set of ECI was determined by minimizing a cross validation (CV) score calculated using the "leave one out" method. The CV scores for each cluster expansion were smaller than 6 meV/site.

	Lattice parameter (Å)		HH-FH Mismatch (%)
	DFT	Exp	DFT
TiNiSn	5.945	5.92	2.97
ZrNiSn	6.153	6.11	2.61
HfNiSn	6.113	6.07	2.62
$TiNi_2Sn$	6.116	6.09	
$ZrNi_2Sn$	6.314	6.27	
$HfNi_2Sn$	6.273	6.24	

Table 1. DFT calculated lattice constants from this work compared to experimental values, Exp [*89*], and the lattice mismatch between the HH and FH compounds relative to the HH lattice constant.

Fully relaxed lattice constants for the HH and FH structures are shown in Table *1*. The calculated DFT parameters overestimate the experimental values [*89*] by a small margin (0.5-0.7%) as is to be expected with DFT-GGA.

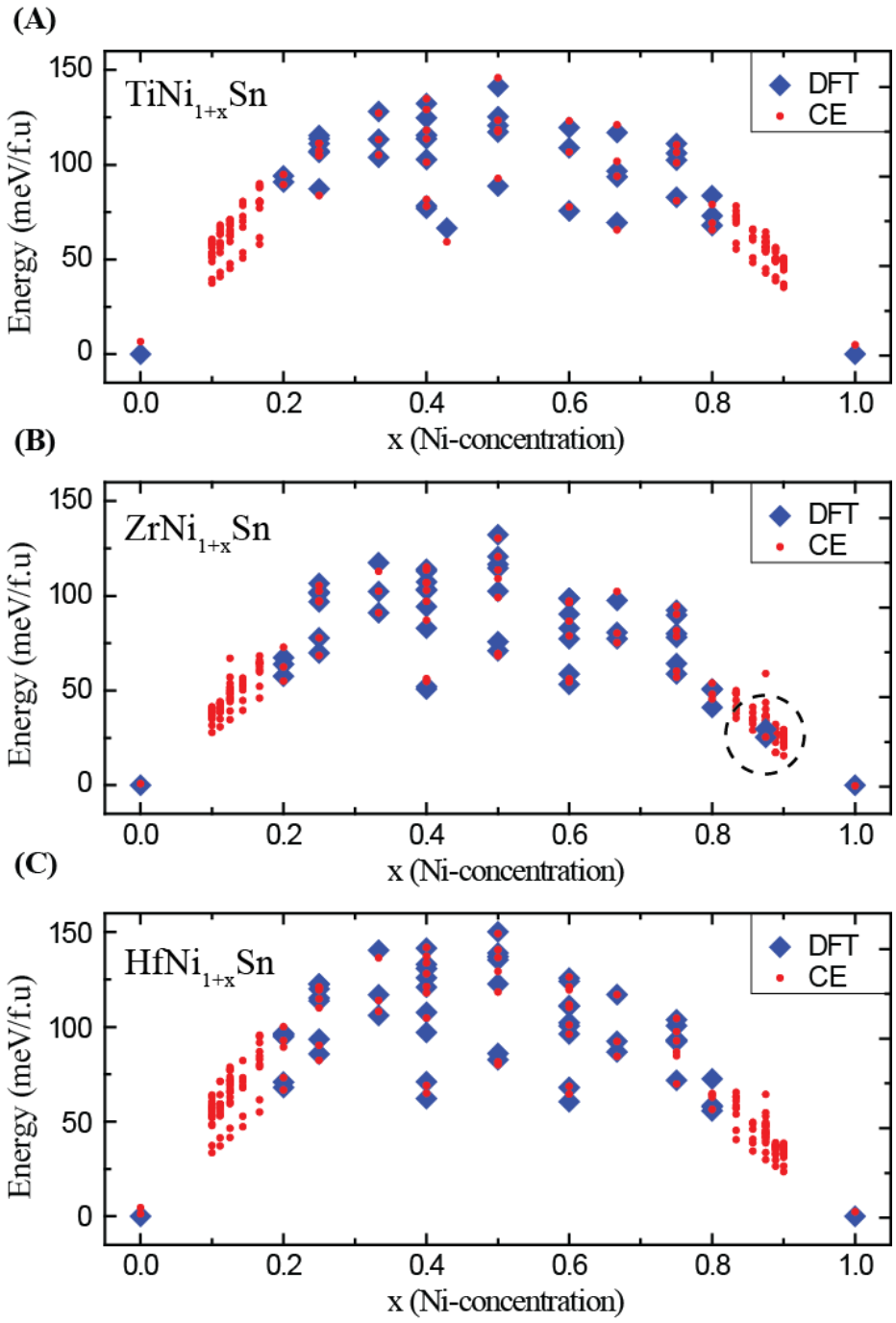

Figure 9. Formation energy per formula unit cell relative to the ground states are shown for $TiNi_{1+x}Sn$ (A), $ZrNi_{1+x}Sn$ (B), and $HfNi_{1+x}Sn$ (C). DFT calculated energies are shown as blue diamonds. The Cluster Expansion (CE) predicted energies for the DFT structures and further predictions for configurations up to $x = 0.1$ and $x = 0.9$ are shown as red dots. The dashed circle in (B) indicates specific configurations discussed in the text.

The DFT formation energies relative to HH *M*NiSn and FH *M*Ni_2Sn are shown in Figure 9 as blue diamonds. The cluster expansion predicted energies of different Ni-vacancy arrangements over the vacancy sublattice of HH MNiSn are shown as red dots.

The formation energies of the configurations in Figure 9 are all positive relative to the HH and FH structures. This implies that no solid solution or intermediate ordered arrangement of Ni and vacancies is stable between x = 0 and 1 at zero temperature. From only the DFT calculated energies, it can be predicted that below a certain temperature, called the critical temperature, a two phase coexistence region between HH and FH should exist. The cluster expansions fit to the DFT formation energies included 11, 12, and 14 ECI, resulting in CV scores of 5.7, 4.3 and 5.9 meV for $TiNi_{1+x}Sn$, $ZrNi_{1+x}Sn$, and $HfNi_{1+x}Sn$, respectively.

The DFT formation energies of $ZrNi_{1+x}Sn$ and $HfNi_{1+x}Sn$ exhibit a slight asymmetry around x = ½. The formation energy associated with adding Ni to the vacancy sublattice for HH ZrNiSn and HfNiSn is higher than that of adding vacancies to FH $ZrNi_2Sn$ and $HfNi_2Sn$, indicating that vacancy defects in the FH is less costly than Ni defects in HH structures, in agreement with previous calculations [*82*]. The formation energies of the $TiNi_{1+x}Sn$ system, by contrast, are far more symmetrical.

Figure 9 also shows formation energies predicted with the cluster expansion for Ni-vacancy arrangements in larger supercells than those calculated with DFT. Large supercells can accommodate Ni-vacancy configurations at more dilute concentrations (i.e., closer to $x = 0$ or $x = 1$). Supercells up to volumes of 10 times the primitive cell volume were predicted with the CE and correspond to the red dots in Figure 9 in the range of $0.1 \leq x \leq 0.2$ and $0.8 \leq x \leq 0.9$. The DFT

energies of several of the $ZrNi_{1-x}Sn$ configurations were predicted to have low energy by the cluster expansion at x = 0.875. Two of the configurations were calculated with DFT to further assess the accuracy of the cluster expansion (data circled by the dashed line in Figure 9(B)). The DFT results match the cluster expansion predictions within 4 meV/f.u, and provide a confirmation of the predictive power of the cluster expansion method on the HH class of materials.

5.3 Pseudo-binary phase diagrams

Calculated pseudo-binary HH-FH phase diagrams for $TiNi_{1+x}Sn$, $ZrNi_{1+x}Sn$, and $HfNi_{1+x}Sn$ are shown in Figure 10. The small black diamonds represent calculated phase boundaries while the dashed horizontal lines indicate experimentally observed HH melting points [*28*] (or decomposition point for TiNiSn). In all three systems, a large miscibility gap separates HH from FH. The persistence of the miscibility gap to high temperatures is a result of the relatively large formation energies of intermediate configurations compared to the formation energies of the HH and FH structures. In the $TiNi_{1+x}Sn$ phase diagram (Figure 10(A)), a symmetrical and large miscibility gap is predicted over the entire temperature range where TiNiSn is observed to be thermodynamically stable. At 1453K, TiNiSn is experimentally observed to decompose into $TiNi_2Sn$, Ti_2Sn, and Sn [*28*]. The solubility limit of excess Ni in the HH structure is negligible at 300 K and increases to only 1.0% (x = 0.010) at 1450 K. This is in stark contrast to the $ZrNi_{1+x}Sn$ phase diagram where the solubility of Ni is predicted to have a stronger temperature dependence (Figure 10(B)). At 300 K, the solubility is also negligible but steadily increases to 5.8% at 1450K. The solubility continues to increase to 11.0% at 1700 K (ZrNiSn melts at 1760 K). For the $HfNi_{1+x}Sn$ phase diagram (Figure 10(C)), the solubility limit once again is negligible at 300 K,

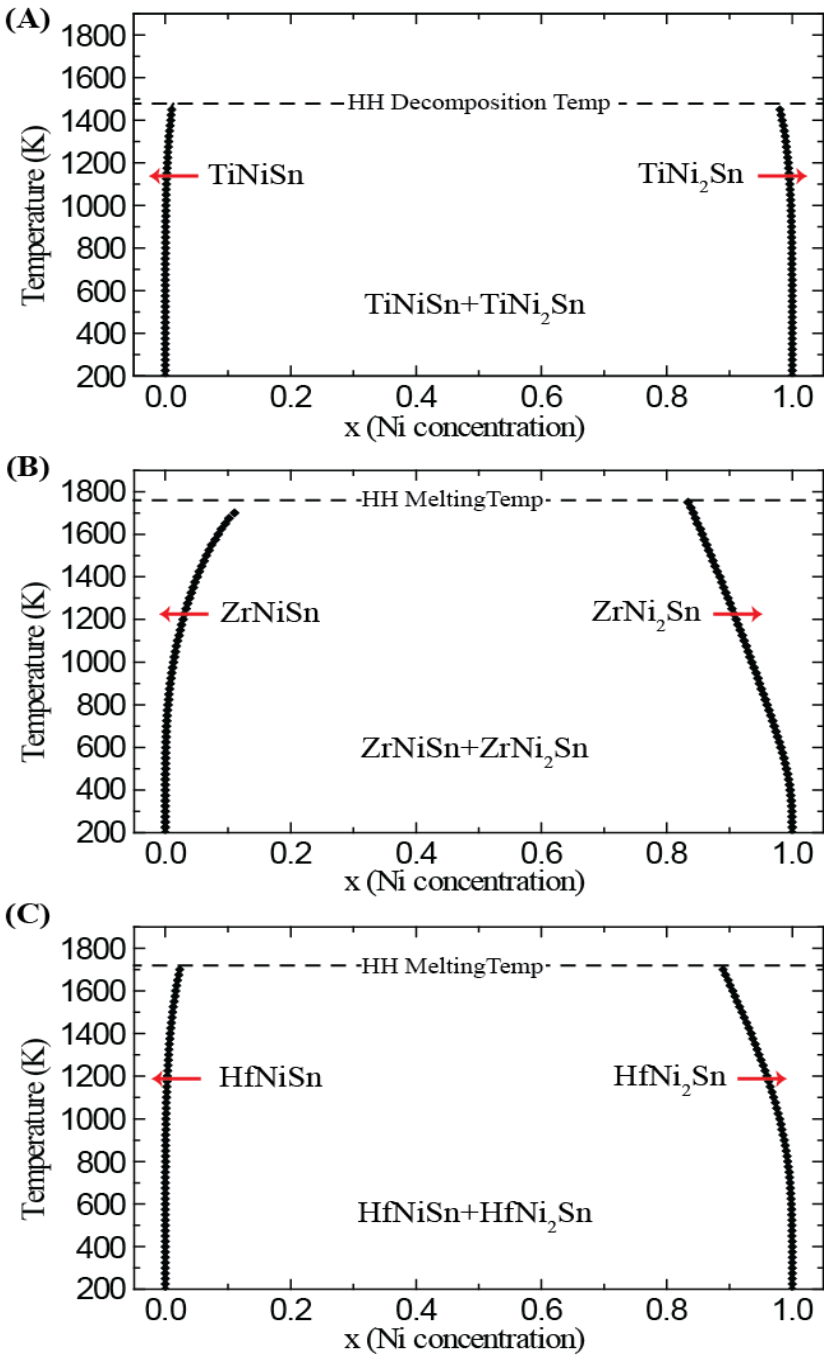

Figure 10. Temperature-concentration pseudo-binary phase diagrams of $TiNi_{1+x}Sn$ (A), $ZrNi_{1+x}Sn$ (B), $HfNi_{1+x}Sn$ (C). The small black diamonds represent calculated points along the phase boundary and the horizontal dashed line indicates experimental melting points for the HH (or decomposition point for TiNiSn).

increases to 1.0% at 1450 K and becomes 2.3% at 1700 K. These low solubility values are in agreement with current experiments where FH secondary phases have been observed with as little as 3% excess Ni with transmission electron microscopy [*34*]. The phase boundaries at higher temperatures and at compositions closer to $x = 0.5$ are not accessible using Monte Carlo simulations, however the present results cover the temperature range for practical operation as TE power generation materials.

Our study suggests that a secondary FH phase will precipitate within a HH matrix at excess Ni concentrations greater than x = 0.01 for temperatures up to 1450 K in TiNiSn and HfNiSn, and up to 900 K in ZrNiSn. If precipitation occurs at the nano-scale, the FH phase may be difficult to observe experimentally by X-ray diffraction (XRD) techniques for concentrations below 3% [*33*]. However, the authors of Ref. [*33*] argue that the measured HH bulk lattice parameter remains constant for all compositions with $x < 3\%$, suggesting two-phase coexistence, in agreement with our predictions.

The temperature dependence of the ZrNiSn phase has a larger Ni solid solubility at high temperatures, however; many studies of TE HH materials find *ZT* to peak between 600 and 800 K [*5, 34, 92*]. The Zr phase shows only 0.4% solubility at 800 K, implying that FH precipitates are predicted to be stable during high temperature operation in the temperature range of interest.

The solubility of vacancies in the FH phase is seen to be much larger than the solubility of Ni in the HH. This is especially true for the $ZrNi_{1+x}Sn$ and $HfNi_{1+x}Sn$ phase diagrams. All three systems begin with negligible vacancy solubility at 300 K. The $ZrNi_{1+x}Sn$ system shows vacancy solubility of 12% ($x = 0.88$) at 1450 K and 16% ($x = 0.84$) at 1700 K. The $HfNi_{1+x}Sn$ system shows vacancy solubility of 7.3% at 1450 K and 11.0% at 1700 K. The $TiNi_{1+x}Sn$ diagram shows an increase to only 2.0% ($x = 0.980$) at 1450 K. The asymmetry between vacancy solubility in FH

and Ni solubility in HH arises from the asymmetry in the formation energies in Figure 9. The higher solubility of vacancies in the FH matrix implies that HH nanostructures within FH materials might be less stable than FH nanostructures in HH materials. However, the low solubility of both Ni and vacancies at room temperature implies that if there is sufficient diffusion, both HH and FH materials are able to from secondary phase nanostructures.

The equilibrium phase diagrams calculated here using the CE model are not the only consideration in determining the actual microstructure observed in materials. In some cases, a material will never realize its thermodynamically stable state because nucleation and diffusion barriers may prevent formation and subsequent growth of the stable phase in a supersaturated matrix. Our current treatment also neglects contributions to the free energy arising from coherency strains during two-phase coexistence. Coherency strains increase the solubility limits of calculated miscibility gaps from the additional interface energy required to make a two phase mixture [*93-96*]. The lattice mismatch between HH-FH ranges between 2.5% to 3%, which can result in sizable strain energy penalties during coherent two-phase coexistence, depending on the elastic moduli of the coexisting phases. Strain energies are also very sensitive to the morphology and distribution of coherent precipitates within a matrix [*97*].

5.4 Vibrational properties of *M*NiSn and *M*Ni_2Sn compounds

5.4.1 Half-Heusler vibrational properties

Phonon dispersion curves along high symmetry directions for TiNiSn, ZrNiSn, and HfNiSn structures are shown in Figure 11. For the semiconducting HH materials a non-analytic correction was used to account for the dipole-dipole interactions, resulting in the splitting of longitudinal

optical (LO) and transverse optical (TO) bands at the zone-center. Several trends can be identified in the HH phonon spectra as the *M*-site atom is changed from Ti to Zr to Hf. Most noticeably, the wide acoustic-optical band gap, which exists in TiNiSn (Figure 11(A)) near 175cm^{-1}, is closed in ZrNiSn (Figure 11B) as the lower optical modes drop in frequency. Large gaps between the optical and acoustic modes reduce acoustic-optical phonon-phonon scattering [*98*] and are undesirable for low thermal conductivity materials. The qualitative similarity in shape of the TiNiSn and ZrNiSn bands shows that the bonding structure is similar, and thus the mass difference between Ti and Zr atoms is the primary cause of the frequency shift.

In HfNiSn the acoustic and optical bands drop lower in frequency than in ZrNiSn and greater optical-acoustic band mixing is seen. All three acoustic branches of HfNiSn have comparably lower Γ point group velocities than TiNiSn or ZrNiSn, as shown in Table 2. Also, a new gap centered around 200 cm^{-1} is opened between the two sets of optical modes. This suggests it is possible to tune the location of the lower optical bands by isoelectronic substitution on the M site. Phonon-phonon scattering mechanisms become more important at high temperatures and thus are of interest in the search for strategies to lower lattice thermal conductivity in HH alloys. All

	Θ_D (K)		υ_g (cm x 10^5 s^{-1})	
	Calculated	Exp	LA	TA
TiNiSn	370	335[a],407[b]	5.9	2.8
ZrNiSn	372	323[b]	5.7	2.9
HfNiSn	320	307[b]	5.1	1.8
$ZrNi_2Sn$	247		4.7	2.7
$HfNi_2Sn$	266		4.2	2.5

Table 2 The Debye temperature, Θ_D, was calculated from the phonon density of states and is compared to experimental results from Ref. [*99*] (a) and Ref. [*100*] (b). Group velocities, υ_g, at the zone center were fit to calculated phonon frequency data along the Γ-X direction.

calculated HH phonon dispersions agree well with past theoretical studies that relied on different computational methods [*101-104*].

5.4.2 Full-Heusler vibrational properties

The calculated dispersion curves for the FH structures, shown in Figure 12, have 3 additional optical bands arising from the 2nd Ni atom in the primitive cell, making a total of 12 phonon bands. The dispersion curves for $TiNi_2Sn$ show imaginary frequencies (Figure 12(A)). Imaginary phonon frequencies (shown as negative frequencies) indicate dynamical instabilities within the cubic phase at zero Kelvin. This surprising result was checked by calculating force constants with larger supercells of size $3 \times 3 \times 3$, which confirmed the existence of the imaginary modes.

While other magnetic and non-magnetic full-Heusler variants of interest for magnetic shape memory applications [*86-88*] have been found to exhibit dynamical instabilities, the particular instabilities that are predicted for $TiNi_2Sn$ have not been previously reported. The $TiNi_2Sn$ phonon dispersions presented here differ from results from a previous computational study by Hermet *et al.* [*104*]. Hermet's work uses the Local Density Approximation (LDA), and observed no imaginary frequencies. The origins of the instability observed in this work will be further discussed later in section 5.5.

In contrast to $TiNi_2Sn$, the $ZrNi_2Sn$ and $HfNi_2Sn$ phonon spectra have no unstable phonon modes, although both exhibit very low frequency acoustic modes at the X point. The $ZrNi_2Sn$ and $HfNi_2Sn$ dispersion curves show significant mixing between acoustic and optical modes. The lower optical modes appear to push down the acoustic modes dropping the group velocities below that of HfNiSn, as seen in Table 2.

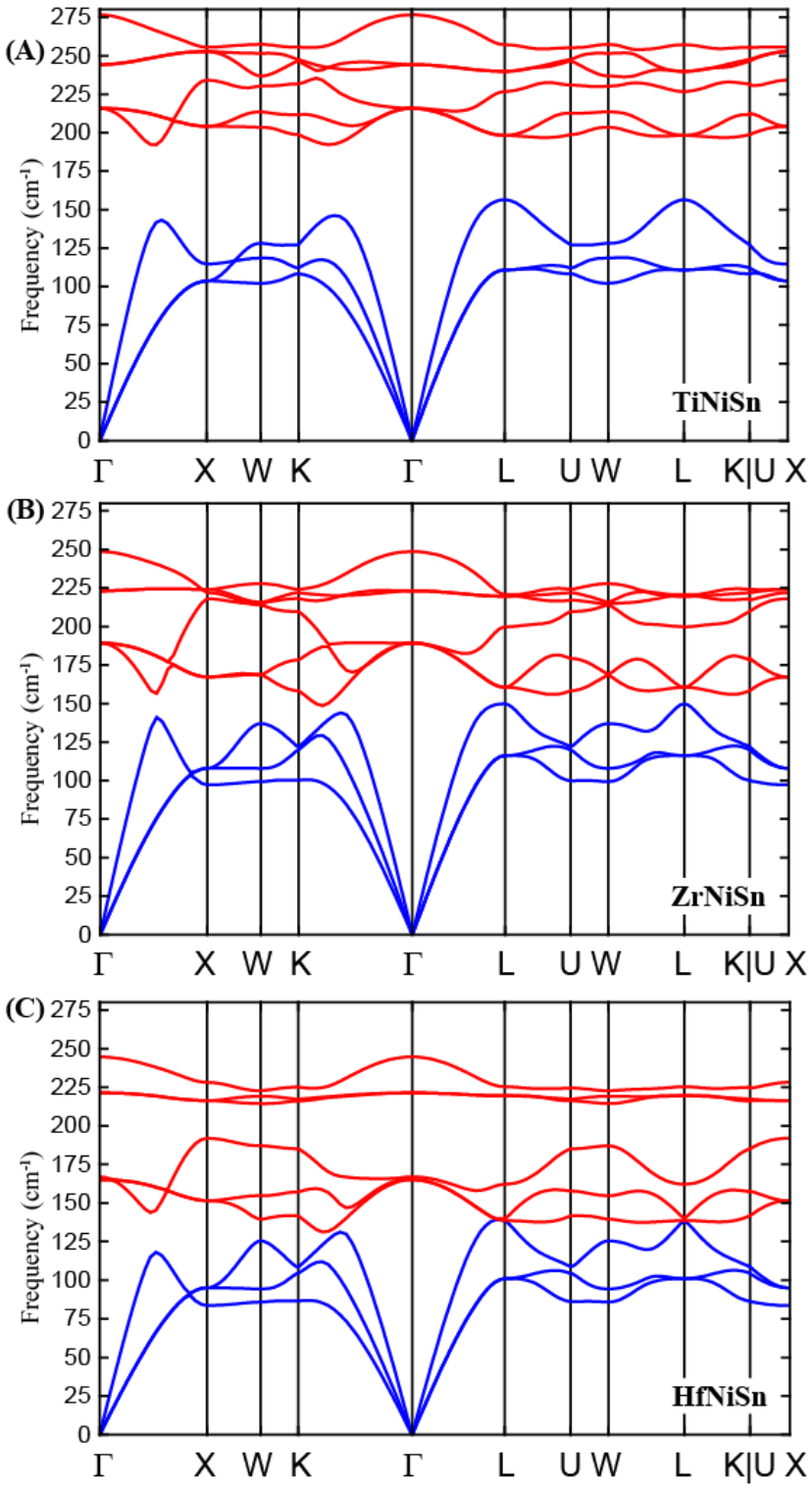

Figure 11. Phonon dispersion curves of TiNiSn (A), ZrNiSn (B), and HfNiSn (C) calculated with DFT shown along high symmetry paths. Optical bands are shown in red and acoustic in blue.

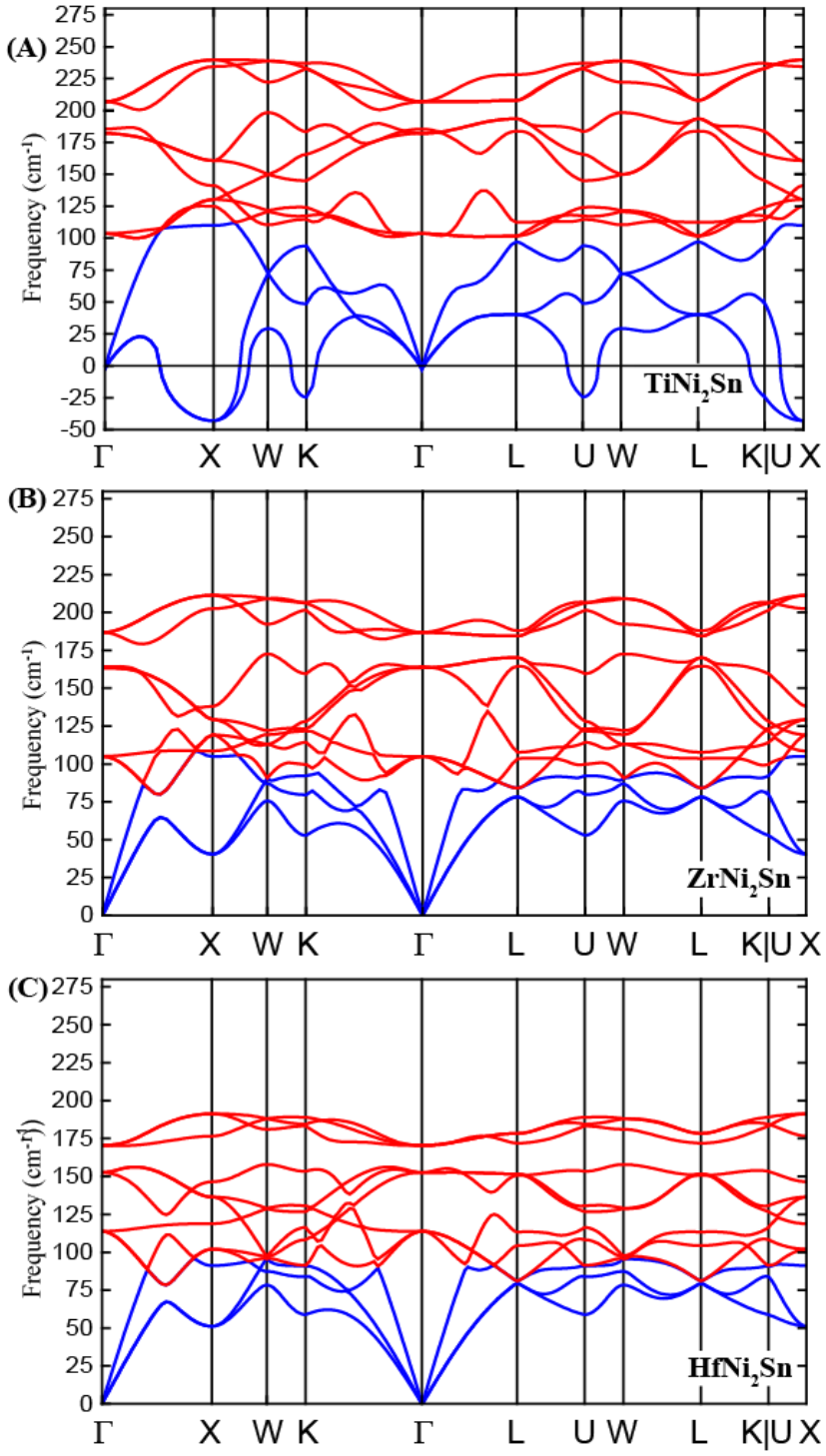

Figure 12. Phonon dispersion curves of $TiNi_2Sn$ (A), $ZrNi_2Sn$ (B), and $HfNi_2Sn$ (C) calculated with DFT shown along high symmetry paths. Optical bands are shown in red and acoustic in blue. Imaginary frequencies are shown as negative values.

5.4.3 Phonon density of states and thermal properties

The total phonon density of states (DOS) and partial phonon density of states (PDOS) are shown in Figure 13. The PDOS is a measure of the relative contributions of each atom in the eigenvector of motion associated with each phonon mode. The FH structures (Figure 13(D-F)) are seen to have very mixed states with approximately equal contributions from each atom for the acoustic and first optical bands. The $TiNi_2Sn$ structure has a significant DOS at frequencies below 50 cm^{-1} from the low frequency TA mode contributions, which arise from the instability. The HH compounds (Figure 13(A-C)) have modes where the PDOS is dominated by contributions from a single atom type. The trends in the HH DOS reflect those seen in their phonon dispersion curves; the peaks shift to lower frequencies as the mass of the M-site atom increases. The acoustic modes are predominantly formed by the heaviest atom in the basis, which is Sn in TiNiSn and ZrNiSn. However, the mass of Hf atoms is larger than that of Sn and the HfNiSn acoustic modes are dominated by the Hf atom contributions as a result.

The acoustic modes dominate heat transport of materials at low and intermediate temperatures because of their high group velocities compared to the optical modes. The shift of dominance from the Sn atom to the Hf atom in the acoustic PDOS implies that M-site alloying would have a greater effect on k_L in HfNiSn than in TiNiSn, as previously observed by Hermet *et al.* [*104*]. Previous experimental studies have wide variance in their synthesis techniques, and the resultant microstructure of their materials makes it difficult to confirm the alloying effects on k_L with our predictions. The optical modes are primarily composed of *M*-atoms and Ni in TiNiSn and ZrNiSn, and switch to Ni and Sn for the HfNiSn structure. The Debye temperature was calculated by fitting the total DOS from zero to one quarter of the maximum phonon frequency. The results follow the trend of a decreasing Debye temperature when going from lighter (Ti) to heavier (Hf)

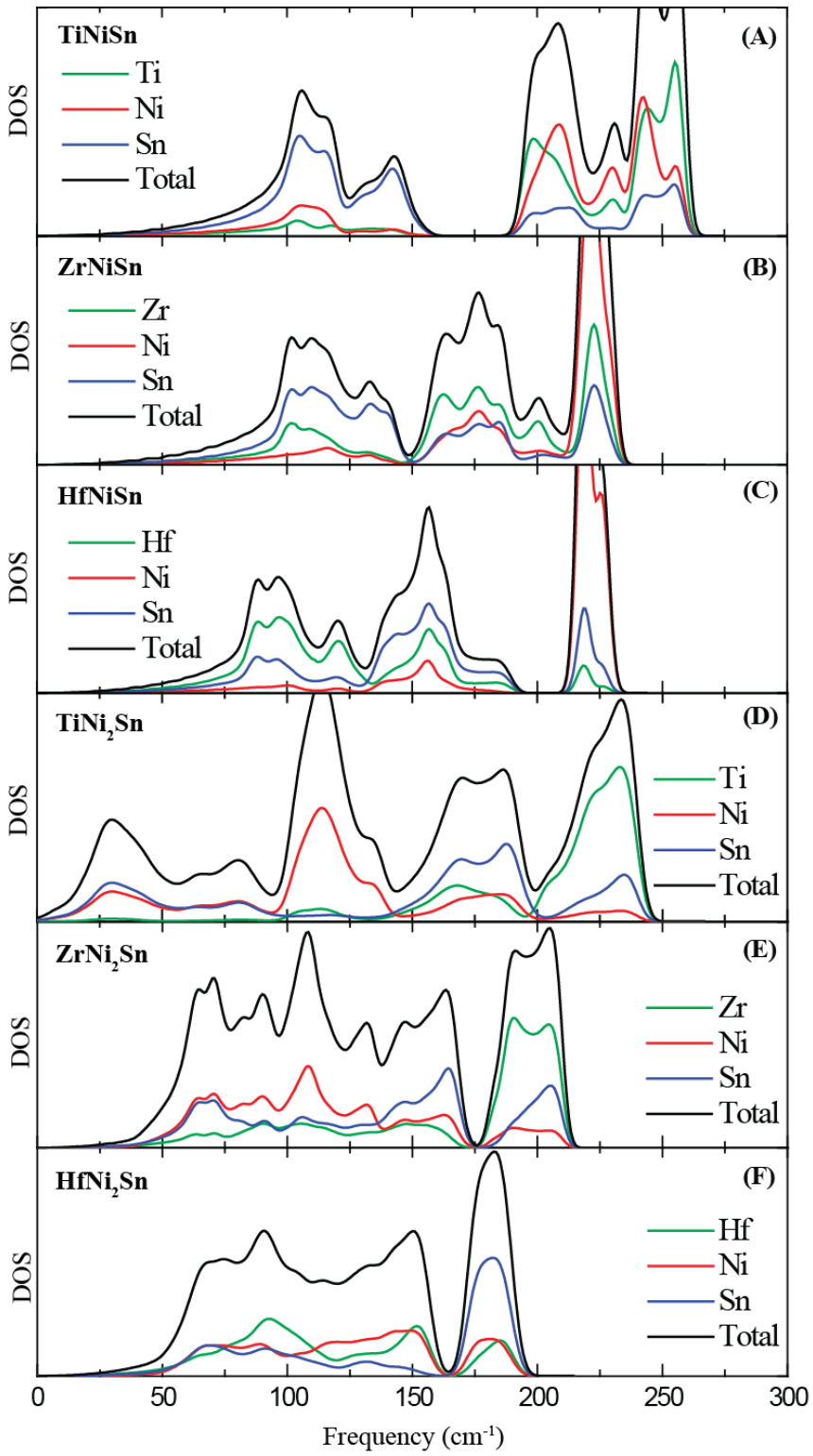

Figure 13. Total density of states (DOS) and partial density of states (PDOS) calculated with DFT. Total DOS is shown in black and contributions from each atom are shown in color, green for *M* = Ti, Zr, or Hf, red for Ni and blue for Sn. Parts (A) through (F) show the DOS for TiNiSn, ZrNiSn, HfNiSn, $TiNi_2Sn$, $ZrNi_2Sn$, $HfNi_2Sn$, respectively.

transition metal. This trend is consistent with a similar increase in phonon DOS at low frequencies with increasing transition metal mass. The calculated Debye temperature match reasonably well with experiment [*99, 100*], as shown in Table 2.

The phonon contributions to heat capacity at constant volume, $C_{v,}$ were calculated within the Phonopy code and are shown in Figure 14 from temperatures 0 to 1000K. The specific heat at constant volume in Figure 14, c_v, is normalized by the number of atoms. The computed c_v of TiNiSn agrees well with experimental measurements [*99*]. Unfortunately, no experimental data is available for comparison with the other HH and FH materials. The per-atom heat capacities at 100 K are given as: c_v = 13.9, 15.4, 16.4, 16.7 18.46, 18.93 ($kJ.K^{-1}.mol^{-1}$) for TiNiSn, ZrNiSn, HfNiSn, $TiNi_2Sn$, $ZrNi_2Sn$, and $HfNi_2Sn$, respectively. This trend can be explained by the shifting of the vibrational DOS to lower frequencies, which increases the number of modes available at low temperatures. $TiNi_2Sn$ is the exception. The low frequency modes associated with the X-TA

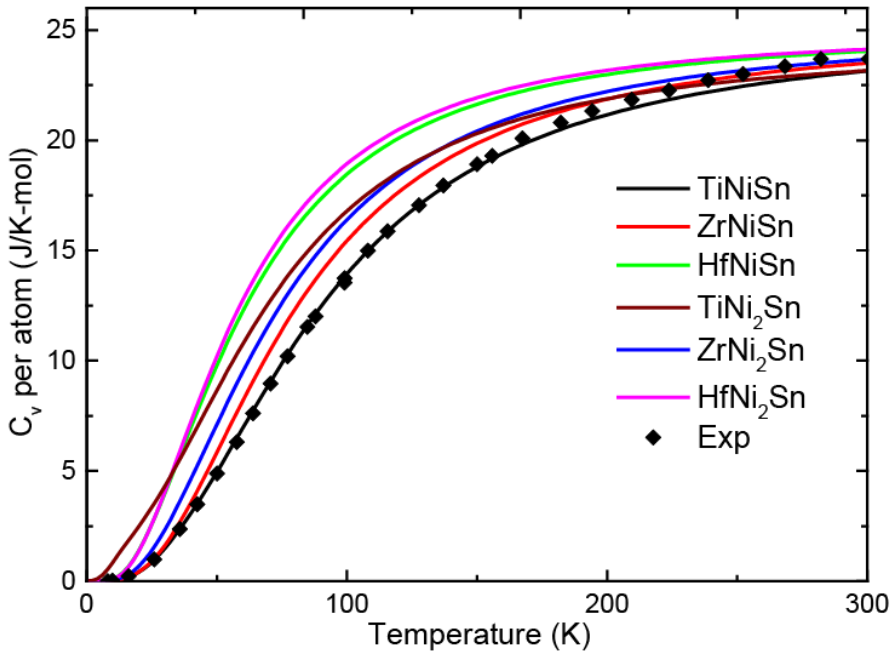

Figure 14. Heat capacity per atom is calculated using DFT. TiNiSn results are compared to experimental data of B. Zhong (ref. 92)

instability create a large DOS at frequencies below 50 cm^{-1} making the c_v of $TiNi_2Sn$ larger than the other structures up to 32 Kelvin. Imaginary modes were not included in the calculation of c_v. In the case of HH, increasing the mass of the M-site atom causes the DOS shift to lower frequencies, and in FH structures the addition of the 2^{nd} Ni atom introduces a new optical band that pushes the acoustic bands frequencies lower. As the temperature increases past the Debye temperature, all phonon modes become occupied and the calculated specific heat of all the HH and FH approach the classical Dulong-Petit limit of 24.94 within ±0.04 ($J.mol^{-1}K^{-1}atom^{-1}$) at 2000K.

5.5 $TiNi_2Sn$ instabilitiy

5.5.1 Energies of distorted cells

The imaginary phonon frequencies of cubic $TiNi_2Sn$ are a result of the negative curvature of the Born-Oppenheimer energy surface with respect to a particular collective atomic displacement. The cubic $TiNi_2Sn$ crystal structure can therefore further decrease its energy by distorting along the eigenvectors of an unstable phonon mode. The distorted structures lower the total formation energy and often have a lower symmetry. Many phases that are predicted to be dynamically unstable at zero Kelvin with DFT are, indeed, experimentally observed at high temperatures where they are stabilized by anharmonic vibrational excitations [*105-108*]. The predicted phonon dispersion curves for $TiNi_2Sn$ show unstable modes near the Brillouin zone edge at the X, K, and U points. At the X point, the phonon wave travels along the cubic [001] direction with a wavelength equal to the conventional cubic unit cell. The unstable modes at the X point correspond to two-fold degenerate transverse acoustic (TA) modes, which we denote as X-TA modes. The unstable modes at the K and U-points each are singly degenerate longitudinal acoustic (LA) modes.

We can further explore the nature of the dynamical instabilities of cubic $TiNi_2Sn$ by directly calculating the energy of the crystal as a function of the amplitude of the unstable phonon modes. While common Bain paths, such as tetragonal and rhombohedral distortions, revealed no reduction in the energy of cubic $TiNi_2Sn$, lower energy structures can be found when the atoms are internally shuffled according to the X-point TA mode eigenvectors. The atomic displacements of this phonon mode are shown in Figure 15, with displacements magnified by 20 times for clarity. The energies of $M Ni_2Sn$ (M=Ti, Zr, Hf) as a function of the amplitude of an X-TA phonon mode are shown in Figure 16A. Since the X-TA phonon mode is dominated by Ni displacements, the displacement distance of Ni atoms is used as a metric of the phonon mode amplitude (horizontal axis in Figure 16A). As is clear in Figure 16A, the cubic form of $TiNi_2Sn$ can further lower its energy by 1.1 meV per formula unit (f.u.). Cubic $ZrNi_2Sn$ and $HfNi_2Sn$, in contrast, are

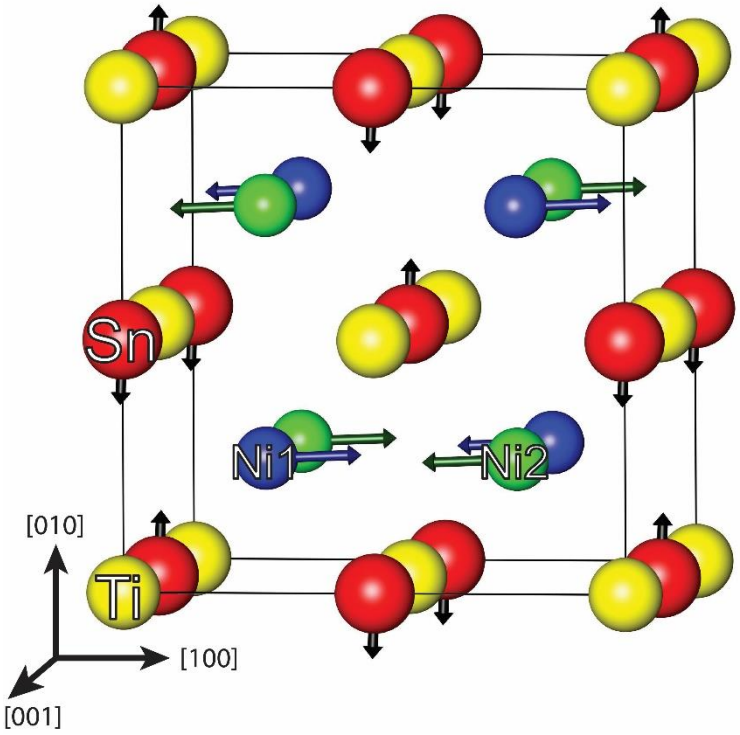

Figure 15. Atomic motions of the X-point TA phonon mode are shown for each atom of the $TiNi_2Sn$ structure. The phonon mode travels in the cubic [001], out of the page. Black arrows indicate atomic motion with amplitudes magnified by 20x.

dynamically stable for the same X-TA phonon modes (Figure 16(A)). Isoelectronic substitution of *M*-site atoms has little effect on the chemistry of the bonding but there are significant differences in the atomic radii of the Ti, Zr, and Hf atoms and, correspondingly, there are large differences in the lattice parameter, as shown in Table 1. The energy of $TiNi_2Sn$ along the phonon modes having

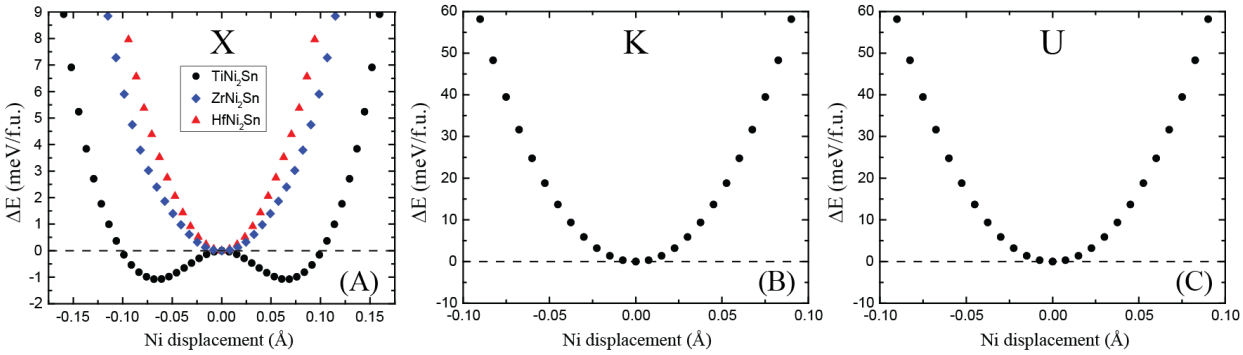

Figure 16. Energy per formula unit of 2x2x2 supercells is shown as a function of phonon mode displacement amplitude for (A) X-point, (B) K-point, and (C) U-point modes for $TiNi_2Sn$. $ZrNi_2Sn$ and $HfNi_2Sn$ energies are shown in (A) for comparison and have positive curvature along the distortion path, whereas $TiNi_2Sn$ has negative curvature with energies that drop 1.1 meV below that of cubic $TiNi_2Sn$. K and U points show no instabilities along their paths. The horizontal axis measures the displacement of Ni atoms from their equilibrium position.

.

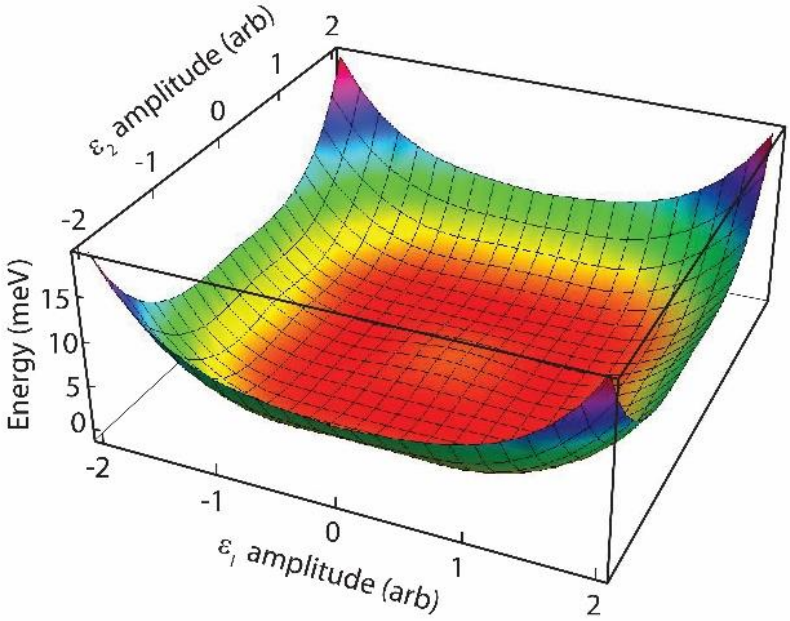

Figure 17. Contour plot shows the change in formation energy of $TiNi_2Sn$ structure as a function of X-TA phonon mode amplitudes ε_1 and ε_2.

imaginary frequencies at the K and U points increase with amplitude (Figure 16(B and C)). Hence, the DFT parameterized harmonic phonon Hamiltonian used to calculate phonon dispersion curves for $TiNi_2Sn$ predicts spurious dynamical instabilities at the K and U points.

The X point is on the Brillouin zone edge in the symmetrically equivalent cubic [001], [010], and [100] directions. Each direction has 2 orthogonal transverse acoustic modes that we call ε_1 and ε_2. The full energy landscape of the X-TA subspace can be characterized by combinations of these two modes with varying amplitudes. Figure 17 shows the change in energy (relative to cubic $TiNi_2Sn$) as a function of ε_1 and ε_2 amplitudes. The plot shows that lower energy distortions exist for any displacements due to a combination of both X-TA ε_1 and ε_2 phonon modes, however, the minimum energies are found along the symmetrically equivalent $(\varepsilon_1,0)$ and $(0,\varepsilon_2)$ directions.

The minimum energy structures have reduced symmetry, from cubic $TiNi_2Sn$ to monoclinic. The distorted structure has space group $P2_1/m$ (space group #11). We did not explore whether additional symmetry breaking could reduce the energy of $TiNi_2Sn$ any further.

The energy curve in Figure 16(A) shows not only that $TiNi_2Sn$ is dynamically unstable at zero Kelvin, but that anharmonic vibrational excitations at elevated temperature should, at some transition temperature, result in the stabilization of the high temperature cubic form of $TiNi_2Sn$ [*107*]. However, the shallow depth of the energy well at only 1.1 meV/f.u. suggests that the critical temperature of stabilization will be very low, if observable at all. A treatment accounting for anharmonic vibrational excitations would be necessary to predict the true critical temperature. While little is understood about high temperature phases that become dynamically unstable at low temperature, the anharmonic excitations that are crucial in making these phases stable above a critical temperature should also have a significant impact on their thermal conductivity.

5.5.2 Origins of $TiNi_2Sn$ instability

To better understand why $ZrNi_2Sn$ and $HfNi_2Sn$ full-Heusler structures are dynamically stable and $TiNi_2Sn$ is not, we explored the effects of interatomic spacing on the $TiNi_2Sn$ instability. As expected, increasing or decreasing the lattice parameter, and subsequently the total volume of the cubic FH crystal structure, results in an overall increase in the formation energy. However, the formation energy's trend as a function of X-TA phonon mode amplitude changes dramatically with lattice parameter. Figure 19 shows the energy of distorted $TiNi_2Sn$ supercells with varying lattice parameter, a. It is found that increasing the lattice parameter makes the structure less stable by lowering the energy of the distorted structures relative to the cubic form. Decreasing the lattice parameter to $a = 0.98a_0$ results in all distorted structures having a higher energy than the cubic structure. The transition from negative to positive curvature occurs near $a = 0.99a_0 = 6.054$ Å. The positive energy curvature at these smaller lattice parameters implies that smaller inter atomic distances stabilize the cubic structure with respect to the X-TA displacements.

The results of Ref. [*104*], which found no complex modes in $TiNi_2Sn$ dispersions, can be explained by the tendency for the X-TA instability to stabilize for smaller lattice parameters. Hermet and coworkers use LDA functionals, which tend to underestimate lattice parameters. Their LDA lattice parameter of $a = 5.91$ Å underestimates the experimental value by 3%, which would remove all traces of the instability according to our results. In our work, GGA functionals overestimate the lattice parameter and exceed the experimental value by 0.5%. While the GGA calculations achieve better agreement with experiment in this case, on average, GGA can overestimate the lattice parameter by about 1% [*47*]. Given the sensitivity of the energy surface on the lattice parameter, the results presented here can only claim that the $TiNi_2Sn$ structure is unstable according to GGA calculations.

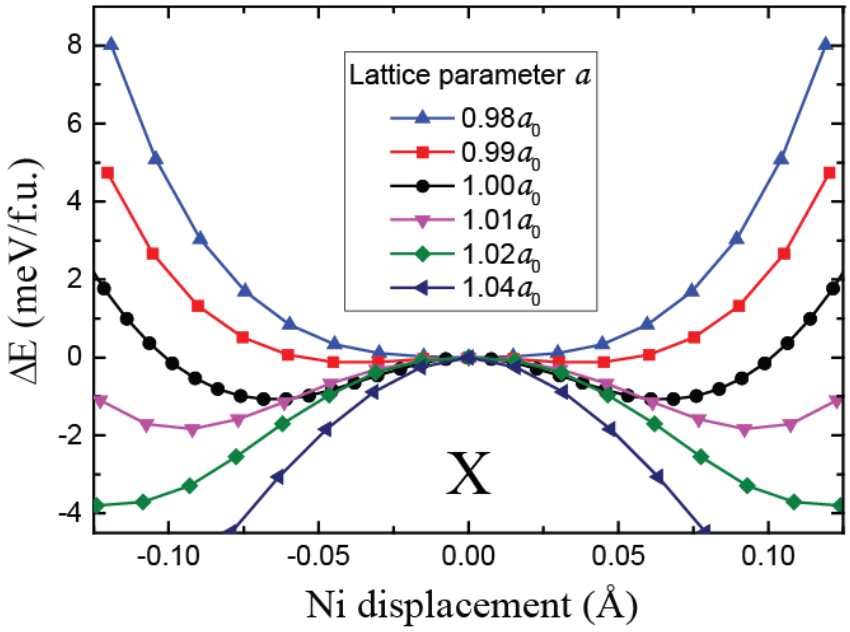

Figure 19. Formation energies of TA-X mode distorted $TiNi_2Sn$ structures relative to the FCC structure are shown for cells of varying lattice parameter *a*, where $a = d*a_0$, and d = 0.98, 0.99, 1.00, 1.01, 1.02, 1.04 and a_0 = 6.116 Å

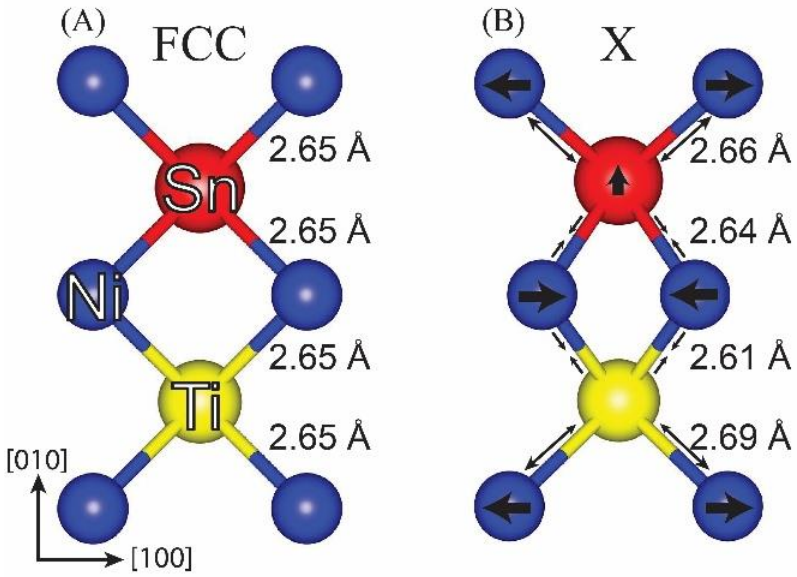

Figure 19. Schematic of the FCC structure (A) and the X-TA mode displaced structure (B), viewed along the cubic [001] direction. The distance between atoms is shown next to each bond. Black arrows centered on atoms show the direction of their displacement relative to the FCC structure.

The instabilities seen in other Heusler alloys were also found to be in TA vibrational modes dominated by the motion of Ni atoms, however the same explanations of optical-acoustic mode mixing cannot be applied to $TiNi_2Sn$ [*86, 88*]. The ordering of the optical bands in MNi_2Sn structures does not change between $TiNi_2Sn$ and $ZrNi_2Sn$ or $HfNi_2Sn$. Furthermore, the Fermi level is not located at a local maximum of the electronic density of states (eDOS) and little to no change in the eDOS is seen near the Fermi level for the distorted structures. Thus, the instability cannot be explained by the Jahn-Teller effect either [*109*]. It is unclear if the Fermi-surface nesting proposed for $MnNi_2Ga$ can be applied to $TiNi_2Sn$ [*88*]. One possible explanation for the instability in $TiNi_2Sn$ is a simple rearrangement of atoms to achieve energetically favorable interatomic bonding distances.

We now examine the effects of X-TA mode distortions on the interatomic distances. In the cubic full-Heusler structure, each Ti (or Sn) site is at the center of a cube made up of 8 Ni atoms. The Ti-Ni and Sn-Ni interatomic distances are equal for all 8 Ni atoms, as shown in Figure 19(A), where only the top layer of Ni atoms are shown in blue for clarity. To a close approximation, the X-TA distortion moves Ni atoms only in the [100] directions indicated in Figure 19(B). Four of the eight Ni atoms slide closer to Ti and shorten the Ti-Ni bond by 0.04 Å. The other 4 move away and lengthen their bond by 0.04 Å. Sn atoms also move in the X-TA distortion. Sn atoms move away from the oncoming Ni atoms by shifting in the [010] direction. The result is that 4 Ni-Sn bonds are only shortened by 0.01 Å and the other 4 only lengthened by 0.01 Å. The overall effects result in Ti atoms being closer to 4 of the 8 Ni atoms while the Ni-Sn bond lengths are more or less unchanged.

Strong p-d hybridization seen in other full-Heusler structures [*86, 110*] may be present in the Ni-Sn bonding and result in more rigid bonds. Rigid Ni-Sn bonds might force the structure to

have a larger lattice parameter, leaving the Ti atoms unable to fill the voids. The X-TA distortion path avoids the energy penalty of altering the Ni-Sn bond lengths while moving the Ti atoms into more stable bonds with 4 of the 8 Ni, possibly resulting in the lower formation energies relative to the cubic structure.

5.6 Conclusions

A thorough analysis of equilibrium phases as a function of temperature and Ni concentration was performed using DFT energies combined with a cluster expansion and Monte Carlo simulations on the HH-FH systems. The calculated phase diagrams predict a miscibility gap between HH-*M*NiSn and FH-*M*Ni_2Sn (M = Ti, Zr, or Hf), with limited Ni solubility in the HH and a limited tolerance for Ni vacancies in FH. The calculated phase diagrams suggest that FH nano-precipitates seen in experiments are thermodynamically stable at concentrations of 1% below the temperature of 1400 K in $TiNi_{1+x}Sn$ and $HfNi_{1+x}Sn$ and below 800 K in the $ZrNi_{1+x}Sn$. Higher solubility of vacancies in FH compositions implies that a larger supersaturation is necessary to form a HH second phase inside FH bulk at elevated temperatures.

Phonon spectra and thermodynamic properties were examined using DFT. The phonon band structures of the HH materials show that the selection of the M atom changes the frequency of optical bands and determines which atom dominates the PDOS of acoustic modes. Calculated heat capacity data agrees well with experiment for TiNiSn and other *M*NiSn and MNi_2Sn phases show trends that follow from the shifts in DOS frequency with M-site mass.

The $TiNi_2Sn$ structure was predicted to be dynamically unstable at zero Kelvin. It is possible to lower the energy compared to cubic FH by displacing atoms along the X-TA mode

distortion path. The nature of the instability is found to be different from instabilities found in other Heusler compounds. The volume dependent distortion energies show that smaller lattice parameters remove the instability along the X-TA mode, indicating that interatomic distances are crucial in creating the instability. We propose that the instability could originate from the smaller size of the Ti 3d orbitals compared to Zr 4d and Hf 5d orbitals.

Chapter 6 Origins of Phase Separation in Thermoelectric (Ti,Zr,Hf)NiSn half-Heusler Alloys from First Principles

6.1 Introduction

While there are many promising half-Heusler compounds for TE power generation, it is widely believed that the *M*NiSn and *M*CoSb (M = Ti, Zr, or Hf) compounds have the most potential for industrial use. These compounds are the most stable and exhibit some of the highest *ZT* values. The state of the art *M*NiSn and *M*CoSb compounds have been shown to achieve *ZT* greater than 1 by use of isoelectronic alloying between all three Ti, Zr, and Hf elements. In 2005, Sakurada and Shutoh observed a high *ZT* of 1.5 at a temperature of 700 K for the $(Hf_{0.25}Zr_{0.25}Ti_{0.5})NiSn_{0.998}Sb_{0.002}$ compound [*6*]. For several years, this result could not be reproduced, and it was not well understood why the *ZT* was so much higher than other similar compounds. More recently, high *ZT* was again achieved in the n-type $(Hf_{0.25}Zr_{0.25}Ti_{0.5})NiSn_{0.998}Sb_{0.002}$ [*92*], with a value of 1.2 at 830 K. Furthermore, a *ZT* of 1.2 was also found in the p-type $(Hf_{0.75}Ti_{0.25})CoSb_{0.85}Sn_{0.15}$ at 983 K [*111*]. The improvements in the figure of merit in both n-type and p-type HH alloys have been attributed to the coexistence of multiple HH phases with different compositions. The phase separation has been reported to occur on a length scale of micrometers [*92, 111-118*]. The observed phases have mixtures of Ti, Zr, and Hf, which results in mass defect scattering and, additionally, the microscale grain boundaries enhance the scattering of long wavelength phonons, thereby significantly

reducing the lattice thermal conductivity of the material. The separate HH phases have coherent or semi-coherent grain boundaries and thus do not harm the electronic properties of the material, resulting in an overall high *ZT*.

The observed microstructures and solubility limits of the $(Hf_{1-x-y}Zr_xTi_y)NiSn$ HH phases are highly dependent on synthesis techniques. When samples are synthesized by arc melting, the material forms a multi-phase mixture, with two dominating phases. One phase is Ti-rich, with smaller amounts of Zr and Hf, while the other phase has a high concentration of Zr and Hf while being deficient in Ti [*92, 111-116*]. In the work of Populoh *et al.* [*112*], for example, samples of $(Hf_{0.26}Zr_{0.37}Ti_{0.37})NiSn$ synthesized by arc melting followed by annealing, exhibited a two-phase microstructure where the (Zr,Hf)-rich phase appeared to have solidified as dendrites, while the Ti-rich phase, showing signs of having solidified later, filled in the interdendritic regions. Energy dispersive X-ray (EDX) analysis showed that the Ti-rich phase had an average composition of $(Hf_{0.06}Zr_{0.22}Ti_{0.72})NiSn$, while the (Zr,Hf)-rich phase had an average composition of $(Hf_{0.33}Zr_{0.47}Ti_{0.20})NiSn$. The Zr and Hf atoms were found to be uniformly distributed within the (Zr,Hf)-rich grains, implying ZrNiSn and HfNiSn form a solid solution. In other studies, careful X-ray diffraction (XRD) showed that up to five separate half-Heusler phases with distinct lattice constants were present within the material [*92, 111, 113*]. The exact Ti to (Zr, Hf) ratio and degree of ordering on the *M* site of these phases remains unknown.

Very different microstructures are obtained when solid-state reaction synthesis is used [*119, 120*]. The solid-state method avoids cooling from the disordered melt. In a study by Downie *et al.* [*119*], solid-state reaction synthesis was used and the samples were reacted for the same temperature and duration as the annealing step in the Populoh *et al*. study (1173 K for 2 weeks). No dendritic features were observed. Instead, EDX analysis revealed an absence of any significant

variations in the composition of the grains, with the largest variations observed being less than 10 % [*119*]. The XRD pattern of the sample with composition $Zr_{0.5}Ti_{0.5}NiSn$ showed multiple peaks corresponding to a semi-continuous distribution of $Zr_{1-x}Ti_xNiSn$ phases throughout the composition range of $0.24 \leq x \leq 0.70$ [*119*]. Similar results were seen with $Ti_{0.5}Hf_{0.5}NiSn$ having semi-continuous $Ti_{1-x}Hf_xNiSn$ phases with a composition range of $0.32 \leq x \leq 0.61$. Surprisingly, $Zr_{0.5}Hf_{0.5}NiSn$ is also seen to form multiple XRD peaks. The observation of multiple XRD peaks in the binary systems was used to argue that, despite the uniform microstructure, some degree of phase separation must have occurred.

The above mentioned experimental studies suggest that the solubility limits of Ti, Zr, and Hf are heavily dependent on synthesis technique. In this study, we use first principles statistical mechanics methods to predict phase stability and solubility limits of half-Heusler phases in the pseudo-ternary composition space defined by $(Hf_{1-x-y}Zr_xTi_y)NiSn$. By comparing the predicted stable phases to experiment, it is possible to identify whether the observed microstructural features reflect thermodynamic equilibrium or were kinetically trapped during synthesis. Understanding the fundamental mechanism responsible for the formation of Ti-rich and Ti-poor grains is invaluable in guiding future experimental work and optimization efforts aimed at further improving the thermoelectric efficiency of half-Heuslers and other material systems.

In the following, I present the results of a study [*121*] of the energies of formation along the pseudo-binary compositions of $(Hf_{1-x}Ti_x)NiSn$, $(Zr_{1-x}Ti_x)NiSn$, and $(Hf_{1-x}Zr_x)NiSn$. The study is also expanded to the full pseudo-ternary space of $(Hf_{1-x-y}Zr_xTi_y)NiSn$ in order to relate predictions directly to the high efficiency compounds discussed in experiments. First principles configurational formation energies are combined with statistical mechanics methods to predict equilibrium pseudo-ternary phase diagrams at finite temperatures. Finally, the results are compared

with existing experimental evidence and discuss how sluggish atomic diffusion plays an important role in kinetically trapping phase separated *M*NiSn compounds.

6.2 Methods

Calculations used a plane wave energy cutoff of 550 eV and a 9 × 9 × 9 Monkhorst-Pack [*51*] k-point mesh to sample the Brillouin zone. All supercells were allowed to fully relax. The formation energy was then calculated with a static run using the tetrahedron method. Cluster expansions were constructed for the $(Hf_{1-x}Ti_x)NiSn$ and $(Zr_{1-x}Ti_x)NiSn$ pseudo-binaries ($0 \leq x \leq 1$) by fitting the DFT formation energies of over 55 different configurations over the *M* sites within supercells of volumes up to five times that of the primitive cell. The pseudo-ternary $(Hf_{1-x-y}Zr_xTi_y)NiSn$ ($0 \leq (x, y) \leq 1$) cluster expansion was fit to the formation energy of 270 different configurations. The CV scores for each cluster expansion were smaller than 2 meV/site.

6.3 Pseudo-binary *M*NiSn systems

6.3.1 Pseudo-binary formation energies

The formation energies of the enumerated configurations in the $(Zr_{1-x}Ti_x)NiSn$, $(Hf_{1-x}Ti_x)NiSn$, and $(Hf_{1-x}Zr_x)NiSn$ pseudo-binaries for $0 \leq x \leq 1$ are shown in Figure 20(a, b, and c). The formation energies are calculated relative to the pure compounds TiNiSn, ZrNiSn, and HfNiSn. The DFT formation energies are shown as blue diamonds. In the $(Zr_{1-x}Ti_x)NiSn$ and $(Hf_{1-x}Ti_x)NiSn$ systems, the relative formation energies of intermediate configurations (where $0 < x < 1$) are positive, implying that only the pure compounds are stable at zero temperature. In contrast, several intermediate configurations of the $(Hf_{1-x}Zr_x)NiSn$ system, shown in Figure 20c, have small

negative formation energies. At all intermediate compositions calculated, a configuration with negative energy exists. The similarity of the formation energies and the fact that no configuration is drastically more favorable than the others indicates that a disordered solid solution of ($Hf_{1-x}Zr_x$)NiSn should be thermodynamically stable even at low temperatures, in agreement with experiment [*114*]. The calculated formation energies of ($Zr_{1-x}Ti_x$)NiSn and ($Hf_{1-x}Ti_x$)NiSn are relatively small compared to the energy of the Ni-vacancy ordering in the *M*Ni_{1+x}Sn system studied in previous work [*85*].

All three *M*NiSn compounds have similar electronic band structures [*84, 122*], indicating that large changes in bonding do not occur with isoelectronic substitution of Ti, Zr, and Hf. The positive formation energies in ($Zr_{1-x}Ti_x$)NiSn and ($Hf_{1-x}Ti_x$)NiSn, are therefore likely a result of the elastic strain energy penalty that arises when the smaller TiNiSn structure and the larger (Zr,Hf)NiSn structures are forced to mix. The DFT-GGA lattice parameters for *M*NiSn compounds are shown in Table 1. The lattice mismatch between TiNiSn and ZrNiSn compounds is 3.4 %, and similarly between TiNiSn and HfNiSn the mismatch is 2.7%. In contrast, the lattice mismatch between HfNiSn and ZrNiSn is only 0.7%. All DFT-GGA values are in close agreement with experiment [*89*]. The formation energies of ($Zr_{1-x}Ti_x$)NiSn are overall higher than those of ($Hf_{1-x}Ti_x$)NiSn. This correlates well with the larger lattice constant mismatch between ZrNiSn and TiNiSn compared to that between HfNiSn and TiNiSn. A more thorough study of the elastic strain energy is required to quantitatively determine if strain energy is the dominating factor in the configurational formation energies calculated here.

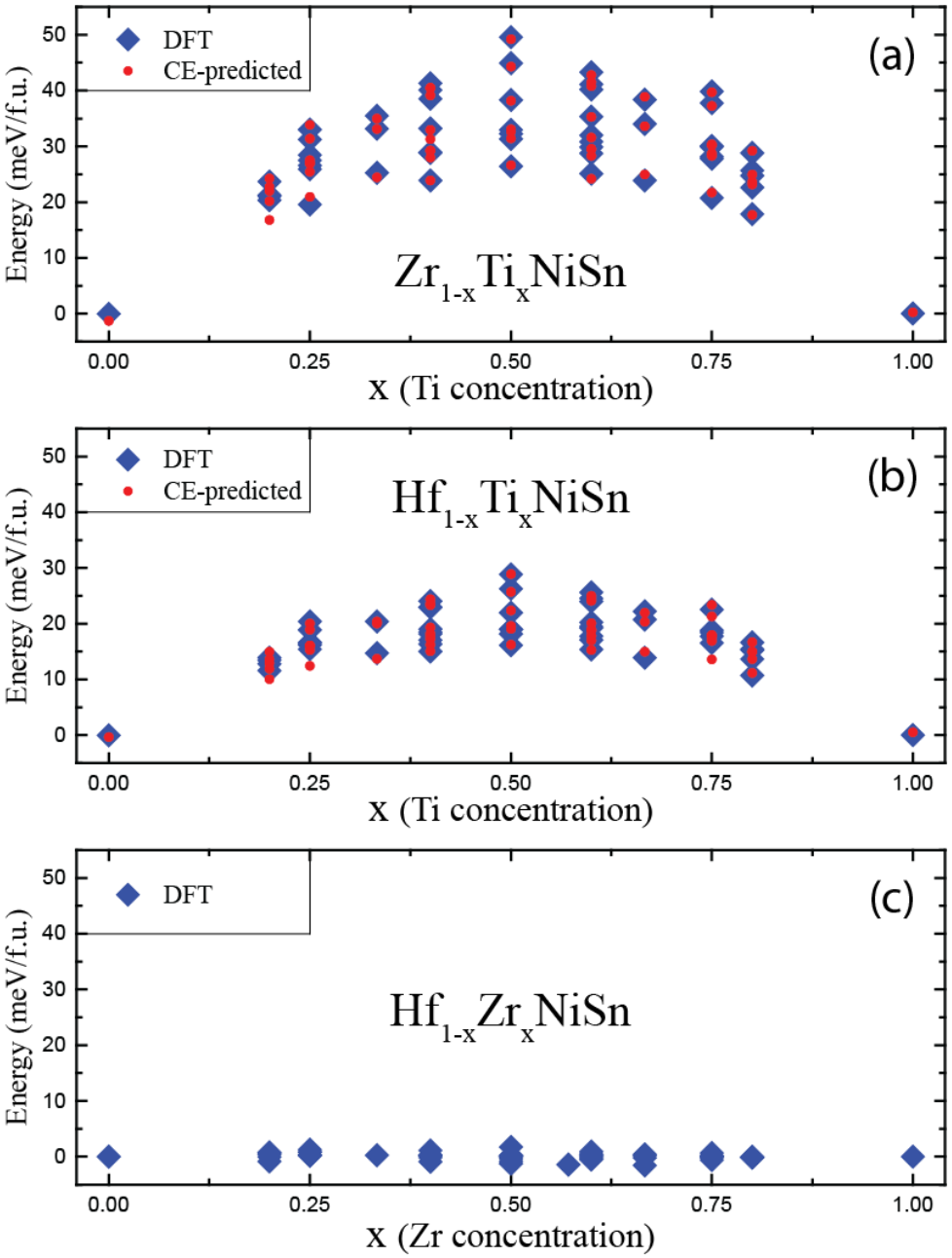

Figure 20. Formation energy per formula unit relative to the pure end states for $Zr_{1-x}Ti_xNiSn$ (a), $Hf_{1-x}Ti_xNiSn$ (b), and $Hf_{1-x}Zr_xNiSn$ (c). The configurational energies calculated by DFT are shown as blue diamonds, and CE predicted energies are shown as red dots.

6.3.2 Pseudo-binary phase diagrams

Configurational energies of the pseudo-binary systems $Zr_{1-x}Ti_xNiSn$ and $Hf_{1-x}Ti_xNiSn$ were used in separate cluster expansion fits in order to obtain accurate phase boundaries. Figure 20 shows the formation energies predicted by the cluster expansions (red dots). The CE fits, which

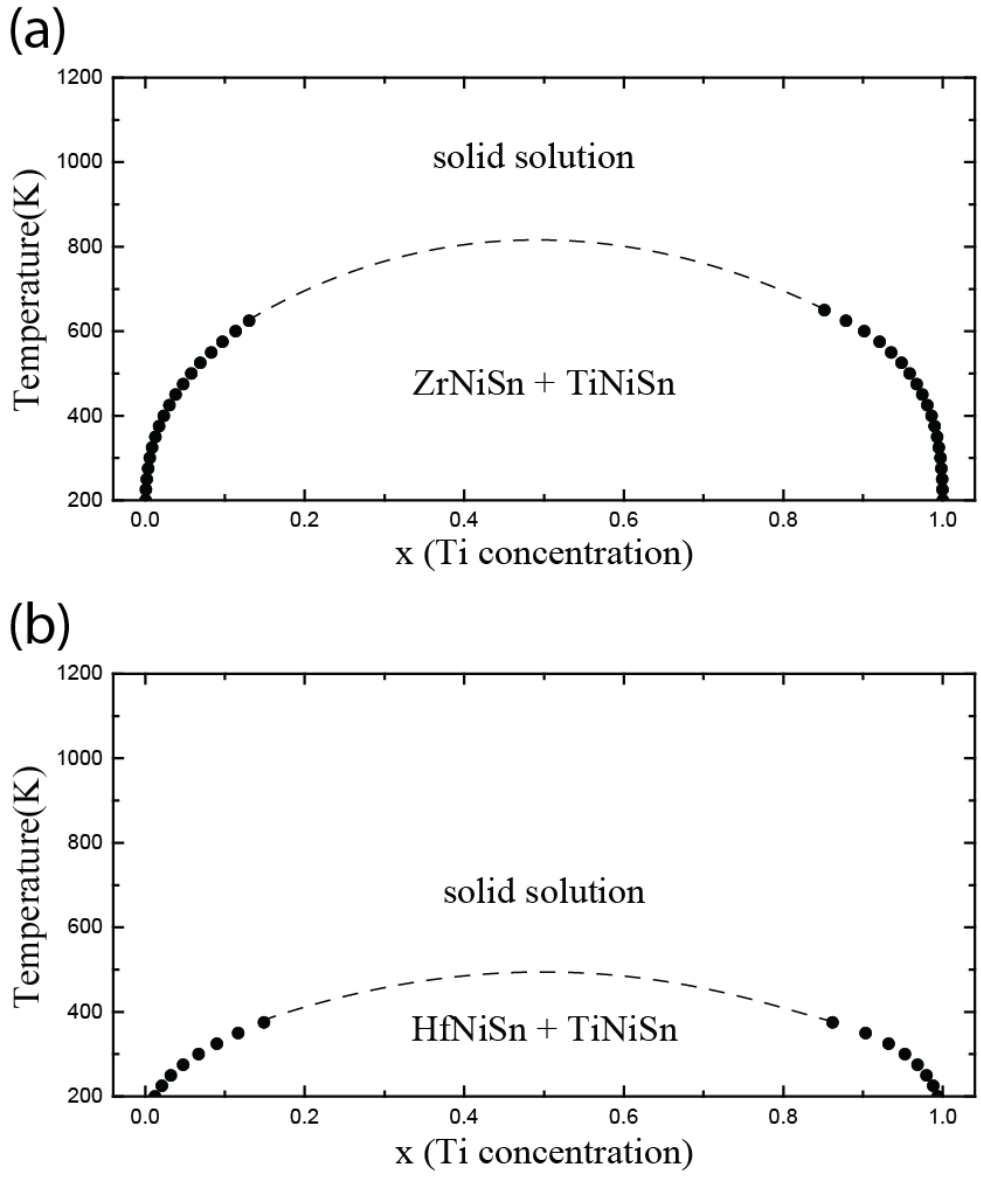

Figure 21. The temperature-composition phase diagrams for (a) $Zr_{1-x}Ti_xNiSn$ and (b) $Hf_{1-x}Ti_xNiSn$. Black dots represent calculated points along the phase boundary. Outside of the boundary, a solid solution minimizes the free energy. Inside the boundary, a two phase coexistence minimizes the free energy.

have an average error of less than 1 meV per configuration, are in good agreement with the DFT formation energies. The $Zr_{1-x}Ti_xNiSn$ was fit to the DFT formation energy of 55 configurations and had a CV score of 0.90 meV. The $Hf_{1-x}Ti_xNiSn$ was fit to 55 configurations and had a CV score of 0.87 meV. The cluster expansion fits were then used in Grand Canonical Monte Carlo simulations. The results of the phase diagram calculations are shown in Figure 21. Calculated points of the phase boundary are shown as black dots. Calculations are in close agreement with those of Mena *et. al.* [*123*], who used a cluster expansion method along with Canonical Monte Carlo simulations. The key difference between Grand Canonical and Canonical simulations is that particle exchange is allowed in Grand Canonical and the final composition is dependent on the chosen chemical potential. In Canonical Monte Carlo, the initial composition, *x*, is an independent variable. Despite this difference, the critical temperatures of the miscibility gap calculated in the two distinct studies agree within 50 ˚C of each other.

6.4 Pseudo-ternary $Hf_{1-x-y}Zr_xTi_yNiSn$ system

6.4.1 Pseudo-ternary formation energies

Figure 22 shows the DFT calculated formation energies for 277 distinct configurations of the pseudo-ternary $(Hf_{1-x-y}Zr_xTi_y)NiSn$ system ($0 \leq (x, y) \leq 1$). The pseudo-ternary energies follow similar trends as those of the binary compounds. The formation energies increase with Ti content, for all Zr/Hf ratios, with a maximum at $y = 0.5$. The formation energies are fairly symmetric about the $y = 0.5$ point. Only compositions along the $y = 0$ line (which corresponds to the binary $(Hf_{1-x}Zr_x)NiSn$ configurations) show negative formation energies relative to the pure compositions. All

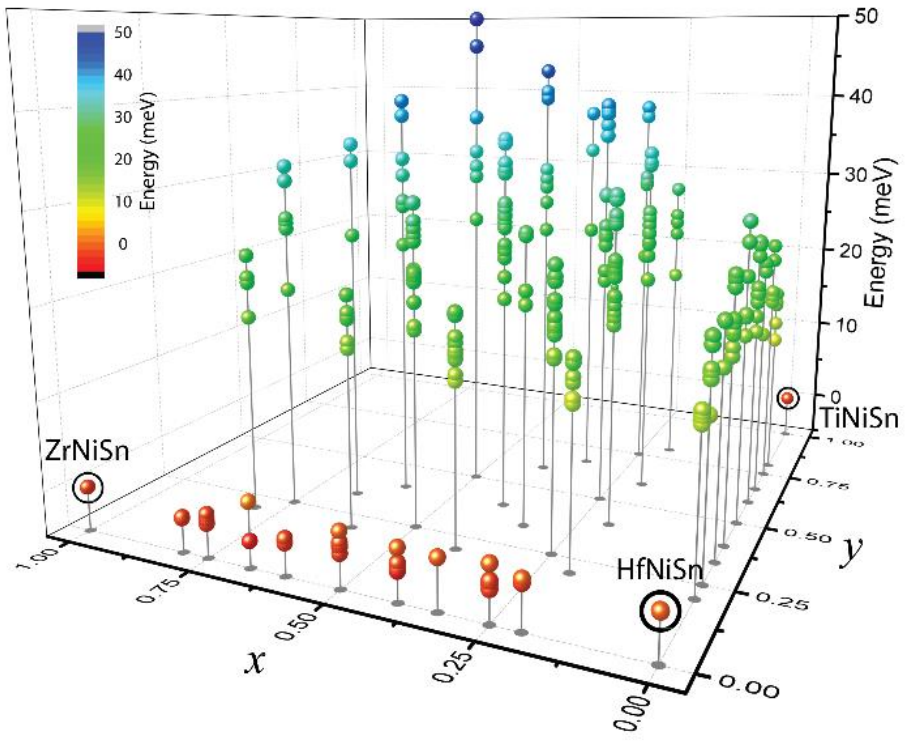

Figure 22. Pseudo-ternary DFT formation energies of the $Hf_{1-x-y}Zr_xTi_yNiSn$ system relative to the three pure states. 277 different configurations up to volumes five times the primitive cell were calculated in VASP. All configurations are found to have positive formation energy, confirming no local ordering is stable at zero temperature.

intermediate ordered configurations containing some Ti are predicted to have positive formation energies, suggesting that a miscibility gap should exist at finite temperature. The lattice parameters of the 277 configurations are plotted in Figure 23. The lattice parameters of the configurations follow Vegard's law closely and show that the lattice parameter of intermediate configurations can be predicted accurately.

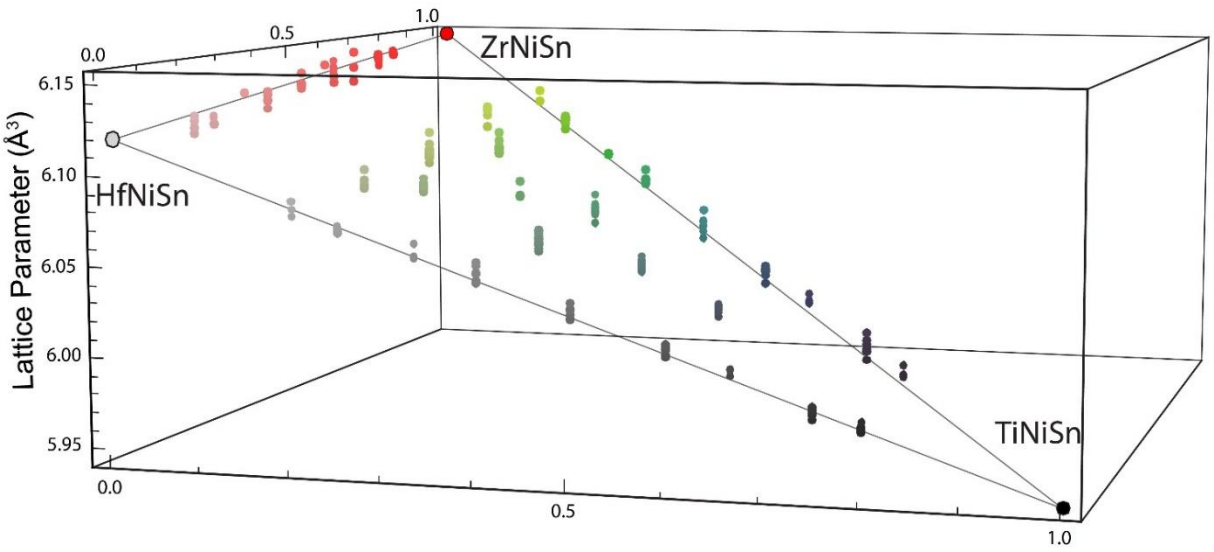

Figure 23. Pseudo-ternary DFT lattice parameters of configurations. The lattice parameters follow Vegard's law very closely.

6.4.2 Pseudo-ternary phase diagram

Figure 24 (a, b, and c) show the calculated pseudo-ternary phase diagram of the $(Hf_{1-x-y}Zr_xTi_y)NiSn$ system at temperatures of 300, 500, and 700 K, respectively. A solid black line denotes the calculated phase boundary between a single phase solid solution region (shown in color) and a two phase miscibility gap region (shown in white). For all temperatures, Hf and Zr are fully miscible in the half-Heusler structure and form a $(Hf_{1-x}Zr_x)NiSn$ solid solution. The solubility of Ti within the $(Hf_{1-x}Zr_x)NiSn$ solid solution depends on the Zr to Hf ratio and the

temperature. The higher energy of mixing between TiNiSn and ZrNiSn causes the solubility of Ti to decrease as the Zr content increases relative to the Hf content. At 300 K (Figure 24(a)), there is a large miscibility gap, where less than 1 % of Ti is soluble in $Hf_{1-x}Zr_xNiSn$ for the majority of the composition range, and the Ti solubility limit slightly increases to ~ 3 % for Hf-rich compositions ($x \leq 0.1$). As the temperature increases to 500 K (Figure 24(b)), the Ti solubility limit increases to around 9 % for Zr-rich compounds and up to 42 % for Hf-rich compounds. At 700 K (Figure

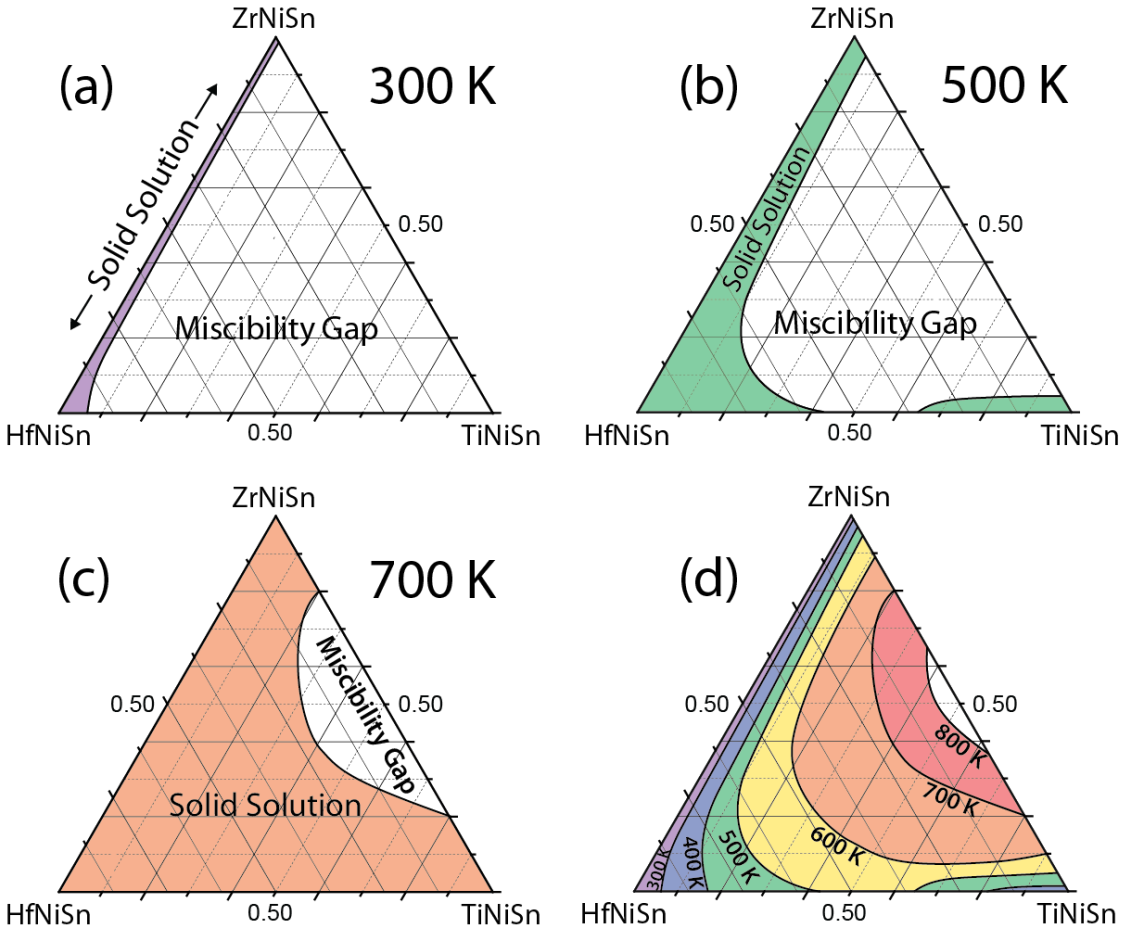

Figure 24. Pseudo-ternary $(Hf_{1-x-y}Zr_xTi_y)NiSn$ phase diagrams were calculated at 300 K (a), 500 K (b), 700 K (c). The solid solution region is shown in color, and the miscibility gap region is shown in white. As the temperature increases, the miscibility gap shrinks, and completely disappears above 900 K. Part (d) shows a summary of phase boundaries calculated from 300 to 800 K.

24(c)), Ti becomes fully soluble along the Hf-rich side, and a small miscibility gap remains near the Zr-rich ($x = 1$) line.

A summary of the calculated phase boundaries is shown in Figure 24(d). There is a critical temperature, T_c, above which the miscibility gap no longer exists, and a solid solution is favorable for all concentrations. For the $(Hf_{1-x-y}Zr_xTi_y)NiSn$ system, $T_c \approx 850$ K along the Zr-rich ($x = 1$) line. The critical temperature drops to $T_c \approx 500$ K, along the Hf-rich ($x = 0$) line, in agreement with the pseudo-binary calculations. This implies that any composition ($0 \leq (x, y) \leq 1$) will form a solid solution when held at temperatures above 850 K for a sufficiently long time in order to reach equilibrium. Similarly, for temperatures below 850 K, a thermodynamic driving force for spontaneous decomposition emerges and Ti-rich and Ti-poor phases should form if sufficient atomic diffusion is allowed to occur. The critical temperatures reported in this work have close agreement with the predictions of Mena *et. al.* [*123*], who used first-principles methods to model the pseudo-binary $Zr_{1-x}Ti_xNiSn$ and $Hf_{1-x}Ti_xNiSn$ systems. The calculated phase diagram in this work, however, disagrees with the high critical temperatures reported in the study by Gurth *et al.* [*124*], which created pseudo-binary phase diagrams based on experimentally measured solubility limits of arc melted samples reported in Kenjo *et al.* [*114*]. The phase diagram calculated via first-principles methods in this work suggests that the experimental solubility limits reported cannot be interpreted as the result of equilibrium processes, but rather as the result of kinetically trapped states. We therefore predict that spinodal decomposition does not occur at the annealing temperatures used in experiments (e.g. 1173 K). We examine this further in later sections.

In this work, $(Hf_{1-x-y}Zr_xTi_y)NiSn$ is treated as a pseudo-ternary system, where we assume that the Ni and Sn content remain stoichiometric. It has been observed in several experimental studies that other binary phases are present after arc melting [*28, 112, 113*]. These phases could be

related to the fact that TiNiSn does not directly melt but rather decomposes into several other phases such as $TiNi_2Sn$, Ni_3Sn_4, and Ti_2Sn [*28, 113*]. We note that such phases, which are not considered in this work, could modify the phase diagram.

6.5 Analysis and discussion

6.5.1 Comparison with experiment

Compositional heterogeneity in alloyed half-Heusler $(Hf_{1-x-y}Zr_xTi_y)NiSn$ compounds seems to be crucial to achieving a high thermoelectric figure of merit [*6, 92, 111, 116*]. Past experimental studies have shown that the degree of heterogeneity over the *M* sublattice of the *M*NiSn half-Heusler compound is very sensitive to the synthesis method [*112-114, 119, 120*]. The experimental literature, however, has not been able to clarify whether the microscale Ti-rich and Ti-poor $(Hf_{1-x-y}Zr_xTi_y)NiSn$ phases correspond to the thermodynamic equilibrium state or whether these microstructures have been trapped kinetically during synthesis. To help resolve this question, a first-principles statistical mechanics study of phase stability in the pseudo-ternary $(Hf_{1-x-y}Zr_xTi_y)NiSn$ composition space was performed. While the calculations predict a miscibility gap at low temperature between a Ti-rich and a Ti-poor half-Heusler phase, this miscibility gap disappears at temperatures above 850 K. Therefore, at the high annealing temperatures used in experiments (e.g., 1175 K), the equilibrium phase is predicted to be a solid solution characterized by disorder of Hf, Zr and Ti over the *M* sublattice.

The first-principles predictions of this study therefore suggest that the multiphase microstructures observed in arc melted and induction melted samples are generated during solidification and are subsequently trapped at lower temperatures due to sluggish kinetics of *M*

atoms in solid *M*NiSn. Experimental studies have found evidence in support of Ti-poor and Ti-rich regions that are created during the solidification step in synthesis. The phase diagram of the Hf-Zr-Ti-Ni-Sn composition space has not been fully characterized near the solid-liquid coexistence region, however, there is a large difference in the melting temperatures of HfNiSn or ZrNiSn (1760 K and 1708 K, respectively [*28*]) and the decomposition temperature of TiNiSn (1453 K) [*28*]. In the study of Gałązka *et al.* [*113*], the authors suggest that Zr and Hf rich half-Heusler phases may solidify first by forming around pure Hf nucleation seeds, followed by the solidification of a Ti enriched liquid as the temperature is further reduced. Using EDX, they observed Zr and Hf rich half-Heusler dendrites and an enrichment of Ti in the interdendritic areas. Hence, the phase separation observed in arc melted samples is likely created during the solidification process rather than the two week annealing step at 1173 K. Indeed, in the work of Kenjo et al. [*114*], the Ti-poor grains are well formed after the initial arc melting step. The annealing step had little effect on the grains and mainly served to remove the impurities from the Ti-rich half-Heusler phase in the intergranular regions.

6.5.2 Atomic diffusion in half-Heuslers

In order for the microstructures created during solidification to remain intact after annealing, the mobilities of Hf, Zr, and Ti must be sufficiently low, such that solidified microstructures are not able to reach the predicted equilibrium solid solution through interdiffusion. Solid-state diffusion of Hf, Zr and Ti over the *M* sublattice of the *M*NiSn half-Heusler compound is likely substitutional and mediated by a vacancy mechanism [*62-64, 67, 125-127*]. Atomic mobilities and their derived interdiffusion coefficients then not only depend on the migration barriers for individual hops, but also on the availability of diffusion mediating vacancies [*75, 125*].

While the calculation of equilibrium vacancy concentrations in compounds and alloys [*61-67*], especially those that are semiconductors [*65*], is quite involved, past first-principles studies by Colinet *et al.* [*81*] and Hazama *et al.* [*128*] predicted a charge-neutral Ti vacancy formation energy in TiNiSn of 3.2 and 3.9 eV respectively. These values are very large, especially when compared to typical alloys [*62-64*], and indicate that the equilibrium vacancy concentration over the *M* sublattice of *M*NiSn half-Heusler compounds will be exceedingly low, even at elevated temperature. Furthermore, the migration barriers for atomic hops between a filled and a vacant *M* site of *M*NiSn half-Heusler compounds are also large. These barriers were estimated for a Ti, Zr and Hf hop into an adjacent vacant site of the *M* sublattice from first principles within a large supercell.

The migration barriers associated with the self-diffusion of *M* site atoms: Ti, Zr, and Hf were calculated. The diffusion of *M* atoms within the stoichiometric HH matrix is likely to occur via a vacancy mechanism, where a vacancy located on the *M* site, Va_M, swaps with an M atom. The mechanism can be thought of as two separate processes: the formation of vacancies in the matrix and vacancy-atom exchange. As discussed in section 3.2.4, the diffusion coefficient in solids can be expressed as [*57*],

$$D = D_0 \exp\left[\frac{-E_a}{k_B T}\right]$$

where E_a is an activation energy, k_B is the Boltzmann constant, *T* is the absolute temperature, and D_0 is the diffusion prefactor, which depends on the jump distance, an effective jump frequency, and the vibrational entropy of vacancy formation [*58*]. The prefector, D_0, in this form has a weak temperature dependence arising from anharmonic vibrational excitations. The prefactor is commonly calculated from first principles within the harmonic approximation [*59, 60*]. The

activation energy of vacancy-mediated diffusion is made up of two contributions, $E_a = \Delta E_V + \Delta E_m$, where ΔE_V is the formation energy of a single vacancy in the matrix, and ΔE_m is the migration energy. The migration energy was calculated using the VASP software in this work, and values of vacancy formation were taken from literature [*81, 128*].

The energy of migration, ΔE_m, is defined as the difference in energy between the initial state and the energy of the transition state. The Nudged Elastic Band (NEB) calculations were performed in VASP to find the location and energy of the saddle point. Initial NEB calculations showed that the saddle point is located half way along the reaction path and the barrier energy is symmetric about the saddle point, thus subsequent NEB calculations were carried out with a single image at the saddle point. Geometrically, the saddle point was found to be shifted off of the direct line connecting nearest neighboring *M* sites (shown as a dashed line in Figure 25(a)) towards the vacant (¾, ¾, ¾) site (shown as an empty black circle in Figure 25(a)).

The predicted migration barriers for hops between neighboring *M* sites are 1.9, 3.0 and 2.7 eV for Ti, Zr and Hf, respectively, as shown in Figure 26. These values are very large compared to other substitutional alloys and compounds [*60, 63, 129*]. Since the overall activation barrier for substitutional diffusion is equal to the sum of the vacancy formation energy and elementary migration barriers [*57, 58*], the above estimates suggest activation barriers for intermixing that range between 5 and 7 eV. With activation barriers this large, interdiffusion among Ti, Zr and Hf will be negligible even at annealing temperatures of 1175 K.

The migration energy of Ni atoms diffusing to vacant sites on the ¾, ¾, ¾ sublattice was also calculated. Of the many pathways calculated, the lowest energy hops in the ZrNiSn matrix

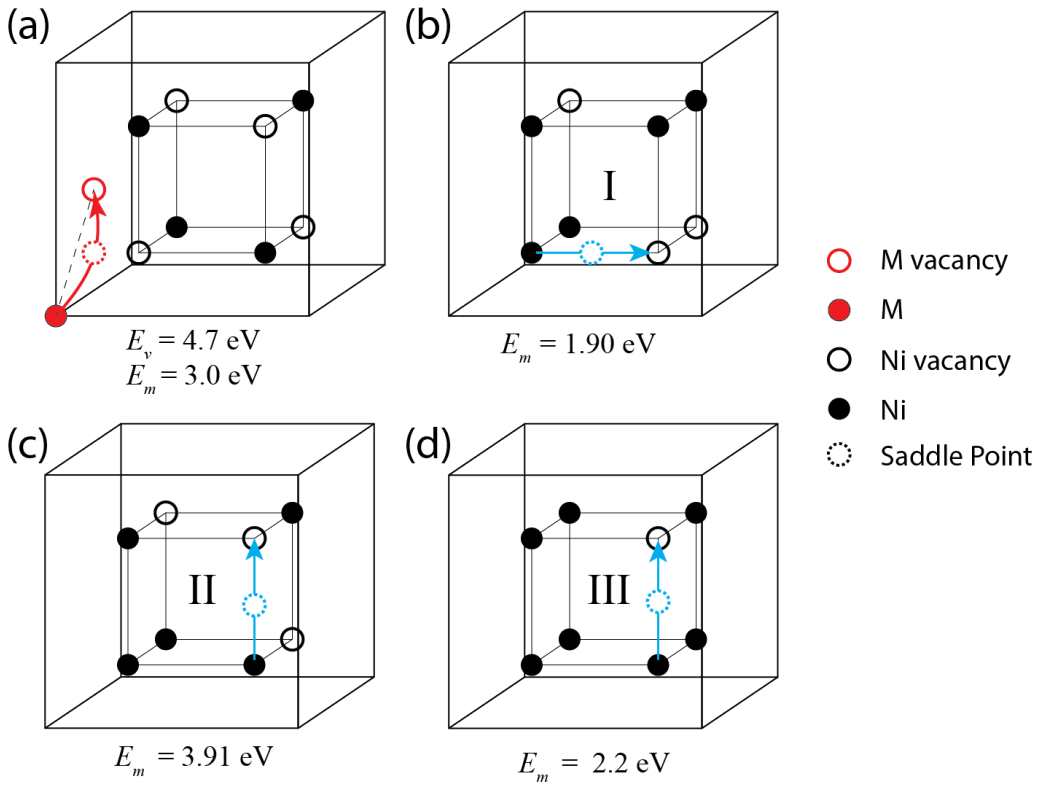

Figure 25. (a) Schematic of the migration path in the MNiSn (M = Ti, Zr, Hf) matrix of M-vacancy diffusion. (b), (c), and (d) show possible paths for Ni diffusion in variable Ni rich environments.

are shown in Figure 25(b) and Figure 25(c). The lowest energy migration path for Ni atoms in $ZrNi_2Sn$ are shown in Figure 25(d). The migration barrier energy for these hops is 1.90, 3.91, and 2.2 eV, respectively. The activation energy of these Ni migrations is between 2-3 eV as the vacancies on already exist within the half-Heusler structure and thus have no vacancy formation energy. This shows that, even compared to Ni atoms within the same material, the activation energy of M-atoms is around twice as large as that of Ni atoms. This is qualitatively in agreement with experiment where Ni atoms consolidate into full-Heusler nanosturctures via solid state reaction [*33, 34, 75-79*], whereas Ti, Zr, and Hf remain well mixed after solid state reaction [*119, 120*].

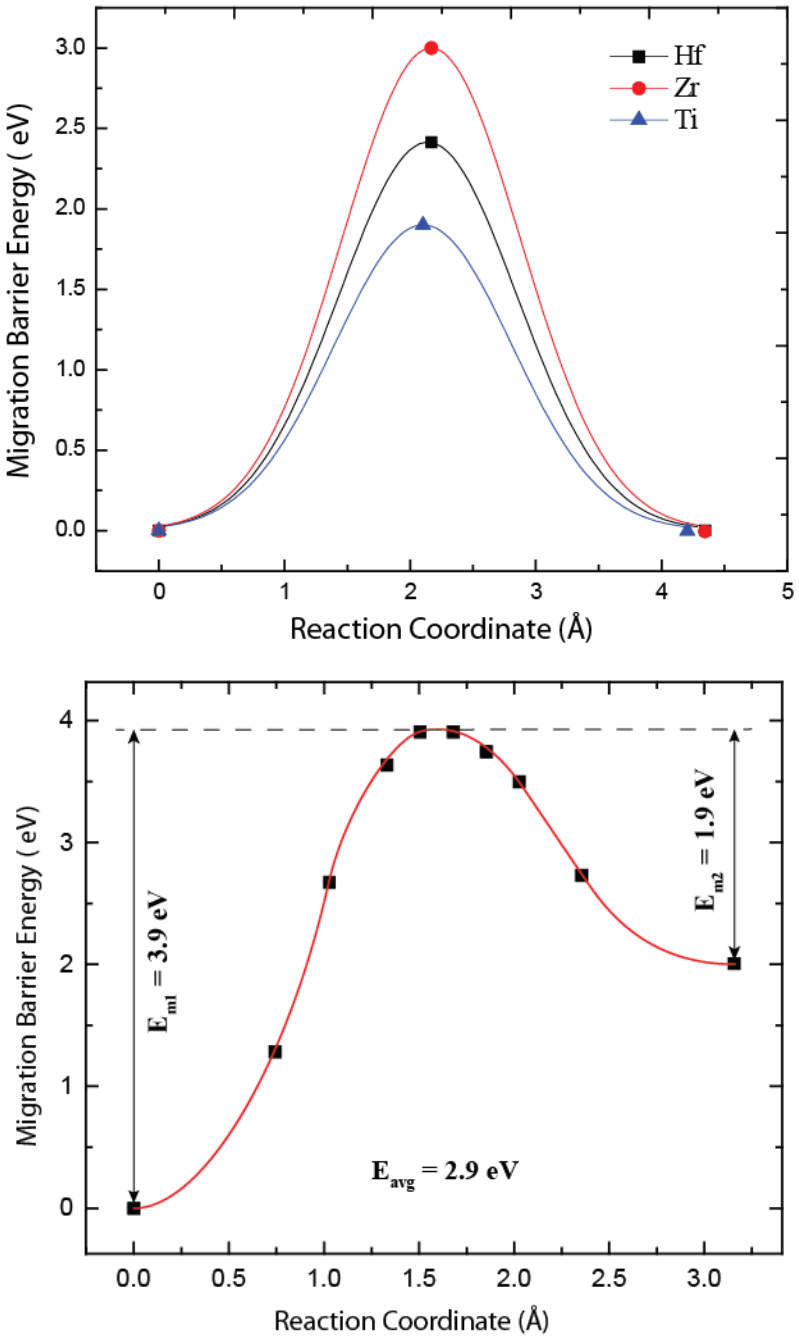

Figure 26. (top) plot of migration barrier energy along the reaction path for Ti, Zr and Hf atoms in TiNiSn, ZrNiSn, and HfNiSn respectively. Symbols represent calculated points along the reaction path and schematic lines are drawn to guide the eye. (bottom) Plot of the migration barrier energy along the lowest energy path for Ni atoms in stoichiometric ZrNiSn.

6.5.3 Experimental evidence of kinetically trapped states

The low critical temperature of the calculated phase diagram and the prediction of very low *M* site interdiffusion coefficients are consistent with the wide variety of microstructures that can be attained through different synthesis techniques. According to the calculated phase diagram, in equilibrium conditions, no two-phase decomposition would occur at a temperature of 1173 K. Thus, solid-state reaction synthesis can result in samples with relatively uniform microstructures, such as those observed in Downie *et al.* [*119*]. The slow diffusion of Ti, Zr, and Hf atoms within the half-Heusler phase make it possible that small inhomogeneities in the starting reaction mixture can form HH phases with slightly varying Ti, Zr, and Hf content, leading to the semi continuous distribution of lattice parameters observed in the XRD patterns [*119*].

In contrast, for synthesis techniques that cool samples from a melt, such as arc melting, induction melting, and melt spinning, the low diffusion rates of Ti, Zr, and Hf atoms would kinetically trap the preexisting microstructure. Therefore, the microscale dendrites that formed during solidification would remain intact after annealing at 1173 K, as was observed in Kenjo *et al.* [*114*] and Gałązaka *et al.* [*113*]. A schematic of a likely solidification path is shown in Figure 27. The lense type solid-liquid coexistence region is typical for materials systems with drastically different melting points. If the $Zr_{1-x}Ti_xNiSn$ system has such phase diagram, it is possible that the rapid cooling inherent to techniques such as arc melting, would create highly non-equilibrium conditions. Passing though the solid-liquid coexistence region quickly could then result in the two phase mixture of a Ti-poor solid and a Ti-rich liquid. After reaching lower temperatures, the Ti-rich liquid would solidify in the intergranular areas. The poor diffusion of M atoms would then freeze in the microstructure and prevent a solid solution to form even at medium to high temperatures.

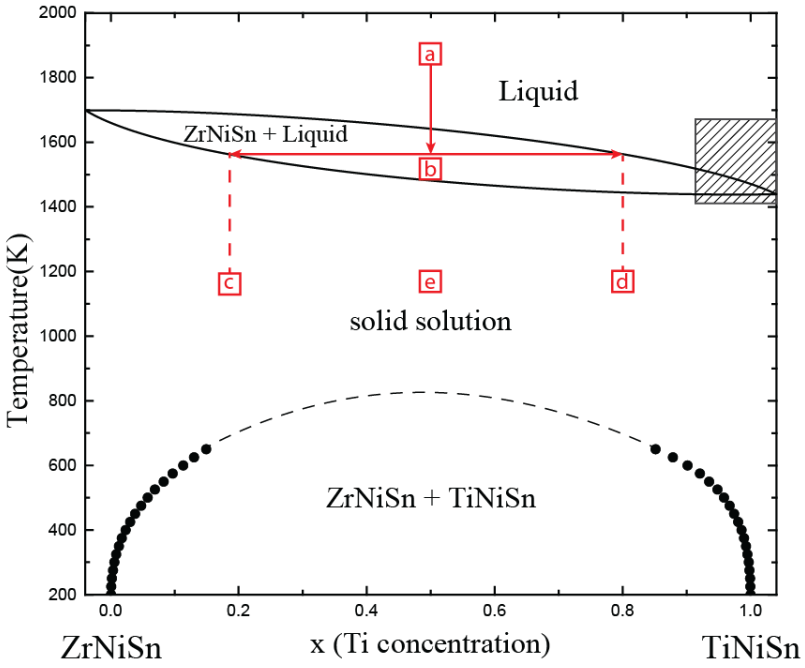

Figure 27. Schematic of the solidus and liquidus lines for the $Zr_{1-x}Ti_xNiSn$ system. The CE calculated phase boundaries for the solid-solid two phase mixture are shown as black dots. A possible route of solidification is shown in red and labeled (a-e).

The microscale phase separation is considered critical to lowering the lattice thermal conductivity of half-Heusler thermoelectrics. The calculated phase diagram presented in this work implies that such a microstructure is only meta-stable. Low diffusion coefficients benefit the material and make it possible to trap in heterogeneous microstructures during the solidification process. A recent study by Krez *et al.* [*130*] tested the stability of $Ti_{0.3}Zr_{0.35}Hf_{0.35}NiSn$ under thermal cycling. The sample was cycled from 373 K to 873 K at 10 K min^{-1} for up to 500 cycles and found that the dendritic microstructure remained intact, showing that the phase separated *M*NiSn materials are viable for power generation applications. The first-principles study presented in this work suggests that the solidification process is the critical step in creating the desired phase separated microstructures. Synthesis techniques, such as induction heating, which allow for better control of the cooling rate than arc melting, might provide control over the size and composition

of the resulting microstructure, leading to new methods for further enhancing the thermoelectric performance of half-Heusler alloys.

6.6 Conclusions

A first-principles statistical mechanics study using the cluster expansion method and Monte Carlo simulations was performed to predict phase stability of half-Heusler phases at finite temperature in the $(Hf_{1-x-y}Zr_xTi_y)NiSn$ pseudo-ternary composition space. A miscibility gap is predicted at low temperatures between TiNiSn and (Zr,Hf)NiSn compounds. The miscibility gap disappears above $T_c \approx 850$ K along the Zr-rich ($x = 1$) line. The critical temperature is lower along the Hf-rich ($x = 0$) line ($T_c \approx 500$ K). The asymmetry between the Zr-rich and Hf-rich critical temperatures is correlated with a larger lattice mismatch between ZrNiSn and TiNiSn, compared to that between HfNiSn and TiNiSn.

The low critical temperature predicted for the pseudo-ternary $(Hf_{1-x-y}Zr_xTi_y)NiSn$ phase diagram implies that the phase separation observed in experiments is not caused by an equilibrium thermodynamic process, such as spinodal decomposition, as suggested in [*124*]. Calculated migration barriers for Ti, Zr, and Hf diffusion indicate that the mobility of *M* atoms in *M*NiSn is very low. The calculated phase diagram combined with low diffusion coefficients suggest that Ti-rich and Ti-poor grains are created during solidification and are then kinetically trapped at lower temperatures. The low diffusion rates of *M* atoms represent new ways of controlling the phase separation via synthesis techniques and provides new routes to obtaining higher thermoelectric efficiency in HH alloys.

Chapter 7 Pb-based half-Heusler Alloys

7.1 *M*NiPb compounds

7.1.1 Introduction

In section 5.4.1, we discussed the vibrational properties of half-Heuslers. It was mentioned in section 5.4.3 that the eigenvectors of the acoustic phonon modes were dominated by the heaviest atom in the compound. For TiNiSn and ZrNiSn compounds, the heaviest element is Sn. This implies that there is an opportunity to further lower the thermal conductivity of HH alloys by disrupting the low frequency phonon transport carried by the Sn atoms [*102*, *104*]. This could be accomplished by either weakening the bonds between Sn and its neighboring atoms or by substituting other elements that occupy the Sn-site in the lattice. The bonding between Sn and Ni is particularly strong in *M*NiSn compounds as was noted in Chapter 5, so disrupting this covalent bonding might have adverse effects on the electronic transport properties. However, it is possible that by using isoelectronic substitution on the Sn-site the electrical properties will remain intact, and the mass defects on the Sn-site would heavily scatter acoustic phonons.

Isoelectronic alloying with Sn (atomic mass 118.71 g/mol) could be accomplished by using either Ge (atomic mass 72.64 g/mol) or Pb (atomic mass 207.2 g/mol). For either substitution to be effective, a large solubility limit is necessary. It is known that ZrNiGe does not form in the half-

Heusler structure, but instead the AlB_2 family (space group Pnma, #62) [*89*]. The difference in structure forces there to be a limited solubility of Ge within $ZrNiSn_{1-x}Ge_x$ in the half-Heusler phase. However, the crystal structure of *M*NiPb was recently determined to form as a half-Heusler, as discussed in the next section.

7.1.2 Stability of *M*NiPb

In a work by Gautier *et al.* [*131*], a large computational search for stable compounds of the ABX structure with a total of 18 valence electrons was performed. The ABX structure, where X is a group X element (i.e., Ni, Pb, Pt) or a group IX element (i.e., Co, Rh, Ir), and A and B are other elements selected, such that ABX has a total of 18 valence electrons, is found to form in many different crystal structures. However, a large fraction of known ABX compounds form in the half-Heusler structure. Of the 483 possible compounds in this family, only 83 had been synthesized so far. The study designed rigorous criteria for theoretically assessing the stability of a compound, and applied it to all 483 compounds. The stable phase of a given ABX compound is found through a three step process.

Step 1: the lowest energy crystal structure is determined by calculating the formation energy of 41 prototype structures that ABX structures are known to form in. The search is then expanded to combinations of the 41 structures calculated by use of a genetic algorithm, (see supplementary materials of [*131*]).

Step 2: The lowest energy structure is then tested for dynamic stability by calculating the phonon dispersion curves using density functional perturbation theory (DFPT) and identifying any imaginary phonon modes.

Step 3: The formation enthalpy, ΔH_f, of the lowest energy structure is then compared to that of competing binary and ternary phases. The competing phases considered are made up of an extensive list of known stable phases and unknown potential phases that would compete for existence with the structure in question. The list of unknown potential phases is created by making isovalent component swaps of known phases. The formation enthalpies of competing phases are used to construct a convex hull, $C(X_{ABX})$, where the thermodynamic stability of the ABX structure in question is assessed by its distance to the convex hull, $\Delta H_f - C(X_{ABX})$.

Using these criteria for thermodynamic stability, Gautier *et al.* correctly predicted all 84 previously reported compounds as stable, and identified 54 unreported compounds as stable. Of the 54 predicted stable compounds, 30 compounds are predicted to form in the half-Heusler structure type.

In order to test the predictions, 15 compounds were chosen and synthesized. The synthesis was carried out by mixing stoichiometric amounts of elemental powder, arc melting, and annealing. The results are a testament to the accuracy of their predictions; all 15 compounds synthesized were observed to form in the predicted crystal structure and the lattice parameters typically only deviated from the calculated values by 1-2 %.

Concerning thermoelectric materials, the study showed that the compounds ZrNiPb, ZrPdPb, and HfNiPb, were all predicted to be stable, and TiNiPb was found to be just barely unstable. Furthermore, the study went on to calculate their electronic band structures. All three stable Pb-based half-Heuslers have bandgaps less than 0.5 eV, making them possible thermoelectric candidates.

ZrNiPb was actually synthesized by Gautier *et al.* and found to form in a single phase. Its electronic properties were measured at room temperature and a power factor of 5.2 $\mu W\ cm^{-1}\ K^{-2}$ was found, which is comparable to that of undoped ZrNiSn at room temperature.

	Lattice Parameter (Å)	
	DFT	Experiment
ZrNiSn	6.153[a]	6.11[b]
ZrNiPb	6.241[c], 6.267[d]	6.176[d]

Table 3. DFT calculated and experimental lattice constants for ZrNiSn and ZrNiPb. (a) DFT-GGA from Page *et al*. [*85*], (b) experiemental lattice parameter from [*89*] , (c) unpublished by Page *et al*., and (d) DFT-GGA and experimental values of solid state reacted ZrNiPb from Gautier *et al*. [*131*].

7.2 Solubility limits of Pb in $MNiSn_{1-x}Pb_x$

7.2.1 Computational results

With the knoweldge that ZrNiPb is a stable half-Heusler compound and potentially good TE material, we set out to computationaly predict the solubility limits of Pb in $ZrNiSn_{1-x}Pb_x$. Here we discuss the unpublished results of our DFT study of the $ZrNiSn_{1-x}Pb_x$ system. The calculated lattice parameter of ZrNiPb matches well with that of Gautier *et al.* [*131*], and both are a close match with the experiemental value, as shown in Table 3. The lattice mismatch between ZrNiSn and ZrNiPb is only ~1.5 %, showing that the two materials are well matched for forming a solid solution.

Figure 28 shows the calculated formation energy of 32 configurations within the pseudo-binary $ZrNiSn_{1-x}Pb_x$ system for $0 \leq x \leq 1$. The configurations have both positive and negative energy relative to the ZrNiSn and ZrNiPb compounds. The dispersal of many different

configurations with similar values of negative formation energy implies that a solid solution is favorable for all values of *x*. This data implies that there is no phase separation even at low temperatures and that a solid solution should be stable for TE power generation.

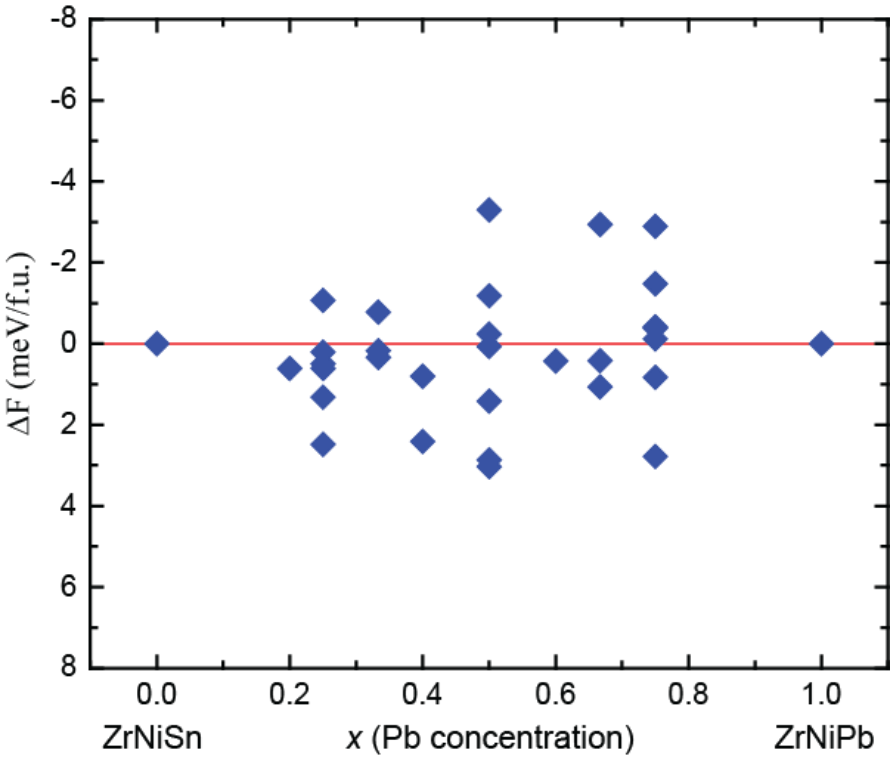

Figure 28. Configurational formation energies of the $ZrNiSn_{1-x}Pb_x$ system for $0 \leq x \leq 1$, plotted relative to ZrNiSn and ZrNiPb formation energy. Lower energy structures found along the composition space indicate the formation of a solid solution.

7.2.2 Experimental Results

Sample synthesis was attempted in order to confirm the ability of these materials to form a solid solution, however, even obtaining a single phase ZrNiPb material was extremely difficult. Both arc melting and solid-state reaction were attempted for ZrNiPb and HfNiPb compounds. The solid-state reacted samples were held at 950 ˚C for 2 weeks, and then allowed to cool naturally. Arc melted samples were flipped and remelted 3 times, and then powderized. During the arc

melting process, large amounts of vapor coated the inner wall of the chamber, and was thought to be unreacted Pb based on its appearance. Scanning electron microscope images were taken with a JEOL 7800FLV, as seen in Figure 29. In Figure 29(a), the solid state reacted ZrNiPb sample is observed to have multiple phases indicated by differing density indicated by contrast in the SEM image. Compositions of the phases were assessed by energy dispersive spectrometry (EDS) and the major phases are labeled directly on the image. The majority phase was found to be half-Heusler ZrNiPb, in agreement with X-ray diffraction data. The most prominent secondary phases are pure Pb and $ZrNi_2$. The Pb phase is not granular and appears to have solidified much later in the synthesis. This is possible due to the low melting point of Pb, 327.5 ˚C. It appears that some Pb was left unreacted during the solid-state reaction and remained liquid until the sample cooled below the Pb melting point.

Figure 29(b) shows and SEM image of the HfNiPb sample. The HfNiPb sample was found to me multiphase as well, this time with no clear majority phase. Pure Pb and Hf_2Ni are clearly seen in large amounts in the SEM image, and HfNiPb compounds are only found in thin layers on the boundaries of Hf_2Ni grains. This study suggests that ZrNiPb compounds might be possible via some other synthetic route, however HfNiPb compounds seem to be barely stable and it may not be possible to achieve as single phase HH at all.

While we were unable to find a proper synthetic route to remove the Pb impurities and obtain a single phase *M*NiPb compound, a recent study by Mao *et al.* [*132*] was successful in making ZrNiPb. Mao *et al.* employed a complicated synthetic process inorder to remove the Pb impurities. The process is as follows: 1) combine stoichiometric elemental powders with an extra 2 at.% of Pb to compensate for loses during arc melting; 2) arc melt Zr and Ni together first, then add the Pb and remelt three times; 3) pulverize the ingot with high energy ball milling for 20 hours;

4) spark plasma sinter the powders at 900 ˚C for only 2 minutes; and 5) anneal the resulting pellet at 800 ˚C for one week.

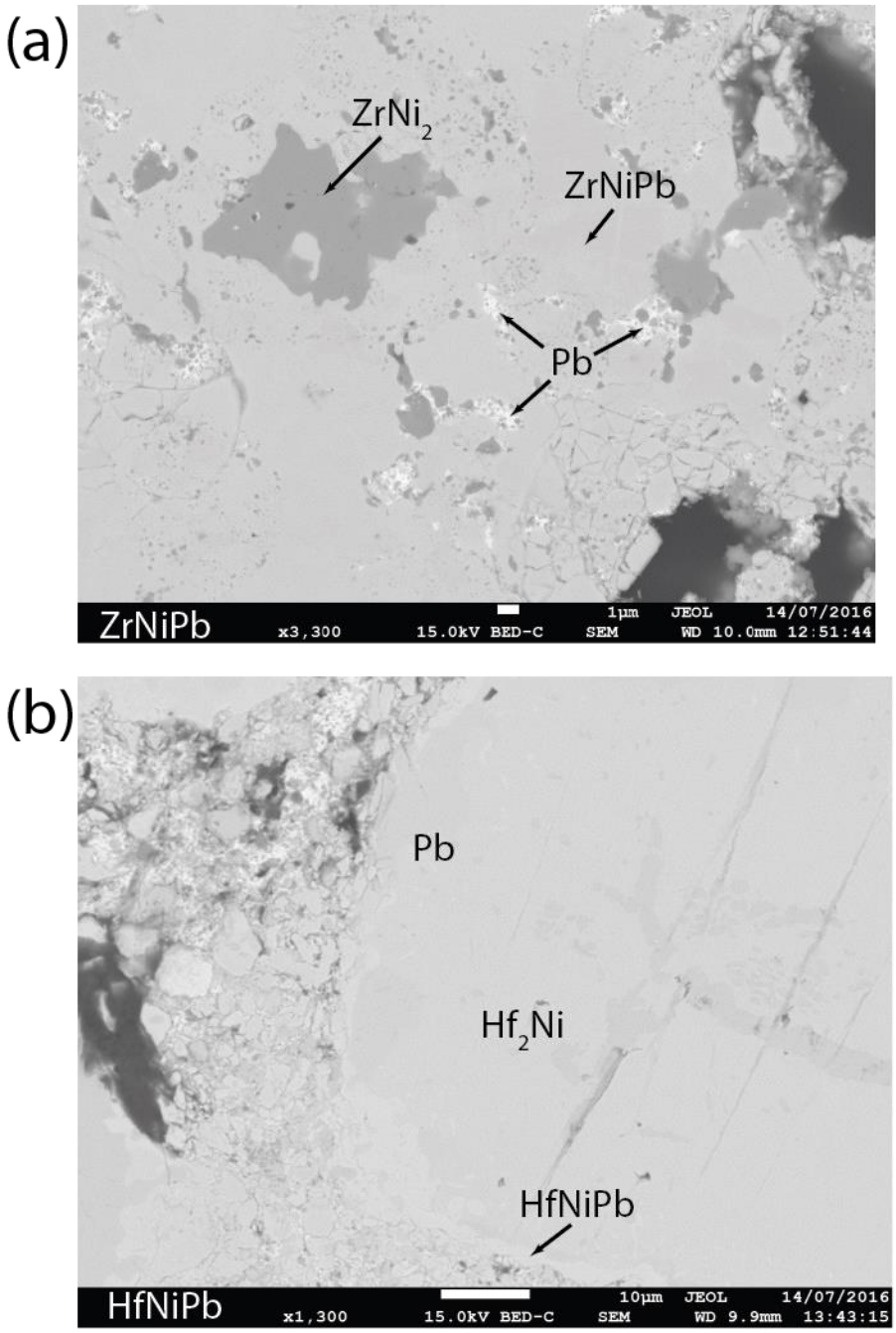

Figure 29. SEM images of (a) ZrNiPb and (b)HfNiPb samples prepared by solid-state reaction. Labeled compositions were measured using EDS.

Mao *et al.* observed that most of the Pb impurity phase was elminated during the final annealing stage. It is interesting to note that they have reversed the usual order of the last two synthesis stepes. Samples are usually annealed before densification. The extremly short SPS time of 2 minutes followed by annealing indicates that Pb may separate out of the matrix during the high temperature and pressure of SPS. This is in agreement with our study where we observed that pure Pb was expelled by the sample in liquid form during SPS. Annealing serves to bring the Pb back into the HH matrix and drastically improves the electrical properties of the material.

Mao *et al.* went on to show Bi to be an effective dopant, with optimal electrial properties obtained for $ZrNiPb_{0.98}Bi_{0.02}$. More critically, the study reports a series of $ZrNiPb_{0.98-x}Sn_xBi_{0.02}$ compounds for x = 0, 0.2, 0.4, 0.6, 0.8, and 0.98. The XRD results show without a doubt that the resultant materials form in a single phase half-Heusler structure for the whole compositions range, verifying our DFT predictions of a stable solid solution. The thermal conductivity of the x = 0.6 sample was found to be reduced by ~46% compared to that of the x = 0 sample. The power factors were found to be as good as in *M*NiSn compounds, with PF ≈ 50 $\mu Wcm^{-1}K^{-1}$, and *ZT* as high as 0.75 was found for the x = 0.6 sample. This study serves as a great proof of concept that ZrNiPb is a promising TE material that requires further study.

Chapter 8 Concluding Remarks

Half-Heusler alloys with general composition *M*NiSn are a promising class of thermoelectric materials. I used density functional theory calculations combined with a cluster expansion method and Monte Carlo simulations to predict phase equilibria as a function of temperature and composition of several exciting half-Heusler systems. By examining the $MNi_{1+x}Sn$ system, it was found that phase separation is highly favored even at high temperatures, suggesting that full-Heusler nano-structures are stable in operating conditions. The vibrational properties of *M*NiSn and MNi_2Sn compounds were predicted and it was found that $TiNi_2Sn$ has unstable phonon modes at the X-point. The instability arises from an atomic rearrangement, where the formation energy can be lowered by distorting the cell in such a way that keeps the bonding distances the same between Ni and Sn atoms, and shortens 4 of the 8 bonds between Ti and Ni atoms.

In the $Hf_{1-x-y}Zr_xTi_yNiSn$ system, a pseudo-ternary phase diagram was created from first principles. The results revealed that separation of Ti-rich and Ti-poor phases is only thermodynamically stable below the critical temperature of 850 K. I propose that the observed Ti-rich and Ti-poor microscale grains are a result of the kinetic process of cooling from melt, and are only meta-stable phases. However, atomic diffusion calculations show that diffusion rates are very slow, and these meta-stable states may be kinetically locked, such that even after annealing at high temperatures, the microscale grains remain unchanged.

Finally, the $ZrNiSn_{1-x}Pb_x$ system was examined. The work was inspired by the recent discovery that ZrNiPb has a stable half-Heusler crystal structure. My calculations show that a randomly ordered solid solution of Sn and Pb atoms is energetically favorable in the half-Heusler structure, and thus $ZrNiSn_{1-x}Pb_x$ compounds with any desired $0 \leq x \leq 1$ are possible. This prediction was experimentally confirmed in the study by Mao *et al*. [*132*]. $ZrNiSn_{1-x}Pb_x$ compounds provide an exciting new route to lowering the thermal conductivity of half-Heusler thermoelectrics.

References

1. L. D. Hicks, M. S. Dresselhaus, Thermoelectric Figure of Merit of a One-Dimensional Conductor. *Phys Rev B* **47**, 16631 (1993).
2. L. D. Hicks, M. S. Dresselhaus, Effect of Quantum-Well Structures on the Thermoelectric Figure of Merit. *Phys Rev B* **47**, 12727 (1993).
3. G. A. Slack, D. M. Rowe, Ed. (CRC Press LLC, Boca Raton, Florida 33431, 1995), chap. 34, pp. 407.
4. L. D. Zhao, S. H. Lo, Y. S. Zhang, H. Sun, G. J. Tan, C. Uher, C. Wolverton, V. P. Dravid, M. G. Kanatzidis, Ultralow thermal conductivity and high thermoelectric figure of merit in SnSe crystals. *Nature* **508**, 373 (2014).
5. C. Uher, J. Yang, S. Hu, D. T. Morelli, G. P. Meisner, Transport properties of pure and doped MNiSn (M=Zr, Hf). *Phys Rev B* **59**, 8615 (1999).
6. S. Sakurada, N. Shutoh, Effect of Ti substitution on the thermoelectric properties of (Zr,Hf)NiSn half-Heusler compounds. *Appl Phys Lett* **86**, 082105 (2005).
7. F. G. Aliev, V. V. Kozyrkov, V. V. Moshchalkov, R. V. Scolozdra, K. Durczewski, Narrow band in the intermetallic compounds MNiSn (M=Ti, Zr, Hf). *Z. Physik B - Condensed Matter* **80**, 353 (1990).
8. Q. Shen, L. Chen, T. Goto, T. Hirai, J. Yang, G. P. Meisner, C. Uher, Effects of partial substitution of Ni by Pd on the thermoelectric properties of ZrNiSn-based half-Heusler compounds. *Appl Phys Lett* **79**, 4165 (2001).
9. R. Farshchi, M. Ramsteiner, Spin injection from Heusler alloys into semiconductors: A materials perspective. *J Appl Phys* **113**, 191101 (2013).
10. H. C. Kandpal, C. Felser, R. Seshadri, Covalent bonding and the nature of band gaps in some half-Heusler compounds. *J Phys D Appl Phys* **39**, 776 (2006).
11. W. Jeitschko, Transition metal stannides with MgAgAs and MnCu2Al type structure. *Met. Trans.* **1**, 3159 (1970).
12. Y. Xia, S. Bhattacharya, V. Ponnambalam, A. L. Pope, S. J. Poon, T. M. Tritt, Thermoelectric properties of semimetallic (Zr, Hf)CoSb half-Heusler phases. *J Appl Phys* **88**, 1952 (2000).
13. S. R. Culp, J. W. Simonson, S. J. Poon, V. Ponnambalam, J. Edwards, T. M. Tritt, (Zr,Hf)Co(Sb,Sn) half-Heusler phases as high-temperature (> 700 degrees C) p-type thermoelectric materials. *Appl Phys Lett* **93**, 022105 (2008).
14. S. Öğüt, K. M. Rabe, Band gap and stability in the ternary intermetallic compounds NiSnM (M=Ti,Zr,Hf): A first-principles study. *Phys Rev B* **51**, 10443 (1995).
15. L. Offernes, P. Ravindran, C. W. Seim, A. Kjekshus, Prediction of composition for stable half-Heusler phases from electronic-band-structure analyses. *J Alloy Compd* **458**, 47 (2008).

16. J. Pierre, R. Skolozdra, J. Tobola, S. Kaprzyk, C. Hordequin, M. A. Kouacou, I. Karla, R. Currat, E. Lelievre-Berna, Properties on request in semi-Heusler phases. *J Alloy Compd* **262**, 101 (1997).
17. J. Tobola, J. Pierre, Electronic phase diagram of the XTZ (X=Fe, Co, Ni; T=Ti, V, Zr, Nb, Mn; Z=Sn, Sb) semi-Heusler compounds. *J Alloy Compd* **296**, 243 (2000).
18. Y. Stadnyk, A. Horyn, V. Sechovsky, L. Romaka, Y. Mudryk, J. Tobola, T. Stopa, S. Kaprzyk, A. Kolomiets, Crystal structure, electrical transport properties and electronic structure of the $VFe_{1-x}Cu_xSb$ solid solution. *J Alloy Compd* **402**, 30 (2005).
19. D. P. Young, P. Khalifah, R. J. Cava, A. P. Ramirez, Thermoelectric properties of pure and doped FeMSb (M=V,Nb). *J Appl Phys* **87**, 317 (2000).
20. L. Jodin, J. Tobola, P. Pecheur, H. Scherrer, S. Kaprzyk, Effect of substitutions and defects in half-Heusler FeVSb studied by electron transport measurements and KKR-CPA electronic structure calculations. *Phys Rev B* **70**, 184207 (2004).
21. C. G. Fu, T. J. Zhu, Y. T. Liu, H. H. Xie, X. B. Zhao, Band engineering of high performance p-type FeNbSb based half-Heusler thermoelectric materials for figure of merit zT > 1. *Energ Environ Sci* **8**, 216 (2015).
22. Y. Z. Pei, X. Y. Shi, A. LaLonde, H. Wang, L. D. Chen, G. J. Snyder, Convergence of electronic bands for high performance bulk thermoelectrics. *Nature* **473**, 66 (2011).
23. C. G. Fu, T. J. Zhu, Y. Z. Pei, H. H. Xie, H. Wang, G. J. Snyder, Y. Liu, Y. T. Liu, X. B. Zhao, High band degeneracy contributes to high thermoelectric performance in p-type half-Heusler compounds. *Adv Energy Mater* **4**, 1400600 (2014).
24. M. Mikami, A. Matsumoto, K. Kobayashi, Synthesis and thermoelectric properties of microstructural Heusler Fe_2VAl alloy. *J Alloy Compd* **461**, 423 (2008).
25. M. Mikami, Y. Kinemuchi, K. Ozaki, Y. Terazawa, T. Takeuchi, Thermoelectric properties of tungsten-substituted Heusler Fe_2VAl alloy. *J Appl Phys* **111**, 093710 (2012).
26. C. S. Lue, Y. K. Kuo, Thermoelectric properties of the semimetallic Heusler compounds $Fe_{2-x}V_{1+x}M$ (M=Al,Ga). *Phys Rev B* **66**, 085121 (2002).
27. C. G. Fu, S. Q. Bai, Y. T. Liu, Y. S. Tang, L. D. Chen, X. B. Zhao, T. J. Zhu, Realizing high figure of merit in heavy-band p-type half-Heusler thermoelectric materials. *Nat Commun* **6**, 216 (2015).
28. D. Jung, K. Kurosaki, C. Kim, H. Muta, S. Yamanaka, Thermal expansion and melting temperature of the half-Heusler compounds: MNiSn (M = Ti, Zr, Hf). *J Alloy Compd* **489**, 328 (2010).
29. H. Hohl, A. P. Ramirez, C. Goldmann, G. Ernst, B. Wölfing, E. Bucher, Efficient dopants for ZrNiSn-based thermoelectric materials. *Journal of Physics: Condensed Matter* **11**, 1697 (1999).
30. R. Asahi, T. Morikawa, H. Hazama, M. Matsubara, Materials design and development of functional materials for industry. *J Phys-Condens Mat* **20**, 064227 (2008).
31. J. E. Douglas, C. S. Birkel, M. S. Miao, C. J. Torbet, G. D. Stucky, T. M. Pollock, R. Seshadri, Enhanced thermoelectric properties of bulk TiNiSn via formation of a $TiNi_2Sn$ second phase. *Appl Phys Lett* **101**, 183902 (2012).
32. Y. Kimura, A. Zama, Thermoelectric properties of p-type half-Heusler compound HfPtSn and improvement for high-performance by Ir and Co additions. *Appl Phys Lett* **89**, 172110 (2006).

33. Y. F. Liu, P. Sahoo, J. P. A. Makongo, X. Y. Zhou, S. J. Kim, H. Chi, C. Uher, X. Q. Pan, P. F. P. Poudeu, Large Enhancements of Thermopower and Carrier Mobility in Quantum Dot Engineered Bulk Semiconductors. *J Am Chem Soc* **135**, 7486 (2013).
34. J. P. A. Makongo, D. K. Misra, X. Y. Zhou, A. Pant, M. R. Shabetai, X. L. Su, C. Uher, K. L. Stokes, P. F. P. Poudeu, Simultaneous Large Enhancements in Thermopower and Electrical Conductivity of Bulk Nanostructured Half-Heusler Alloys. *J Am Chem Soc* **133**, 18843 (2011).
35. X. A. Yan, G. Joshi, W. S. Liu, Y. C. Lan, H. Wang, S. Lee, J. W. Simonson, S. J. Poon, T. M. Tritt, G. Chen, Z. F. Ren, Enhanced Thermoelectric Figure of Merit of p-Type Half-Heuslers. *Nano Lett* **11**, 556 (2011).
36. X. L. Su, F. Fu, Y. G. Yan, G. Zheng, T. Liang, Q. Zhang, X. Cheng, D. W. Yang, H. Chi, X. F. Tang, Q. J. Zhang, C. Uher, Self-propagating high-temperature synthesis for compound thermoelectrics and new criterion for combustion processing. *Nat Commun* **5**, 4908 (2014).
37. W. J. Xie, A. Weidenkaff, X. F. Tang, Q. J. Zhang, J. Poon, T. M. Tritt, Recent Advances in Nanostructured Thermoelectric Half-Heusler Compounds. *Nanomaterials* **2**, 379 (2012).
38. J.-W. G. Bos, R. A. Downie, Half-Heusler thermoelectrics: a complex class of materials. *Journal of Physics: Condensed Matter* **26**, 433201 (2014).
39. T. J. Zhu, C. G. Fu, H. H. Xie, Y. T. Liu, X. B. Zhao, High Efficiency Half-Heusler Thermoelectric Materials for Energy Harvesting. *Adv Energy Mater* **5**, 1500588 (2015).
40. S. Chen, Z. F. Ren, Recent progress of half-Heusler for moderate temperature thermoelectric applications. *Mater Today* **16**, 387 (2013).
41. R. O. Jones, Density functional theory: Its origins, rise to prominence, and future. *Rev Mod Phys* **87**, 897 (2015).
42. K. Capelle, A bird's-eye view of density-functional theory. *Braz J Phys* **36**, 1318 (2006).
43. R. Car, M. Parrinello, Unified Approach for Molecular-Dynamics and Density-Functional Theory. *Phys Rev Lett* **55**, 2471 (1985).
44. K. Burke, Perspective on density functional theory. *J Chem Phys* **136**, 150901 (2012).
45. P. Hohenberg, W. Kohn, Inhomogeneous Electron Gas. *Phys Rev B* **136**, B864 (1964).
46. W. Kohn, L. J. Sham, Self-Consistent Equations Including Exchange and Correlation Effects. *Phys Rev* **140**, 1133 (1965).
47. M. Fuchs, M. Bockstedte, E. Pehlke, M. Scheffler, Pseudopotential study of binding properties of solids within generalized gradient approximations: The role of core-valence exchange correlation. *Phys Rev B* **57**, 2134 (1998).
48. J. P. Perdew, K. Burke, M. Ernzerhof, Generalized gradient approximation made simple. *Phys Rev Lett* **77**, 3865 (1996).
49. G. Kresse, J. Furthmuller, Efficient iterative schemes for ab initio total-energy calculations using a plane-wave basis set. *Phys Rev B* **54**, 11169 (1996).
50. P. E. Blochl, Projector Augmented-Wave Method. *Phys Rev B* **50**, 17953 (1994).
51. H. J. Monkhorst, J. D. Pack, Special Points for Brillouin-Zone Integrations. *Phys Rev B* **13**, 5188 (1976).
52. P. E. Blochl, O. Jepsen, O. K. Andersen, Improved Tetrahedron Method for Brillouin-Zone Integrations. *Phys Rev B* **49**, 16223 (1994).
53. W. Setyawan, S. Curtarolo, High-throughput electronic band structure calculations: Challenges and tools. *Comp Mater Sci* **49**, 299 (2010).

54. A. Togo, F. Oba, I. Tanaka, First-principles calculations of the ferroelastic transition between rutile-type and $CaCl_2$-type SiO_2 at high pressures. *Phys Rev B* **78**, 134106 (2008).
55. S. Baroni, S. de Gironcoli, A. Dal Corso, P. Giannozzi, Phonons and related crystal properties from density-functional perturbation theory. *Rev Mod Phys* **73**, 515 (2001).
56. X. Gonze, C. Lee, Dynamical matrices, born effective charges, dielectric permittivity tensors, and interatomic force constants from density-functional perturbation theory. *Phys Rev B* **55**, 10355 (1997).
57. R. W. Balluffi, S. M. Allen, W. C. Carter, *Kinetics of Materials*. Kinetics of Materials (Wiley, 2005), pp. 1.
58. P. Erhart, P. Jung, H. Schult, H. Ullmaier, *Atomic Defects in Metals*. H. Ullmaier, Ed., Atomic Defects in Metals (Springer-Verlag, Berlin Heidleberg, 1991), vol. 25.
59. G. Ho, M. T. Ong, K. J. Caspersen, E. A. Carter, Energetics and kinetics of vacancy diffusion and aggregation in shocked aluminium via orbital-free density functional theory. *Phys Chem Chem Phys* **9**, 4951 (2007).
60. M. Mantina, Y. Wang, R. Arroyave, L. Q. Chen, Z. K. Liu, C. Wolverton, First-principles calculation of self-diffusion coefficients. *Phys Rev Lett* **100**, 215901 (2008).
61. T. R. Mattsson, A. E. Mattsson, Calculating the vacancy formation energy in metals: Pt, Pd, and Mo. *Phys Rev B* **66**, 214110 (2002).
62. A. Van der Ven, G. Ceder, First principles calculation of the interdiffusion coefficient in binary alloys. *Phys Rev Lett* **94**, 045901 (2005).
63. A. Van der Ven, G. Ceder, Vacancies in ordered and disordered binary alloys treated with the cluster expansion. *Phys Rev B* **71**, 054102 (2005).
64. A. A. Belak, A. Van der Ven, Effect of disorder on the dilute equilibrium vacancy concentrations of multicomponent crystalline solids. *Phys Rev B* **91**, 224109 (2015).
65. S. B. Zhang, S. H. Wei, A. Zunger, H. Katayama-Yoshida, Defect physics of the $CuInSe_2$ chalcopyrite semiconductor. *Phys Rev B* **57**, 9642 (1998).
66. C. Wolverton, Solute-vacancy binding in aluminum. *Acta Mater* **55**, 5867 (2007).
67. C. Freysoldt, B. Grabowski, T. Hickel, J. Neugebauer, G. Kresse, A. Janotti, C. G. Van de Walle, First-principles calculations for point defects in solids. *Rev Mod Phys* **86**, 253 (2014).
68. J. M. Sanchez, F. Ducastelle, D. Gratias, Generalized cluster description of multicomponent systems. *Physica A* **128**, 334 (1984).
69. M. Asta, R. Mccormack, D. Defontaine, Theoretical-study of alloy phase-stability in the Cd-Mg system. *Phys Rev B* **48**, 748 (1993).
70. G. Inden, in *Phase Transformations in Materials*, G. Kostorz, Ed. (Wiley-VCH Verlag GmbH & Co. KGaA, Weinheim, FRG, 2001).
71. D. de Fontaine, Cluster approach to order-disorder transformations in alloys. *Solid State Physics (Academic, New York)* **47**, 33 (1994).
72. A. Van der Ven, M. K. Aydinol, G. Ceder, G. Kresse, J. Hafner, First-principles investigation of phase stability in LixCoO2. *Phys Rev B* **58**, 2975 (1998).
73. C. Kittel, H. Kroemer, *Thermal physics*. (W. H. Freeman, San Francisco, ed. 2d, 1980), pp. 473.
74. N. Metropolis, A. W. Rosenbluth, M. N. Rosenbluth, A. H. Teller, E. Teller, Equation of State Calculations by Fast Computing Machines. *J Chem Phys* **21**, 1087 (1953).
75. J. P. A. Makongo, D. K. Misra, J. R. Salvador, N. J. Takas, G. Y. Wang, M. R. Shabetai, A. Pant, P. Paudel, C. Uher, K. L. Stokes, P. F. P. Poudeu, Thermal and electronic charge

transport in bulk nanostructured Zr0.25Hf0.75NiSn composites with full-Heusler inclusions. *J Solid State Chem* **184**, 2948 (2011).
76. J. P. A. Makongo, D. Misra, N. J. Takas, K. L. Stokes, H. Gabrisch, P. F. P. Poudeu, Effect of partial filling of the structural vacant sites on the thermoelectric properties of $Zr_{0.25}Hf_{0.75}NiSn$ half-Heusler alloy. *MRS Online Proceedings Library* **1267**, DD05.12 (2010).
77. Y. Liu, A. Page, P. Sahoo, H. Chi, C. Uher, P. F. P. Poudeu, Electronic and phonon transport in Sb-doped $Ti_{0.1}Zr_{0.9}Ni_{1+x}Sn_{0.975}Sb_{0.025}$ nanocomposites. *Dalton Transactions* **43**, 8094 (2014).
78. Y. W. Chai, Y. Kimura, Nanosized precipitates in half-Heusler TiNiSn alloy. *Appl Phys Lett* **100**, 033114 (2012).
79. Y. W. Chai, Y. Kimura, Microstructure evolution of nanoprecipitates in half-Heusler TiNiSn alloys. *Acta Mater* **61**, 6684 (2013).
80. M. G. Kanatzidis, Nanostructured Thermoelectrics: The New Paradigm? *Chem Mater* **22**, 648 (2010).
81. C. Colinet, P. Jund, J. C. Tedenac, NiTiSn a material of technological interest: Ab initio calculations of phase stability and defects. *Intermetallics* **46**, 103 (2014).
82. K. Kirievsky, Y. Gelbstein, D. Fuks, Phase separation and antisite defects in the thermoelectric TiNiSn half-Heusler alloys. *J Solid State Chem* **203**, 247 (2013).
83. D. T. Do, S. D. Mahanti, J. J. Pulikkoti, Electronic structure of Zr-Ni-Sn systems: role of clustering and nanostructures in half-Heusler and Heusler limits. *J Phys-Condens Mat* **26**, 275501 (2014).
84. J. E. Douglas, C. S. Birkel, N. Verma, V. M. Miller, M. S. Miao, G. D. Stucky, T. M. Pollock, R. Seshadri, Phase stability and property evolution of biphasic Ti-Ni-Sn alloys for use in thermoelectric applications. *J Appl Phys* **115**, 043720 (2014).
85. A. Page, C. Uher, P. F. Poudeu, A. Van der Ven, Phase separation of full-Heusler nanostructures in half-Heusler thermoelectrics and vibrational properties from first-principles calculations. *Phys Rev B* **92**, 174102 (2015).
86. A. T. Zayak, P. Entel, K. M. Rabe, W. A. Adeagbo, M. Acet, Anomalous vibrational effects in nonmagnetic and magnetic Heusler alloys. *Phys Rev B* **72**, 054113 (2005).
87. P. J. Webster, K. R. A. Ziebeck, S. L. Town, M. S. Peak, Magnetic Order and Phase-Transformation in Ni_2MnGa. *Philos Mag B* **49**, 295 (1984).
88. C. Bungaro, K. M. Rabe, A. D. Corso, First-principles study of lattice instabilities in ferromagnetic Ni2MnGa. *Phys Rev B* **68**, 134104 (2003).
89. P. Villars, L. D. Calvert, W. B. Pearson, *Handbook of Crystallographic Data for Intermetallic Phases*. Acta Crystallographica Section A (American Society of Metals, Metals Park, OH, 1985), vol. 3.
90. A. Van der Ven, J. C. Thomas, Q. C. Xu, B. Swoboda, D. Morgan, Nondilute diffusion from first principles: Li diffusion in Li(x)TiS(2). *Phys Rev B* **78**, 104306 (2008).
91. B. Puchala, A. Van der Ven, Thermodynamics of the Zr-O system from first-principles calculations. *Phys Rev B* **88**, 094108 (2013).
92. M. Schwall, B. Balke, Phase separation as a key to a thermoelectric high efficiency. *Phys Chem Chem Phys* **15**, 1868 (2013).
93. J. W. Cahn, Spinodal Decomposition in Cubic Crystals. *Acta Metall Mater* **10**, 179 (1962).

94. A. Van der Ven, K. Garikipati, S. Kim, M. Wagemaker, The Role of Coherency Strains on Phase Stability in Li(x)FePO(4): Needle Crystallites Minimize Coherency Strain and Overpotential. *J Electrochem Soc* **156**, A949 (2009).
95. S. V. Barabash, V. Ozolins, C. Wolverton, First-principles theory of the coherency strain, defect energetics, and solvus boundaries in the PbTe-$AgSbTe_2$ system. *Phys Rev B* **78**, 214109 (2008).
96. H. Chi, H. Kim, J. C. Thomas, X. L. Su, S. Stackhouse, M. Kaviany, A. Van der Ven, X. F. Tang, C. Uher, Configuring pnicogen rings in skutterudites for low phonon conductivity. *Phys Rev B* **86**, 195209 (2012).
97. P. W. Voorhees, The Theory of Ostwald Ripening. *J Stat Phys* **38**, 231 (1985).
98. L. Lindsay, D. A. Broido, T. L. Reinecke, First-Principles Determination of Ultrahigh Thermal Conductivity of Boron Arsenide: A Competitor for Diamond? *Phys Rev Lett* **111**, 025901 (2013).
99. B. Zhong, Masters Thesis, Iowa State University, (1997).
100. R. Kuentzler, R. Clad, G. Schmerber, Y. Dossmann, Gap at the Fermi level and magnetism in RMSn ternary compounds (R = Ti, Zr, Hf and M = Fe, Co, Ni). *Journal of Magnetism and Magnetic Materials* **104–107**, 1976 (1992).
101. D. Wee, B. Kozinsky, B. Pavan, M. Fornari, Quasiharmonic Vibrational Properties of TiNiSn from Ab Initio Phonons. *J Electron Mater* **41**, 977 (2012).
102. P. Hermet, P. Jund, Lattice thermal conductivity of NiTiSn half-Heusler thermoelectric materials from first-principles calculations. *J Alloy Compd* **688**, 248 (2016).
103. P. Hermet, R. M. Ayral, E. Theron, P. G. Yot, F. Salles, M. Tillard, P. Jund, Thermal Expansion of Ni-Ti-Sn Heusler and Half-Heusler Materials from First-Principles Calculations and Experiments. *J Phys Chem C* **118**, 22405 (2014).
104. P. Hermet, K. Niedziolka, P. Jund, A first-principles investigation of the thermodynamic and mechanical properties of Ni-Ti-Sn Heusler and half-Heusler materials. *Rsc Adv* **3**, 22176 (2013).
105. W. Zhong, D. Vanderbilt, K. M. Rabe, First-Principles Theory of Ferroelectric Phase-Transitions for Perovskites - the Case of $BaTiO_3$. *Phys Rev B* **52**, 6301 (1995).
106. J. Bhattacharya, A. Van der Ven, Mechanical instabilities and structural phase transitions: The cubic to tetragonal transformation. *Acta Mater* **56**, 4226 (2008).
107. J. C. Thomas, A. Van der Ven, Finite-temperature properties of strongly anharmonic and mechanically unstable crystal phases from first principles. *Physical Review B* **88**, 214111 (2013).
108. G. Grimvall, B. Magyari-Kope, V. Ozolins, K. A. Persson, Lattice instabilities in metallic elements. *Rev Mod Phys* **84**, 945 (2012).
109. H. A. Jahn, E. Teller, Stability of polyatomic molecules in degenerate electronic states. I. Orbital degeneracy. *Proc R Soc Lon Ser-A* **161**, 220 (1937).
110. I. Galanakis, P. Mavropoulos, P. H. Dederichs, Electronic structure and Slater-Pauling behaviour in half-metallic Heusler alloys calculated from first principles. *J Phys D Appl Phys* **39**, 765 (2006).
111. E. Rausch, B. Balke, J. M. Stahlhofen, S. Ouardi, U. Burkhardt, C. Felser, Fine tuning of thermoelectric performance in phase-separated half-Heusler compounds. *J Mater Chem C* **3**, 10409 (2015).
112. S. Populoh, M. H. Aguirre, O. C. Brunko, K. Galazka, Y. Lu, A. Weidenkaff, High figure of merit in (Ti,Zr,Hf)NiSn half-Heusler alloys. *Scripta Mater* **66**, 1073 (2012).

113. K. Galazka, S. Populoh, L. Sagarna, L. Karvonen, W. J. Xie, A. Beni, P. Schmutz, J. Hulliger, A. Weidenkaff, Phase formation, stability, and oxidation in (Ti, Zr, Hf)NiSn half-Heusler compounds. *Phys Status Solidi A* **211**, 1259 (2014).
114. T. Kenjo, Y. Kimura, Y. Mishima, Phase Stability and Thermoelectric Properties of Half-Heusler Compounds (Ti,M)NiSn (M = Zr, Hf). *MRS Online Proceedings Library* **1218**, Z05.14 (2009).
115. K. Kurosaki, T. Maekawa, H. Muta, S. Yamanaka, Effect of spark plasma sintering temperature on thermoelectric properties of (Ti,Zr,Hf)NiSn half-Heusler compounds. *J Alloy Compd* **397**, 296 (2005).
116. E. Rausch, B. Balke, S. Ouardi, C. Felser, Enhanced thermoelectric performance in the p-type half-Heusler (Ti/Zr/Hf)$CoSb_{0.8}Sn_{0.2}$ system via phase separation. *Phys Chem Chem Phys* **16**, 25258 (2014).
117. T. Morimura, M. Hasaka, S. Yoshida, H. Nakashima, Microstructures and Thermoelectric Properties of an Annealed $Ti_{0.5}(Hf_{0.5}Zr_{0.5})_{0.5}NiSn_{0.998}Sb_{0.002}$ Ribbon. *J Electron Mater* **38**, 1154 (2009).
118. Y. F. Liu, P. F. P. Poudeu, Thermoelectric properties of Ge doped n-type $Ti_xZr_{1-x}NiSn_{0.975}Ge_{0.025}$ half-Heusler alloys. *J Mater Chem A* **3**, 12507 (2015).
119. R. A. Downie, D. A. MacLaren, J. W. G. Bos, Thermoelectric performance of multiphase XNiSn (X = Ti, Zr, Hf) half-Heusler alloys. *J Mater Chem A* **2**, 6107 (2014).
120. R. A. Downie, S. A. Barczak, R. I. Smith, J. W. G. Bos, Compositions and thermoelectric properties of XNiSn (X = Ti, Zr, Hf) half-Heusler alloys. *J Mater Chem C* **3**, 10534 (2015).
121. A. Page, A. Van der Ven, P. F. P. Poudeu, C. Uher, Origins of phase separation in thermoelectric (Ti, Zr, Hf) NiSn half-Heusler alloys from first principles. *J Mater Chem A* **4**, 13949 (2016).
122. D. F. Zou, S. H. Xie, Y. Y. Liu, J. G. Lin, J. Y. Li, Electronic structure and thermoelectric properties of half-Heusler $Zr_{0.5}Hf_{0.5}NiSn$ by first-principles calculations. *J Appl Phys* **113**, 193705 (2013).
123. J. M. Mena, H. G. Schoberth, T. Gruhn, H. Emmerich, Ab initio-based Monte Carlo and mean field studies of phase separated alpha NiSn (alpha =$Ti_{1-x}Hf_x$, $Ti_{1-x}Zr_x$, $Hf_{1-x}Zr_x$) compounds with C1(b) structure. *Acta Mater* **111**, 157 (2016).
124. M. Gurth, G. Rogl, V. V. Romaka, A. Grytsiv, E. Bauer, P. Rogl, Thermoelectric high ZT half-Heusler alloys $Ti_{1-x-y}Zr_xHf_yNiSn$ (0 <= x <= 1; 0 <= y <= 1). *Acta Mater* **104**, 210 (2016).
125. A. Van der Ven, H. C. Yu, G. Ceder, K. Thornton, Vacancy mediated substitutional diffusion in binary crystalline solids. *Prog Mater Sci* **55**, 61 (2010).
126. A. R. Allnatt, Theory of Phenomenological Coefficients in Solid-State Diffusion .1. General Expressions. *J Chem Phys* **43**, 1855 (1965).
127. A. R. Allnatt, Einstein and Linear Response Formulas for the Phenomenological Coefficients for Isothermal Matter Transport in Solids. *J Phys C Solid State* **15**, 5605 (1982).
128. H. Hazama, M. Matsubara, R. Asahi, T. Takeuchi, Improvement of thermoelectric properties for half-Heusler TiNiSn by interstitial Ni defects. *J Appl Phys* **110**, 063710 (2011).
129. Q. C. Xu, A. Van der Ven, First-principles investigation of migration barriers and point defect complexes in B2-NiAl. *Intermetallics* **17**, 319 (2009).

130. J. Krez, B. Balke, S. Ouardi, S. Selle, T. Hoche, C. Felser, W. Hermes, M. Schwind, Long-term stability of phase-separated half-Heusler compounds. *Phys Chem Chem Phys* **17**, 29854 (2015).
131. R. Gautier, X. W. Zhang, L. H. Hu, L. P. Yu, Y. Y. Lin, T. O. L. Sunde, D. Chon, K. R. Poeppelmeier, A. Zunger, Prediction and accelerated laboratory discovery of previously unknown 18-electron ABX compounds. *Nat Chem* **7**, 308 (2015).
132. J. Mao, J. W. Zhou, H. T. Zhu, Z. H. Liu, H. Zhang, R. He, G. Chen, Z. F. Ren, Thermoelectric Properties of n-type ZrNiPb-Based Half-Heuslers. *Chem Mater* **29**, 867 (2017).